

On the Flow of Highly Viscous Emulsions

A thesis written at
ETH Zurich

by
Marco Dressler

to attain the
Venia Legendi

on the recommendation of
Prof. Dr.-Ing. Erich J. Windhab
Professor of Food Process Engineering, ETH Zurich

2006

Copyright © 2006 Marco Dressler
Laboratory of Food Process Engineering (ETH Zurich)
All rights reserved.

On the Flow of Highly Viscous Emulsions

ISBN: 978-3-905609-35-5

Published and distributed by:

Laboratory of Food Process Engineering
Swiss Federal Institute of Technology (ETH) Zürich
ETH Zentrum, LFO
CH-8092 Zürich
Switzerland

<http://www.ilw.agrl.ethz.ch/vt/>

Printed in Switzerland by:

ETH Reprozentrale Höggerberg
HIL C45
CH-8093 Zürich
Switzerland

Preface

This volume collects research work on the rheology and fluid dynamics of highly viscous emulsions carried out at ETH Zurich between 2001 and 2005. A number of topics included in the book had earlier been published in the "Rheologica Acta" and in the "Journal of Non-Newtonian Fluid Mechanics" and have been covered in lectures held at ETH Zurich. Results in this volume are the headstone for two Ph. D. scholarships financed by the Swiss National Science Foundation (SNF).

The main focus of the volume is put for concreteness on highly viscous emulsions, with special regard to their rheology and fluid mechanics. Non-equilibrium Thermodynamics is adopted to construct flow models to describe their rheology and microstructure. Computer codes are developed to solve the models for flows encountered in rheometry and in flow geometries of processing relevance.

I hope that the volume will help the reader to get a feeling for the type of physical questions that one should ask in theory and experiment with regard to the rheology and fluid mechanics of highly viscous emulsions.

Prof. E. J. Windhab is acknowledged for giving me the possibility to carry out this research in an environment of pre-financed projects. The engineering approach to science was a good source of inspiration for this work. The fruitful discussions, the constructive criticisms, and the useful comments helped me to complete this work. I am indebted to Dr. P. Fischer, Dr. R. Gunde, Dr. J. Shaik, and the other present and past members of the Laboratory of Food Process Engineering at ETH Zurich for their help, support, discussions, and interest towards my work. I am grateful to Dipl. Phys. ETH A. Braun for the help in developing the codes of Chap. 5.2.3. Prof. K. Feigl (Michigan Technological University) and Dr. D. Megias-Alguacil (ETH Zurich) are acknowledged for fruitful collaboration and stimulating discussions.

In particular I want to express my gratitude to Prof. B. J. Edwards (University of Tennessee) for the hospitality at the Chemical Engineering Department, and his advice in carrying out this work. I further wish to thank Prof. A. N. Beris and Prof. N. J. Wagner (University of Delaware) for the invitation at the Chemical Engineering Department at University of Delaware and useful discussions concerning the comparison of my models with experimental data. Prof. H. H. Winter (University of Massachusetts) is acknowledged for the interest and enthusiasm towards my work

and for two stimulating discussions at ETH Zurich. I am grateful to Prof. A. Gadomski (University of Bydgoszcz) for inviting me to give a series of lectures as part of the official ceremonies for “The international Year of Physics 2005” in Bydgoszcz (Poland) and the possibility to discuss some topics of this thesis in the light of Statistical Physics.

The most important thank you goes to my parents, Jürgen and Lidia Dressler, to my brother Jürgen Dressler, to Bettina Jungen, and to my grandparents Franz and Marta Dressler for their support, help, and love.

Zurich, April 2006

Marco Dressler

Front cover: Microstructure-rheology relationships for a dilute emulsion. The figure shows model predictions for the steady shear viscosity, η , and the major droplet axis, L , as functions of shear rate, $\dot{\gamma}$. These qualitative predictions of emulsion behavior are obtained from the rheological model Eq. (3.18) (p. 48) with the following parameters: $\phi = 0.1$ (disperse phase volume fraction), $p^* = -0.25$ (viscosity ratio), $G/\Gamma = 4$ (ratio of matrix and interfacial elastic modulus), $\lambda_C \lambda_S / \lambda_n^2 = 1$ (ratio of relaxation times) $k = 0$ (EWM-power law index of matrix phase), $\theta = 0.001$ (phenomenological coupling of matrix and interfacial elasticity). Droplet deformation is shown schematically for various regimes of the major-droplet length curve. In Sec. 4.2 (Fig. 4.9) emulsion properties are discussed for the regime of low and intermediate shear rates.

Contents

List of Figures	vii
1. Introduction	1
1.1. Motivation and Literature Survey	1
1.2. A Simple Toy Model	6
2. Theory	13
2.1. Master Equation	13
2.2. Functional Calculus	14
2.3. Microstructural Constraints	15
2.4. Flow Equations	17
2.4.1. Unconstrained Microstructure	17
2.4.2. Volume Preserving Microstructure	25
3. Modeling	31
3.1. Matrix Viscoelasticity	31
3.1.1. System Variables	31
3.1.2. Poisson and Dissipation Bracket	32
3.1.3. General Flow Equations	33
3.1.4. System Hamiltonian	35
3.1.5. Phenomenological Matrices	35
3.1.6. Mechanical Energy Dissipation	38
3.1.7. Model Equations	40
3.2. Break-up and Coalescence	43
3.2.1. System Variables	43
3.2.2. Droplet Number Equation	44
3.2.3. System Hamiltonian	45
3.2.4. Phenomenological Matrices	46
3.2.5. Mechanical Energy Dissipation	46
3.2.6. Model Equations	48
3.3. Surfactants	49

3.4. Highly Concentrated Emulsions	50
3.5. Critical Comment on Emulsion Models	51
4. Rheology	53
4.1. Model with Matrix Viscoelasticity	53
4.1.1. Simple Shear Flow	54
4.1.2. Elongational Flow	63
4.1.3. Four-Roll Mill Flow	67
4.2. Model with Break-up and Coalescence	69
4.2.1. Simple Shear Flow	70
4.2.2. Elongational Flow	79
5. Simple Laminar Flows	85
5.1. Channel and Tube Flow	85
5.1.1. Model with Matrix Viscoelasticity	88
5.1.2. Model with Break-up and Coalescence	90
5.2. Annular Flow	94
5.2.1. Couette Flow	97
5.2.2. Poiseuille Flow	101
5.2.3. Helical Flow	105
6. Conclusions	111
Bibliography	113
A. Comparison with Experimental Trends	121
A.1. Single Droplet Deformation in Viscoelastic Matrix Fluid	121
A.2. PIB/PDMS blend with low viscoelastic contrast	123
A.3. HPC/PDMS600 blend with high viscoelastic contrast	128

List of Figures

1.1. Morphological and viscometric properties of a Toy Model	8
4.1. Rate of mechanical energy dissipation for a model emulsion	55
4.2. Semiaxes of ellipsoidal droplets for start-up of shear flow	56
4.3. Viscometric properties for start-up of shear flow	57
4.4. Viscometric and morphological properties for steady shear flow	59
4.5. Shear viscosity and first normal stress coefficient for various emulsions . .	62
4.6. Viscometric and morphological properties for uniaxial elongational flow .	64
4.7. Viscometric and morphological properties for planar elongational flow . .	66
4.8. Morphological emulsion properties for start-up of four-roll mill flow . . .	68
4.9. Steady shear flow properties of a model emulsion with break-up	71
4.10. Properties of the droplet distribution function for steady shear flow . . .	72
4.11. Droplet distribution functions for steady shear flow	74
4.12. Transient shear flow properties of an emulsion with break-up	76
4.13. Properties of the droplet distribution functions for transient shear flow .	77
4.14. Droplet distribution functions for transient shear flow	78
4.15. Uniaxial elongational flow properties of a model emulsion with break-up .	80
4.16. Properties of the droplet distribution function in steady elongational flow	81
4.17. Droplet distribution function for steady uniaxial elongational flow	82
5.1. Channel flow profiles for data of a PIB/PDMS emulsion	89
5.2. Channel flow for an emulsion with break-up	91
5.3. Stress and droplet shape profiles for channel flow	92
5.4. Droplet size and number density profiles for channel flow	93
5.5. Couette flow of an emulsion in an annular gap	98
5.6. Droplet size and number density profiles for Couette flow	99
5.7. Droplet semiaxes for Couette flow	100
5.8. Poiseuille flow of an emulsion in the annular gap	102
5.9. Droplet size and number density profiles for Poiseuille flow	103
5.10. Droplet semiaxes for Poiseuille flow	104
5.11. Helical flow of an emulsion in the annular gap	106
5.12. Stress profiles for helical flow	107

5.13. Droplet size and number density profiles for helical flow	108
5.14. Droplet semiaxes for helical flow	109
A.1. Semiaxis of a silicon droplet in viscoelastic corn syrup fluid	122
A.2. Shear flow properties of a PIB/PDMS emulsion	124
A.3. Properties of a PIB/PDMS emulsion for start-up of shear flow	126
A.4. Shear stress and first normal stress difference for a HPC/PDMS blend . .	129

1. Introduction

The main purpose of this initial chapter is to introduce into the field of emulsion rheology and to make a first acquaintance with the experimental characterization and the theoretical description of emulsions. It is useful to start with a summary of relevant work in the field and to motivate the need to develop continuum descriptions for highly viscous emulsions. Then, to present a simple Toy Model sharing some basic properties of all descriptions to be developed later.

1.1. Motivation and Literature Survey

In recent years efforts have been undertaken to describe the flow of highly viscous emulsions. Highly viscous emulsions are liquids consisting of a thick matrix fluid with homogeneously dispersed droplets of a second, thinner fluid referred to as the disperse phase. These materials play an important role in the manufacturing of foods, pharmaceuticals, and plastics so that an understanding of their flow behavior, microstructure characteristics, and material properties is of interest for the applied engineer. For the theoretician the modeling of highly viscous emulsions is a challenge since a set of generally accepted flow equations which are able to describe their rheology together with the dynamics of the disperse phase inclusions is not available. The issue seems even more challenging if one brings to mind that there is no consensus on the mathematical variables describing appropriately highly viscous emulsions. This lack of consensus and knowledge is a good starting point and bears the opportunity to achieve new insight and to gain alternative understanding.

It is clear that highly viscous emulsions, as introduced in the preceding paragraph, are complicated systems exhibiting complex flow behavior due to the highly viscous (*i. e.* thick) matrix, the characteristics of the matrix-disperse phase interface, and the large number of dispersed droplets. Due to these properties, they exhibit astonishing flow behavior, *e. g.* die swelling or rod climbing (Bird et al., 1987), which in turn influences the microstructural characteristics. Therefore, model systems are investigated both experimentally and theoretically to gain advanced knowledge on highly viscous

emulsions. The model systems mentioned in the preceding sentence consist, *e. g.*, of a Newtonian (*i. e.* thin) drop in another Newtonian liquid. For such a model emulsion, the complexity “thick matrix fluid” is eliminated and the complexity “large number of droplets” is reduced by investigating a thin matrix fluid and a single droplet, respectively. The advantage of such model systems are easier sample preparation and experimental characterization, *e. g.* droplet deformation and break-up measurements. The disadvantage is absence of important emulsion characteristics, *e. g.* matrix viscoelasticity and droplet coalescence. Therefore, data on model systems should be considered carefully when speaking about highly viscous emulsions. In the following paragraph we summarize research activities on model emulsions which have been and are currently undertaken at ETH Zurich.

The considerable amount of work dealing with processing, rheology, and Computational Fluid Dynamics (CFD) of highly viscous emulsions which has been carried out in ETH’s Laboratory of Food Process Engineering is summarized in (Windhab et al., 2005): Wolf (1995) studied the dynamics of a single emulsion droplet in shear flow, *i. e.* fluid motion due to relative motion of parallel walls confining it. Kaufmann (2002) extended this work studying deformation of single droplets in more general flows, *e. g.* stretching flows and in the gap between rotating concentric or eccentric cylinders. With these experiments, deformation characteristics and break-up criteria for single droplets have been determined. Megias-Alguacil et al. (2004) refined the measuring techniques to extract reliable surface tension data from deforming droplets and to study the role of surfactants. Droplet deformation experiments are time consuming and difficult due to the macroscopic length and time scales and the non-equilibrium nature of droplet deformation. Therefore, Computational Fluid Dynamics (CFD) of model emulsions is used to understand model emulsions. This allows also to look at flows which are difficult to realize experimentally. In Feigl et al. (2003) a CFD approach has been developed for studying single droplet deformation in mixed, dispersing-type, flow fields. This approach consists of a finite element method to solve the Navier-Stokes equations for Newtonian liquids, calculation of a particle path in the flow, and calculation of droplet deformation along the path using a boundary integral technique (Loewenberg and Hinch, 1996). In Kaufmann (2002) the hybrid scheme has been applied to stretching flows and concentric/eccentric cylinder geometries to simulate flow of model emulsions. The idea behind the choice of these flows and geometries is the desire to model extrusion processing of highly viscous emulsions. However, the numerical procedure is for Newtonian liquids and it does not account for the coupled effects of droplet deformation, breakup/coalescence, and thick matrix on the flow and processability of highly viscous emulsions. Furthermore, it is not possible to model the droplet size distribution function of polymer blends (*cf.* Caserta et al., 2005, 2004) within this simulation approach. In this volume we try to give an idea how these issues can be addressed using non-equilibrium Thermodynamics. We conclude this section giving an overview of the relevant research work carried out by other researchers.

In the 1930s, Taylor (1932, 1934) presented experimental and theoretical studies on deformation of a single Newtonian fluid droplet in a Newtonian matrix fluid. In the 1950s, Oldroyd (1953, 1955) developed a theory for the linear viscoelastic behavior of emulsions of Newtonian liquids with an ensemble of droplets. Using an effective medium approach and assuming that the interfacial tension between the emulsion phases does not change with deformation, he derived an expression for the complex modulus characterizing linear viscoelastic emulsion behavior. In the dilute disperse phase regime, *i. e.*, for small droplet concentration, Oldroyd's expression for the complex modulus is consistent with the results of Taylor (1932, 1934). The works of Oldroyd represent the first steps towards the development of a continuum description of highly viscous emulsions and have been the starting point for further research. In the 1970s, they have been picked up by Choi and Schowalter (1975) who adopted a cell model and a perturbation expansion of droplet concentration and droplet deformation to refine Oldroyd's expression for the complex modulus. This allowed for more reliable prediction of experimental data. Finally in the 1990s, Palierne (1990) generalized Oldroyd's expression for the elastic modulus to allow disperse and continuous phases to be viscoelastic. In the limit of constant interfacial tension, the predictions of Palierne's theory are identical with the predictions of Oldroyd (1953, 1955) and Choi and Schowalter (1975). Today, this model represents the state-of-the-art to describe and to fit experimental data for highly viscous emulsions taken in the regime of linear viscoelasticity. It is also adopted to obtain the droplet size in highly viscous emulsions. However, the Palierne Model for highly concentrated emulsions as well as the Taylor theory for dilute systems are for the small deformation regime; they cannot describe the non-linear viscoelastic emulsion behavior.

At the beginning of the 1990s, Doi and Ohta (1991) put forth a continuum theory for a mixture of two immiscible fluids, which still today is very popular to describe the flow of highly viscous emulsions. The Doi-Ohta theory was developed to describe the flow of Newtonian fluids of equal viscosity and roughly equal density. Furthermore, the theory assumes a 50:50 emulsion so that both phases maintain continuity (co-continuous systems). The rheology of the Doi-Ohta fluid differs from that of a single Newtonian fluid because of the presence of interface, which is accounted for by two variables: the interface orientation tensor and the amount of interfacial area. Over the past fifteen years, non-equilibrium Thermodynamics has become a well established theory to investigate fluids with internal microstructure (cf. e. g. Beris and Edwards, 1994). Recently, polymer blends and emulsions have become the subject of investigation in non-equilibrium thermodynamics, with the goal being to derive dynamical time evolution equations for these systems. The first attempts (cf. e. g. Wagner et al., 1999) in this direction focused on blends of Newtonian liquids with a co-continuous morphology and, in particular, on the improvement of the Doi-Ohta Model. These efforts tried to obtain more realistic relaxation expressions within the context of the Doi-Ohta theory without changing the microstructural variable of the Doi-Ohta Model.

Since 1998, research activities in theoretical polymer blend rheology shifted also towards blends with a droplet morphology, where a disperse phase is present as microscopically small droplets in a continuous matrix. Maffettone and Minale (1998) introduced the first constrained-volume model for the deformation, orientation, and advection of ellipsoidal droplets of a Newtonian fluid in a second Newtonian matrix fluid. In this model, the droplet is described in terms of a second-rank, contravariant microstructural tensor with constant determinant to account for volume preservation of the disperse phase. Note that the model, as developed by Maffettone and Minale (1998), is purely phenomenological and does not give an expression for the extra stress tensor. In the model it is assumed that the so-called "volume preservation constraint" is fulfilled for arbitrary homogeneous deformation and that the shape of the droplet can be represented by an ellipsoid even close to break up. This approximation is in good agreement with computer simulations of Loewenberg and Hinch (1996) and with experimental observations of Guido and Villone (1998). Aït-Kadi et al. (1999) undertook a thermodynamic study of general constrained-volume models which lead to a restricted set of time evolution equations for these systems. Later, this restricted set of time evolution equations was generalized by Edwards et al. (2003). Grmela et al. (2001) adopted a non-equilibrium Thermodynamics approach and introduced a phenomenological expression for the elastic free energy to obtain a thermodynamically consistent expression for the extra stress tensor for the Maffettone and Minale (MM) Model. This expression has been evaluated and compared with experimental data for emulsions by Yu et al. (2002). Efforts have been undertaken to generalize the MM Model to describe platelet like droplet configurations as found for thin droplet phase liquids (Maffettone and Greco, 2004), non-Newtonian fluid components (Minale, 2004), and to extract viscometric properties from single droplet deformation experiments (Minale and Maffettone, 2003).

An alternative constrained-volume model for blends of Newtonian liquids with a droplet morphology was presented in Almusallam et al. (2000), the ALS Model. The model is written in terms of a modified anisotropy tensor of the Doi-Ohta type to describe the disperse phase morphology. For this variable, an approximate volume for the droplet inclusions is defined in terms of its scalar invariants, and a set of time evolution equations is proposed, which was intended to conserve the approximate volume related to the anisotropy tensor, *cf.* Chap. 2. However, this is a quite difficult task, which was fully accomplished only recently by Edwards and Dressler (2003) adopting the methodology proposed by Edwards et al. (2003). The Doi-Ohta Model and the model of Almusallam et al. (2000) have been invoked in several instances to recover morphological properties of polymer blends from rheological measurements (see, *e. g.* Jansseune et al., 2000, 2001). The idea of these works is to measure viscometric material functions (*e. g.* transient and steady-state shear stresses and first normal stress differences) which can be linked to an orientation angle via a stress-optical rule. Then, a rheological blend model such as the Maffettone Minale Model, the Doi-Ohta Model, or the model of Almusallam et al. (2000) is invoked to obtain the average size of the dispersed droplets (Jansseune et al.,

2000). To conclude this section, we summarize some recent experimental work on single droplet deformation in complex fluids which has been published in the 1990s.

Delaby et al. (1994) investigated droplet deformation in polymer blends during uniaxial stretching flow focusing on the influence of the viscosity ratio in the regime of negligible interfacial tension. Their method has been developed for working directly with polymer melts in the high temperature regime. It involves observation of the elongated droplets at room temperature after extensional flow at high temperature in the molten state and quenching. However, compared to the Couette, four-roll-mill, or opposed jet devices the method of Delaby et al. (1994) is rather impractical since it requires one to elongate and quench several specimens at various elongation strains to study time dependent effects. The measurements of Delaby and coworkers considered the time-dependent deformation of single polyethylene droplets with radius of approximately $100\mu\text{m}$ in a polystyrene specimen in constant strain rate uniaxial extensional flow with a viscosity ratio¹ between 0.005 and 13. Iza et al. (2001) studied the rheology of compatibilized immiscible viscoelastic polymer polystyrene/polyethylene blends. They performed dynamic, steady shear, and transient experiments to probe the effect of interfacial modification on the rheological behavior. The presence of the copolymer was observed particularly in transient experiments after start up of shear flow. Vinckier et al. (1997) investigated the response of semi-concentrated model blends (10% dispersed phase), consisting of slightly viscoelastic polymers, on a step-wise increase in shear rate and observed a deformation of droplets into fibrils. Similar studies have been performed by Lacroix et al. (1999) in shear and elongational flows for several polymer blends and the results have been compared with the Doi-Ohta Model (cf. above). Experimental measurements of droplet deformation in uniaxial elongational flow have been reported by Chin and Han (1979) who used a conical flow channel and injected single droplets along the central axis, where the flow is uniaxial but the strain rate experienced by a single droplet changes during time as it moves through the channel.

Starting from 1998, Guido and coworkers have published a series of articles in which an accurate characterization of the behavior of micro-droplets in various types of shear flows is given. The materials which are adopted in the experiments of Guido and coworkers are polyisobutene and polydimethylsiloxane at room temperature and the size of the droplets is approximately $50-100\mu\text{m}$. Guido and Villone (1998) correlated droplet images taken along the shear and the vorticity direction and presented independent measurements of the three semi-axis of an ellipsoidal drop in steady shear for Newtonian fluid components. Though the experiments of Guido and Villone (1998) were performed in a shear rheometer the viscoelastic response of the droplet phase was not measured because the focus was mainly on the characterization of the full ellipsoidal shape. In Guido et al. (2003a,b) single droplet dynamics in a non-Newtonian Boger fluid is reported and it is

¹The viscosity ratio is defined as the ratio of disperse phase and matrix phase zero-shear viscosity.

found that the elasticity of the matrix phase decreases the steady state orientation angle of the droplet with respect to a Newtonian matrix fluid. Earlier, Levitt et al. (1996) performed similar experiments for non-Newtonian blends detecting a so-called droplet widening effect for start-up of simple shearing flow, i.e., an increase of the vorticity axis of the droplet with respect to its equilibrium value. These authors tried to find correlations of drop deformation with the elastic bulk properties of the blend components.

1.2. A Simple Toy Model

In this volume we construct flow equations for emulsions which take into account physical mechanisms influencing their rheology. To become familiar with some common properties of these equations it is instructive to introduce a simple Toy Model which shares some properties with these models and to solve the Toy Model for simple shearing flow, which is done analytically. Furthermore, the model constitutes a good test for the computer codes to be developed later.

Lets study a dilute emulsion of two Newtonian liquids of equal viscosity which is considered as a continuum with constant density, each particle of it containing an ensemble of disperse phase droplets with equal size. It is assumed that the droplets deform into ellipsoids in the flowing emulsion and that break-up and coalescence do not occur. The volume fraction of disperse phase is ϕ , the droplet radius is R , and interfacial tension of the emulsion components is Γ' . The elastic modulus of the emulsion is defined as $\Gamma = \Gamma'/R$, i. e. interfacial tension over droplet radius. For this equi-viscosity emulsion we introduce the following set of model equations

$$\nabla \cdot \mathbf{v} = 0, \quad (1.1a)$$

$$\text{Re} \frac{D\mathbf{v}}{Dt} = -\nabla p + \nabla \cdot \boldsymbol{\sigma}, \quad (1.1b)$$

$$\text{De} \frac{D\mathbf{S}}{Dt} = \text{De} (\mathbf{S} \cdot \mathbf{L}^T + \mathbf{L} \cdot \mathbf{S}) + f_1 \phi \left(\mathbf{S} - \frac{3}{I_2} \mathbf{1} \right), \quad (1.1c)$$

where ∇ is the Nabla operator for derivative with respect to space and $D \cdot /Dt$ denotes the material derivative. Equation (1.1a) is the continuity equation for an incompressible medium, where \mathbf{v} denotes the macroscopic velocity field of the flowing emulsion. Equation (1.1b) is the Cauchy momentum balance equation for the velocity field, where Re is the Reynolds number, p is the isotropic pressure, and $\boldsymbol{\sigma}$ is the extra stress tensor. The extra-stress tensor is given with Eq. (1.1d), below. Equation (1.1c) is the droplet shape tensor equation for the deforming droplets. In this equations \mathbf{S} is a positive definite second rank tensor, $\mathbf{L}^T = \nabla \mathbf{v}$ is the transpose of the velocity gradient tensor, $f_1 < 0$ is a phenomenological parameter, I_2 is the second invariant of the droplet shape tensor,

De is the Deborah number, and $\mathbf{1}$ denotes the unit tensor. With the value $f_1 = -16/35$ the droplet shape tensor equation is consistent with the Taylor Theory for single droplet deformation (Taylor, 1932, 1934). The Eigenvalues of the droplet shape tensor are the squared semi-axis of the deforming ellipsoidal droplets and the Eigenvectors are the directions of the semi-axis with respect to a fixed coordinate system. Equation (1.1c) is such that the determinant of the droplet shape tensor is constant, $\det \mathbf{S} = 1$, which reflects incompressibility of the disperse phase fluid. Equation (1.1c) is the Maffettone-Minale Model for equi-viscosity conditions. To close the above set of flow equations we need to specify the extra stress tensor, $\boldsymbol{\sigma}$.

The extra stress tensor in the Cauchy momentum balance equation is defined as

$$\boldsymbol{\sigma} = \phi \left(I_1 \mathbf{S} - \mathbf{S} \cdot \mathbf{S} - \frac{2}{3} I_2 \mathbf{1} \right), \quad (1.1d)$$

where I_1, I_2 denote the first and second invariant of the droplet shape tensor, respectively. This expression for the extra stress tensor will be derived in Chap. 3. The contribution of the matrix and disperse phase viscosity is neglected in the expression of the extra stress tensor, for simplicity. The above model is a set of partial differential equations for the velocity, pressure, and droplet shape tensor field which can be solved for arbitrary flow geometries, defined through initial and boundary conditions for the unknown fields. A simple analytical solution of the Toy Model may be obtained for a quiescent emulsion. In deed for $\mathbf{L} = \mathbf{0}$ we recover ellipsoidal droplets, *i. e.* $\mathbf{S} = \mathbf{1}$.

Before evaluating the Toy Model we need to comment on the volume preservation constraint ($\det \mathbf{S} = 1$) and the assumption of ellipsoidal droplets inherent to Eq. (1.1c) since these two aspects are basic ingredients of the descriptions to be developed later. The approximation of ellipsoidal droplets has been investigated experimentally for droplets with diameters between 40 and 500 μm by Guido and Villone (1998) and by Hu and Lips (2003) in simple shear flow and in planar hyperbolic flow, respectively. It is found that even close to break-up droplets can be appropriately circumscribed with ellipsoids. The use of the droplet shape tensor in Eq. (1.1c) implies that this is also true on much smaller length scales than those examined experimentally.

The model equations (1.1) are written down in dimensionless form. To obtain physical properties the dimensionless quantities are to be scaled: extra stress tensor (pressure) with the elastic modulus, $\Gamma \boldsymbol{\sigma}$ (Γp), droplet shape tensor with the equilibrium radius of droplets in the undeformed state $R^2 \mathbf{S}$, and the velocity gradient tensor with a characteristic time scale of droplet retraction \mathbf{L}/λ_S , where λ_S is a characteristic time scale of the interface, in the following named relaxation time. Then the Reynolds and the Deborah number are

$$\text{Re} = \frac{U \rho L}{\Gamma \lambda_S}, \quad (1.2a)$$

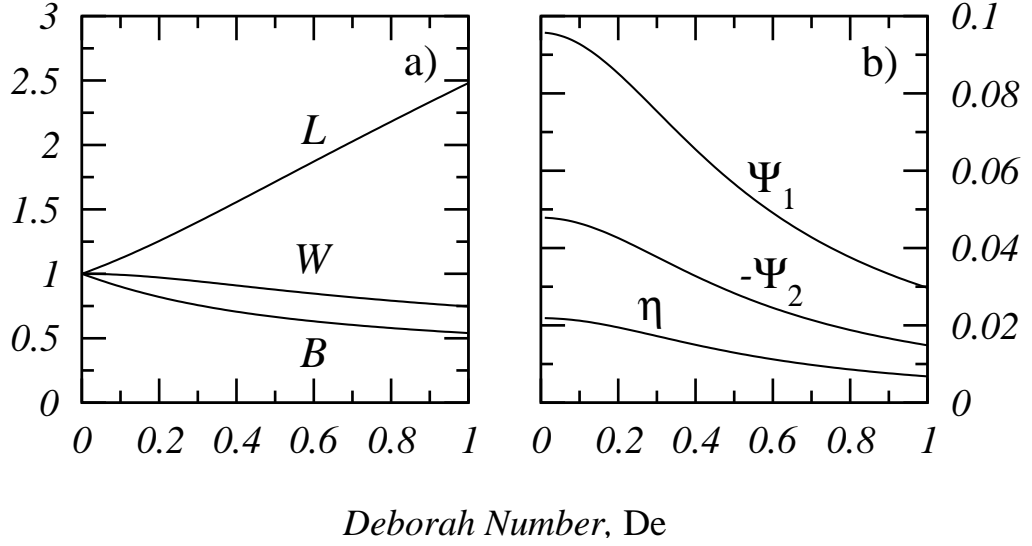


Figure 1.1.: Morphological and Viscometric properties according to the Toy Model for steady shear flow ($\phi = 0.01$ $f_1 = -16/35$).

$$\text{De} = \lambda_S \sqrt{2\mathbf{D} : \mathbf{D}^T}, \quad (1.2b)$$

where U is a characteristic velocity, L a characteristic length scale of the flow problem, $\mathbf{D} = 1/2(\mathbf{L} + \mathbf{L}^T)$ is the rate of deformation tensor, and ":" denotes contraction of second-rank tensors. In the following we solve the Toy Model for simple shear flow as used in rheological characterization and we discuss model predictions for the droplet shape and the viscometric functions.

For steady shear flow, $\mathbf{v} = v_1(x_2)\mathbf{e}_1$ (e. g. in the cone-and-plate geometry for standard rheometers) the continuity equation (1.1a) and the Cauchy momentum balance (1.1b) are trivial and the droplet tensor equation (1.1c) reduces to a set of algebraic third order equations. These can be solved analytically to give

$$\mathbf{S} = \frac{1}{(\tilde{f}_1)^{1/3}} \begin{pmatrix} f_1^2 + 2\text{De}^2 & f_1\text{De} & 0 \\ f_1\text{De} & f_1^2 & 0 \\ 0 & 0 & f_1^2 \end{pmatrix}, \quad (1.3)$$

where $\tilde{f}_1 = f_1^4(f_1^2 + \text{De}^2)$. The Eigenvalues of this matrix read

$$\lambda_{1,2} = \frac{1}{S_{33}^2} \pm \sqrt{\frac{\text{De}^2 S_{12}^2}{f_1^2} + S_{12}^2}, \quad (1.4)$$

$$\lambda_3 = S_{33}, \quad (1.5)$$

and are the squared semi-axis of the deformed droplets. Evaluating these expressions

for the Eigenvalues with Eq. (1.3) gives the droplet semi-axis.

$$L^2 = \frac{f_1^2 + \text{De}^2 + \text{De}\sqrt{f_1^2 + \text{De}^2}}{(\tilde{f}_1)^{1/3}}, \quad (1.6a)$$

$$B^2 = \frac{f_1^2 + \text{De}^2 - \text{De}\sqrt{f_1^2 + \text{De}^2}}{(\tilde{f}_1)^{1/3}}, \quad (1.6b)$$

where L , B are the major and the minor droplet axis in the shearing plane, respectively. The droplet axis perpendicular to the shearing plane is $W = \sqrt{S_{33}} < 1$. The components of the extra stress tensor can be calculated easily from Eq. (1.1d) using the solution (1.3). With $I_2 = 3/S_{33}$ one obtains

$$\sigma_{12} = \frac{\phi f_1^{1/3} \text{De}}{(f_1^2 + \text{De}^2)^{2/3}}, \quad N_1 = \frac{2\phi \text{De}^2}{f_1^{2/3} (f_1^2 + \text{De}^2)^{2/3}}, \quad N_2 = -\frac{1}{2} N_1. \quad (1.7)$$

We see that the model allows to predict the non-equilibrium droplet shapes as well as the viscoelastic response of the emulsion due to the elastic interface between the fluid phases. The morphological and viscometric properties according to Eqs. (1.6) (1.7) are shown in Fig. 1.1, where the first and second normal stress coefficients are defined as $\Psi_1 = N_1/\text{De}^2$ and $\Psi_2 = N_2/\text{De}^2$, respectively.

Inspecting Eqs. (1.6) we see that the major droplet axis and the minor droplet axis are always larger and smaller than one, respectively. The vorticity axis is also smaller than one which means that under equi-viscosity conditions the droplets deform into cigar shaped particles, in the following named prolate. This is consistent with experimental data and theoretical studies of Taylor (1932, 1934). Therefore, for thick disperse phase fluids, the prediction of the Toy Model is in qualitative agreement with experimental data. For thin disperse phase fluids one expects pancake shaped droplets, named hereafter oblate. With the Toy Model it is not possible to describe these droplet configurations. From Eqs. (1.7) we learn that the Toy Model allows to predict the viscoelastic response of the emulsion which is due to the elastic interface. It allows to describe transient as well as steady state deformations and it can be applied to any flow, since it is expressed in terms of the arbitrary velocity field. The ratio of normal stress differences is very large compared to typical values of -0.1 for polymer melts. Note that the Toy Model is only for Newtonian emulsion components and it does not account for break-up and coalescence phenomena. Moreover, it is not immediately clear how oblate droplet configurations can be modeled and how matrix viscoelasticity influences droplet deformation.

The problems of the Toy Model discussed in the preceding paragraph are a shortcoming of almost all theoretical works on emulsion rheology, and in particular of the works dealing with the droplet shape tensor theory and the anisotropy tensor theory. In these models the viscoelastic response of the emulsion is exclusively due to the elastic interface

between the components. It is clear that the limitation of Newtonian emulsion components is a very severe one since commercial emulsions are made of high molecular weight polymers with a characteristic non-Newtonian flow behavior. If the emulsion consists of a continuous matrix of one polymer with microscopic droplets of a second phase, the viscoelastic response is due to the matrix and not just the interface. Thus one should use a description for emulsions consisting of a viscoelastic matrix phase with microscopically small droplet inclusions of a second phase. In this volume we give a systematic approach to the description of highly viscous emulsions, based on non-equilibrium Thermodynamics. We show how the deficiencies of the Toy Model and other emulsion models can be overcome. To conclude this chapter we give a short summary of the treatise.

In Chap. 2 we introduce a master equation of non-equilibrium Thermodynamics which allows us to derive flow equations for viscoelastic fluids. We use this approach to obtain dynamic equations for a complex fluid with a microstructure described in terms of a second-rank tensor, *e. g.* a polymer solution. From this set of time evolution equations we construct then flow equations for a viscoelastic fluid with a volume preserving microstructure, *e. g.* droplets of a Newtonian liquid in an Eulerian fluid. The descriptions derived in Chap. 2 are for a compressible and non-isothermal medium.

Chapter 3 is dedicated to the development of thermodynamically consistent models for highly viscous emulsions to consider various effects which are not taken into account in the Toy Model. We are not so much striving for quantitative accuracy in model prediction, but are instead attempting to develop an understanding for what type of effects are necessary in order to render an accurate physical understanding of highly viscous emulsions. Specifically, in Sec. 3.1 we focus on emulsions with a viscoelastic matrix phase, we take into account the effect of matrix deformation on droplet shape, and we consider both prolate and oblate droplet configurations. In Sec. 3.2 the model is extended to incorporate phenomena of break-up and coalescence of droplets. This is done through the introduction of a droplet distribution function to quantify the size of the droplets. In Secs. 3.3 and 3.4 we point out how emulsions containing surface active molecules and emulsions with a high volume fraction of disperse phase are to be modeled in the framework of non-equilibrium Thermodynamics.

In Chap. 4 the emulsions models are solved for transient and steady flows as encountered in the cone-and-plate rheometer, elongational rheometers, and in the stagnation point of the four-roll-mill apparatus, *i. e.* we study flows with a homogeneous rate of deformation history. We perform calculations for the models with matrix viscoelasticity and break-up and coalescence. This is done to examine the extent to which matrix viscoelasticity and droplet break-up and coalescence affect the rheology and morphological characteristics of highly viscous emulsions. We draw conclusions about the importance of matrix viscoelasticity and about the size distribution of droplets for emulsion rheology. A preliminary fit of the models with rheological and morphological data of emulsions is

postponed to the Appendix.

In Chap. 5 we solve the model equations for steady laminar flows in channels, tubes, and in the gap between concentric cylinders. This is done to demonstrate that the models are suitable for CFD of highly viscous emulsions. The relationship with the homogeneous flow calculations of Chap. 4 is worked out and the wall viscometric emulsion properties are discussed as a function of wall shear rate. We discuss droplet dispersion in annular flows and we draw some conclusions for emulsion processing. The last Chap. 6 summarizes the main results and gives an outlook.

2. Theory

A mathematically precise way to describe the flow of complex fluids is afforded by non-equilibrium Thermodynamics. We introduce first a master equation to derive flow equations for complex fluids and the Volterra calculus of functionals as a necessary mathematical tool. Then we consider complex fluids with different microstructural characteristics and we continue to derive flow equations for these complex fluids. We will obtain two sets of flow equations which describe the matrix and the droplet phase of highly viscous emulsions.

2.1. Master Equation

The structural equation of the Hamiltonian bracket formalism is (Beris and Edwards, 1994)

$$\frac{dF}{dt} = \{F, H\} + [F, H], \quad (2.1)$$

where $F = F[a, b, \dots]$ is an arbitrary functional (global quantity) of variables a, b, \dots , $d \cdot / dt$ is the total time derivative, $\{\cdot, \cdot\}$ is a Poisson bracket, $[\cdot, \cdot]$ is a dissipation bracket, and the functional $H = H[a, b, \dots]$ is the system Hamiltonian (generator of the dynamics), depending on the variables. Equation (2.1) is a special case of the more general GENERIC expression of Grmela and Öttinger (1997); Öttinger and Grmela (1997). The relationship with the master equation of that formalism is worked out in Edwards (1998) and Edwards et al. (1998). The variables a, b, \dots which are adopted to describe the system's dynamics are defined on an operational space, \mathcal{P} . The brackets appearing in the above structural equation have well defined properties to ensure that the dynamics of the system obeys Hamilton's principle of least action and the Laws of Thermodynamics. The Poisson bracket is bilinear, it is antisymmetric, and it satisfies the Jacobi identity¹. It specifies the reversible contribution to the dynamics of the functional F . The dissipation bracket (Beris and Edwards, 1994) is constructed in a

¹ $\{F, \{G, H\}\} + \{H, \{F, G\}\} + \{G, \{H, F\}\} = 0$

way to ensure that the First and Second Law of Thermodynamics are satisfied and that the total mass is conserved. It determines the irreversible contribution to the overall dynamics of the functional F .

If one applies Eq. (2.1) to discrete particle dynamics the variables a, b, \dots are generalized coordinates, F is a function of these coordinates, and we adopt the calculus of partial derivatives. When describing a continuum, the variables a, b, \dots are fields of arbitrary tensorial order, F is a functional of these fields, and the calculus of functional derivatives (Volterra calculus) is adopted. In this case a, b, \dots are thermodynamic variables, *i. e.* statistical mechanical averages over all constituent molecules and other microstructural components which constitute a single fluid particle of the continuum. Basic principles of the Volterra calculus are summarized in the next section.

2.2. Functional Calculus

An arbitrary functional $F[a, b, \dots]$ of the dynamical variables represents a global system property (*e. g.* the total momentum) and it is defined in terms of the corresponding local quantity (*e. g.* the momentum density) through the equation

$$F[a, b, \dots] = \int_{\Omega'} f(a, \nabla a, b, \nabla b, \dots) d^3x, \quad (2.2)$$

where Ω' is an integration domain with fixed boundaries. The functional F is only allowed to depend implicitly on ∇a and ∇b since it is a global system property. The total time derivative of the arbitrary functional appearing in the structural equation (2.1) is then given as

$$\frac{dF}{dt} = \int_{\Omega'} \left[\frac{\delta F}{\delta a} \frac{\partial a}{\partial t} + \frac{\delta F}{\delta b} \frac{\partial b}{\partial t} + \dots \right] d^3x = \left\langle \frac{\delta F}{\delta a}, \frac{\partial a}{\partial t} \right\rangle + \left\langle \frac{\delta F}{\delta b}, \frac{\partial b}{\partial t} \right\rangle + \dots, \quad (2.3)$$

where $\partial \cdot / \partial \cdot$ and $\delta \cdot / \delta \cdot$ denote the partial and the Volterra derivative, respectively. Both derivatives have to belong to the same operating space, \mathcal{P} , in order to form a proper inner product, $\langle \cdot, \cdot \rangle$, as it appears on the right hand side of Eq. (2.3). For the Volterra derivative of an arbitrary functional, F , with respect to a system variable with arbitrary tensorial order, a , we have

$$\frac{\delta F}{\delta a} = \mathbf{\Pi}^a \left(\frac{\partial f}{\partial a} - \nabla \cdot \frac{\partial f}{\partial (\nabla a)} \right) \in \mathcal{P}, \quad (2.4)$$

where $\mathbf{\Pi}^a$ is a projection operator which ensures, that $\delta F/\delta a$ and $\partial a/\partial t$ belong to the same operating space, \mathcal{P} (Beris and Edwards, 1990a, 1994). For an unconstrained variable, a , $\mathbf{\Pi}^a$ is the identity operation. The unconstrained Volterra derivative is obtained from taking the variation of the functional F with respect to a and it represents the Euler/Lagrange equation resulting from the variation of the functional F with respect to the variable a .

For a constrained variable $\mathbf{\Pi}^a$ is not anymore the identity operation and one has to define a proper Volterra derivative so that $\delta F/\delta a$ and $\partial a/\partial t$ belong to the same operational space. The incompressibility of the material is an example for such a constraint since it enforces the momentum density field, $\mathbf{M}(\mathbf{r}, t) = \rho \mathbf{v}(\mathbf{r}, t)$, to be divergence free in the domain Ω' , *i. e.* $\nabla \cdot \mathbf{M} = 0$ in Ω' . By applying the Weyl/Hodge theorem it can be shown that for this constraint the projection operation is $\mathbf{\Pi}^{\mathbf{M}}(\mathbf{a}) = \mathbf{a} - \nabla p$, where $\mathbf{a} \in \mathbb{R}^3$ is an arbitrary vector and the pressure p is a scalar function which satisfies an elliptic (Poisson) equation, subject to flux (von Neumann) boundary conditions for a given vector, \mathbf{a} (Beris and Edwards, 1994). Similarly, it is also possible to impose constraints on other system variables, *e. g.* the structural tensorial variables which are adopted to describe the deformation of complex fluids. This is the topic of the next section where we introduce various constraints for a second-rank tensorial variable, \mathbf{C} .

Before proceeding with the introduction of microstructural constraints we wish to comment on the macroscopic and the microscopic interpretation of internal variables. If the fluid is ideally elastic (*i. e.* for a purely conservative system) deformation is appropriately described in terms of the Left-Cauchy-Green Tensor, *i. e.* $\mathbf{C} = \mathbf{F} \cdot \mathbf{F}^T$. However, if the fluid is viscoelastic, (*i. e.* for non-vanishing dissipation) \mathbf{C} cannot be identified with a deformation tensor and a microstructural interpretation has to be adopted. In this case $\mathbf{C} = \int \mathbf{R}\mathbf{R} d^3r$ is interpreted as a configuration tensor, *i. e.* the second moment of the end-to-end vector of the microstructural constituents of the fluid, where the integration is over all accessible configurations of the macromolecule. This means that the macroscopic interpretation of \mathbf{C} (as a deformation tensor) is related to ideally elastic material behavior and the microscopic interpretation (as a configuration tensor) is related to non-ideal, *i. e.* viscoelastic behavior. In what follows we refer to \mathbf{C} as the deformation or conformation tensor. However, the difference between the two quantities should be kept in mind.

2.3. Microstructural Constraints

Our first task is to introduce the scalar invariants of symmetric and positive definite second rank tensorial variables. Since every scalar constraint on a positive definite

second rank tensor is represented as a function of the scalar invariants, it suffices to focus on the invariants. For a second rank tensor, \mathbf{C} , they are defined as follows

$$I_1 = C_{\alpha\alpha}, \quad (2.5a)$$

$$I_2 = \frac{1}{2}(C_{\alpha\alpha}C_{\beta\beta} - C_{\alpha\beta}C_{\beta\alpha}), \quad (2.5b)$$

$$I_3 = \det \mathbf{C}. \quad (2.5c)$$

We have introduced the Einstein summation convention which will be adopted throughout the thesis. Let us next think about the importance of these constraints for the modeling of complex fluids which are described in terms of \mathbf{C} .

For complex fluids of long, flexible molecules (*e. g.* in polymer melts, polymer solutions, or in the matrix of a highly viscous emulsion) the molecules will extend and orient in an externally imposed flow field. Such a fluid possesses an *unconstrained microstructure*, since the response to an external flow field will consist in a variation of the internal variable which conserves only its positive definite character. We proceed to look at microstructural constraints for complex fluids related to the scalar invariants of second rank tensors. We start with the constraints related to the first and the second scalar invariant.

For suspensions of rigid molecules or suspensions of rigid particles (*e. g.* liquid crystals) the microstructure is different in nature from that of flexible macromolecular solutions or melts since the molecules are inextensible. In this case we are dealing with a *length preservation* (or inextensibility) constraint on the structural variable, since the molecules are stiff and they are only allowed to change their orientation and motion in response to an external flow field. In this case the microstructural constraint is $I_1 = 1$. Alternatively, the microstructural inclusions in a fluid may be deformable and orientable but the surface area of the microstructural constituents cannot change under flow. We refer to this a situation as a *surface preservation* constraint on the structural variable. This situation is realized, *e. g.*, for the interface of two co-continuous phases or an ensemble of deformable micro-platelets which orient and deform in a flow field. Thus, for the surface preservation constraint we have $I_2 = 1$. We turn our attention to the constraint related to the third invariant, the volume preservation constraint.

Special attention is to be devoted to the constraint related to the third scalar invariant, the *volume preservation* constraint. This constraint is relevant for the modeling of highly viscous emulsions and it has been introduced for the modeling of emulsions in Maffettone and Minale (1998) and for polymeric fluids in (Ait-Kadi et al., 1999). Indeed, if the microstructure consists of volume preserving units which can deform and orient under flow, the microstructure obeys the constraint

$$I_3 = 1, \quad (2.6)$$

as we have already seen in the Toy Model. The implications of such a constraint for the modeling of complex fluids are important and are investigated systematically in the subsequent chapters.

As already mentioned at the beginning of this section every scalar constraint of a microstructural variable can be expressed as a function of its scalar invariants. Almusallam et al. (2000), *e. g.*, adopted a surface orientation tensor, \mathbf{q} , to describe the shape of ellipsoidal droplets in highly viscous emulsions. The approximate volume of the droplets, described in terms of the invariants of the surface orientation tensor is then defined as

$$V_d = \frac{4}{3\pi\sqrt{27 + 30\sqrt{3}}} \frac{1}{\sqrt{I_3(10I_2^{3/2} + I_1^3)}} \quad (2.7)$$

i. e. the volume is expressed in terms of the scalar invariants, $I_i, i \in \{1, 2, 3\}$ of the anisotropy tensor, \mathbf{q} . Almusallam et al. (2000) proposed a time evolution equation for \mathbf{q} which was intended to conserve the approximate volume of the droplet, a task which was only accomplished by Edwards and Dressler (2003). In the following droplet shapes are described in terms of a droplet shape tensor, \mathbf{S} , introduced with the Toy Model, Sec. 1.2.

To give a satisfactory description of complex fluids it is essential that the time evolution equations for these fluids are constructed in a way to reflect and to conserve the inherent characteristics of the microstructure. In the case of the volume preservation constraint, *e. g.*, the volume of the internal microstructure remains constant in space and time, for all deformation undergone by the material. Therefore, the constraint on the microstructure is to be used as basic ingredient when developing time evolution equations for complex fluids. Only this allows to give a reasonable description of their dynamics. In Sec. 2.4 we show how appropriate time evolution equations can be derived from the master equation.

2.4. Flow Equations

2.4.1. Unconstrained Microstructure

We illustrate the derivation of thermodynamically consistent time evolution equations for complex fluids which are described in terms of the classical hydrodynamic fields and an unconstrained, positive definite second rank tensorial variable. First, we specify the operating space with the dynamical variables, next we write down the Poisson and dissipation brackets, and finally we derive the resulting time evolution equations for the fluid.

We need to introduce these concepts here because they are required in the subsequent sections to obtain flow equations for fluids with a volume preserving microstructure. In the derivation of the flow equations we follow standard procedure in Beris and Edwards (1990a, 1994); Edwards and Beris (1991a, 1992).

Operating space

Our first task is to introduce the operating space for describing flow of a complex fluid with an unconstrained structural variable (Beris and Edwards, 1994). For a complex fluid with an unconstrained structural variable we adopt the following operating space for the spatial (Eulerian) description of fluid flow

$$\mathcal{P} = \begin{cases} \rho(\mathbf{r}, t) & \in \mathbb{R}^+ \\ s(\mathbf{r}, t) & \in \mathbb{R}^+ \\ \mathbf{M}(\mathbf{r}, t) = \rho \mathbf{v}(\mathbf{r}, t) & \in \mathbb{R}^3, \mathbf{n} \cdot \mathbf{M} = 0 \text{ on } \partial\Omega' \\ \mathbf{C}(\mathbf{r}, t) & \in \mathbb{R}^{3 \times 3T}. \end{cases} \quad (2.8)$$

This operating space consists of the hydrodynamic fields, namely the mass density field, $\rho(\mathbf{r}, t)$, the entropy density field $s(\mathbf{r}, t)$, the momentum density field $\mathbf{M}(\mathbf{r}, t) = \rho \mathbf{v}(\mathbf{r}, t)$, and an unconstrained structural variable $\mathbf{C}(\mathbf{r}, t) = \rho \mathbf{c}(\mathbf{r}, t)$. The system variables are defined on a domain Ω' with fixed boundaries $\partial\Omega'$. The mass density and the entropy density are scalar variables, the momentum density field is a vectorial variable, and the structural variable is a second rank contravariant tensorial variable being symmetric and positive definite. We mention that there is no generally accepted rule whether the internal variable, \mathbf{C} , should be a contravariant, a covariant, or a mixed second order tensor. Yet the transformation rule of the internal variable influences the time evolution equation of the internal variable and the form of the extra stress tensor so that we have to be careful in specifying that quantity (Beris and Edwards, 1994).

The Volterra derivatives with respect to the system variables are defined through Eq. (2.4) where the projection $\mathbf{\Pi}^a$ is simply the identity operation since all system variables are unconstrained. In particular, for the Volterra derivative of F with respect to the unconstrained structural variable we have

$$\frac{\delta F}{\delta \mathbf{C}} = \mathbf{\Pi}^{\mathbf{C}} \left(\frac{\partial f}{\partial \mathbf{C}} \right) = \frac{\partial f}{\partial \mathbf{C}} - \nabla_\alpha \frac{\partial f}{\partial (\nabla_\alpha \mathbf{C})}, \quad (2.9)$$

i. e. $\mathbf{\Pi}^{\mathbf{C}}$ is the identity operation. For a volume preserving microstructure the above relationship has to be modified in order to take into account the volume preservation constraint which is imposed on the structural variable (*cf.* Sec. 2.4.2). After having specified the operational space and the Volterra derivatives of arbitrary functionals on \mathcal{P} we write down the two brackets appearing in the structural equation (2.1).

Poisson Bracket

Let us now consider the reversible dynamics of the complex fluid, fully described in terms of the Poisson bracket. Looking at the operating space of Eq. (2.8) we see that its elements are non-canonical variables the canonical ones being material coordinates and conjugate momenta of single fluid particles.

The canonical Poisson bracket in the material (Lagrangian) description of fluid flow is

$$\{F, G\}_L = \int_{\Omega} \left(\frac{\delta F}{\delta Y_{\alpha}} \frac{\delta G}{\delta \Pi_{\alpha}} - \frac{\delta F}{\delta \Pi_{\alpha}} \frac{\delta G}{\delta Y_{\alpha}} \right) d^3x, \quad (2.10)$$

where the subscript L refers to the material description. In the above integral Ω represents the system volume with fixed boundaries, $\mathbf{Y}(\mathbf{r}, t)$ denotes the material coordinate, and $\mathbf{\Pi}(\mathbf{r}, t) = \delta L / \delta \dot{\mathbf{Y}}(\mathbf{r}, t) = \rho_0(\mathbf{r}) \delta \mathbf{Y}(\mathbf{r}, t) / \delta t$ is the conjugate momentum vector field, L being the Lagrangian and $\rho_0(\mathbf{r})$ the initial density distribution of the fluid. In order to arrive at the spatial (non-canonical) Poisson bracket of the ideally elastic medium the material variables, $\mathbf{Y}(\mathbf{r}, t)$, $\mathbf{\Pi}(\mathbf{r}, t)$, have to be transformed to the spatial variables ρ , s , \mathbf{M} , \mathbf{C} . Inserting these representations into the material Poisson bracket (2.10) and considering the anti-symmetry of the Poisson bracket one arrives at the non-canonical bracket. The result of this formal exercise is (Beris and Edwards, 1990a,b, 1994; Edwards and Beris, 1991a,b; Edwards et al., 1991)

$$\begin{aligned} \{F, G\}_E = & - \int_{\Omega'} \left[\frac{\delta F}{\delta \rho} \nabla_{\beta} \left(\frac{\delta G}{\delta M_{\beta}} \rho \right) - \frac{\delta G}{\delta \rho} \nabla_{\beta} \left(\frac{\delta F}{\delta M_{\beta}} \rho \right) \right] d^3x \\ & - \int_{\Omega'} \left[\frac{\delta F}{\delta s} \nabla_{\beta} \left(\frac{\delta G}{\delta M_{\beta}} s \right) - \frac{\delta G}{\delta s} \nabla_{\beta} \left(\frac{\delta F}{\delta M_{\beta}} s \right) \right] d^3x \\ & - \int_{\Omega'} \left[\frac{\delta F}{\delta M_{\gamma}} \nabla_{\beta} \left(\frac{\delta G}{\delta M_{\beta}} M_{\gamma} \right) - \frac{\delta G}{\delta M_{\gamma}} \nabla_{\beta} \left(\frac{\delta F}{\delta M_{\beta}} M_{\gamma} \right) \right] d^3x \\ & - \int_{\Omega'} \left[\frac{\delta F}{\delta C_{\alpha\beta}} \nabla_{\gamma} \left(\frac{\delta G}{\delta M_{\gamma}} C_{\alpha\beta} \right) - \frac{\delta G}{\delta C_{\alpha\beta}} \nabla_{\gamma} \left(\frac{\delta F}{\delta M_{\gamma}} C_{\alpha\beta} \right) \right] d^3x \quad \boxed{\text{I1}} \\ & - \int_{\Omega'} C_{\gamma\alpha} \left[\frac{\delta G}{\delta C_{\alpha\beta}} \nabla_{\gamma} \left(\frac{\delta F}{\delta M_{\beta}} \right) - \frac{\delta F}{\delta C_{\alpha\beta}} \nabla_{\gamma} \left(\frac{\delta G}{\delta M_{\beta}} \right) \right] d^3x \quad \boxed{\text{I2}} \\ & - \int_{\Omega'} C_{\gamma\beta} \left[\frac{\delta G}{\delta C_{\alpha\beta}} \nabla_{\gamma} \left(\frac{\delta F}{\delta M_{\alpha}} \right) - \frac{\delta F}{\delta C_{\alpha\beta}} \nabla_{\gamma} \left(\frac{\delta G}{\delta M_{\alpha}} \right) \right] d^3x, \quad \boxed{\text{I3}} \end{aligned} \quad (2.11)$$

where the subscript E indicates spatial description of fluid flow, *i. e.* non-canonical variables. The above bracket shares the properties of a Poisson bracket since it is bilinear,

it is antisymmetric, and it satisfies the Jacobi identity. Let us briefly examine the several integrals in the above dissipation bracket before turning our attention to the dissipation bracket.

The first three integrals in Eq. (2.11) represent the Poisson bracket for the structure-less medium and lead to the conservative classical hydrodynamic equations for the density, entropy and momentum, *i. e.* Euler's equations of ideal fluid flow. The last three integrals have been labeled I1, I2, I3 and they represent the effects of elasticity in the medium. The sum of these integrals is denoted as $\{\cdot, \cdot\}_E^C = \text{I1} + \text{I2} + \text{I3}$ and we call it the **C**-sub-bracket. Only this sub-bracket has to be transformed in Sec. 2.4.2 when we are going to impose the volume preservation constraint (2.6) on the structural variable. The form of the Poisson bracket is determined by the tensorial order of the elements of the operational space, the transformation rule from the material to the spatial variables, and eventual constraints on the elements of the operational space \mathcal{P} , (2.8). It determines the reversible contributions to the time evolution equations of the field variables, the form of the pressure in terms of the thermodynamic potential, and the reversible contributions of the stress tensor in the momentum equation, *i. e.* elastic stresses.

Dissipation Bracket

We come to the specification of the irreversible contribution to fluid flow that is to be expressed in terms of a dissipation bracket. To obtain an appropriate dissipation bracket one starts with a general expression which is consistent with the First and the Second Law of Thermodynamics

$$[F, G]_E = - \int_{\Omega'} \left\{ \Xi \left[\mathbb{L} \left(\frac{\delta F}{\delta \boldsymbol{\omega}}, \nabla \frac{\delta F}{\delta \mathbf{w}} \right); \frac{\delta G}{\delta \mathbf{w}}, \nabla \frac{\delta G}{\delta \mathbf{w}} \right] + \frac{1}{T} \frac{\delta F}{\delta s} \Xi \left[\mathbb{L} \left(\frac{\delta G}{\delta \boldsymbol{\omega}}, \nabla \frac{\delta G}{\delta \mathbf{w}} \right); \frac{\delta G}{\delta \mathbf{w}}, \nabla \frac{\delta G}{\delta \mathbf{w}} \right] \right\} d^3x, \quad (2.12)$$

where $\mathbb{L}[\cdot]$ denotes that the dependence of Ξ is linear with respect to \cdot , $\mathbf{w} = (a, b, \dots, \mathbf{M}, s)$, and $\boldsymbol{\omega} = (a, b, \dots, \mathbf{M})$, *i. e.* $\mathbf{w} = (\boldsymbol{\omega}, s)$, s being the entropy density and $a, b, \dots \equiv (\rho, \mathbf{C})$ the other dynamical variables. The quantities $\delta G/\delta \mathbf{w}$ and $\nabla \delta G/\delta \mathbf{w}$ in the dissipation bracket represent the relaxational and the flux system affinities, respectively and they are coupled through the function Ξ . Determination of the affinities for the set of variables ρ , s , \mathbf{M} , and \mathbf{C} , application of the Curie principle, of the principle of frame indifference, of the material invariance principle, and consideration of local mass and

local momentum conservation, gives the following dissipation bracket

$$\begin{aligned}
 [F, G]_E = & - \int_{\Omega'} B_{\alpha\beta} \nabla_\alpha \frac{\delta F}{\delta s} \nabla_\beta \frac{\delta G}{\delta s} d^3x \\
 & - \int_{\Omega'} Q_{\alpha\beta\gamma\epsilon} \nabla_\alpha \frac{\delta F}{\delta M_\beta} \nabla_\gamma \frac{\delta G}{\delta M_\epsilon} d^3x \\
 & - \int_{\Omega'} R_{\alpha\beta\gamma\epsilon\eta\nu} \nabla_\alpha \frac{\delta F}{\delta C_{\beta\gamma}} \nabla_\epsilon \frac{\delta G}{\delta C_{\eta\nu}} d^3x \quad \boxed{\text{J1}} \\
 & - \int_{\Omega'} \Lambda_{\alpha\beta\gamma\epsilon} \frac{\delta F}{\delta C_{\alpha\beta}} \frac{\delta G}{\delta C_{\gamma\epsilon}} d^3x \quad \boxed{\text{J2}} \\
 & - \int_{\Omega'} P_{\alpha\beta\gamma\epsilon} \left(\nabla_\alpha \frac{\delta F}{\delta M_\beta} \frac{\delta G}{\delta C_{\gamma\epsilon}} - \nabla_\alpha \frac{\delta G}{\delta M_\beta} \frac{\delta F}{\delta C_{\gamma\epsilon}} \right) d^3x \quad \boxed{\text{J3}} \quad (2.13) \\
 & + \int_{\Omega'} B_{\alpha\beta} \frac{1}{T} \frac{\delta F}{\delta s} \nabla_\alpha \frac{\delta G}{\delta s} \nabla_\beta \frac{\delta G}{\delta s} d^3x \\
 & + \int_{\Omega'} Q_{\alpha\beta\gamma\epsilon} \frac{1}{T} \frac{\delta F}{\delta s} \nabla_\alpha \frac{\delta G}{\delta M_\beta} \nabla_\gamma \frac{\delta G}{\delta M_\epsilon} d^3x \\
 & + \int_{\Omega'} R_{\alpha\beta\gamma\epsilon\eta\nu} \frac{1}{T} \frac{\delta F}{\delta s} \nabla_\alpha \frac{\delta G}{\delta C_{\beta\gamma}} \nabla_\epsilon \frac{\delta G}{\delta C_{\eta\nu}} d^3x \quad \boxed{\text{J1}'} \\
 & + \int_{\Omega'} \Lambda_{\alpha\beta\gamma\epsilon} \frac{1}{T} \frac{\delta F}{\delta s} \frac{\delta G}{\delta C_{\alpha\beta}} \frac{\delta G}{\delta C_{\gamma\epsilon}} d^3x, \quad \boxed{\text{J2}'}
 \end{aligned}$$

The integrals containing the internal variable, \mathbf{C} , have been labeled J1, J2, J3, J1', and J2'. Note that the terms J1' and J2' differ from J1 and J2 only through the $1/T \delta F/\delta s$ term. In analogy to the Poisson sub-bracket, $\{\cdot, \cdot\}_E^C$, we define the dissipation sub-bracket, $[\cdot, \cdot]_E^C = J1 + J2 + J3 + J1' + J2'$, as the sum of the integrals containing the structural variable. This sub-bracket will be transformed in the following Sec. 2.4.2 to impose the volume preservation constraint on the structural variable. We continue with a discussion of the single integrals in the dissipation bracket and we examine the coupling between the members of the operational space.

The bracket (2.13) involves all possible couplings not forbidden by the Curie principle which states that only affinities of the same tensorial order can couple with each other. The first and the sixth integral with the phenomenological matrix \mathbf{B} account for an irreversible entropy flux into internal degrees of freedom. The second and the seventh integral with the phenomenological matrix \mathbf{Q} reflect a flux of linear momentum into internal degrees of freedom. The integrals with the phenomenological matrix \mathbf{R} (labeled

J1 and J1') represent dissipation due to spatial inhomogeneities, *i. e.* a flux, of the structural variable. The integrals with the phenomenological matrix Λ (labeled J2 and J2') are dissipation due to a relaxation of the internal microstructure. The remaining integral with the phenomenological matrix \mathbf{P} is a flux-relaxation coupling between the linear momentum and the structural variable and it accounts for the phenomenon of non-affine motion. The minus sign in the integrand of this term arises since the two affinities have different parities under time reversal. Two other couplings are allowed due to the Curie principle, namely $\nabla(\delta F/\delta\rho)$ with itself and with $\nabla(\delta F/\delta s)$. However, for a one component fluid the phenomenological matrices are necessarily zero so that we can omit these terms (Beris and Edwards, 1994). Furthermore, the $(\delta F/\delta\mathbf{M})(\delta G/\delta\mathbf{M})$ and the $(\delta F/\delta\rho)(\delta G/\delta\rho)$ term do not appear in the dissipation bracket due to local momentum and mass conservation. All phenomenological matrices \mathbf{B} , \mathbf{Q} , \mathbf{R} , Λ , \mathbf{P} have to satisfy the principles of frame indifference, the principle of material invariance, and to obey the Onsager/Casimir reciprocal relations. The application of these principles reduces the number of independent phenomenological coefficients in these matrices. For our further analysis we will need symmetry relationships of the form $Q_{\alpha\beta\gamma\epsilon} = Q_{\gamma\epsilon\alpha\beta} = Q_{\beta\alpha\gamma\epsilon} = Q_{\alpha\beta\epsilon\gamma}$.

Reconsidering the non-canonical Poisson bracket and the dissipation bracket, Eqs. (2.13, 2.11), we notice that the structure of both objects depends primarily on the transformation from the canonical to the non-canonical variables and the tensorial order of the elements of \mathcal{P} . To evaluate the Master Equation an appropriate system Hamiltonian has to be known which generates the dynamics of the system.

System Hamiltonian

Let us now introduce the Hamiltonian of the fluid which is obtained from a Legendre Transformation of the Lagrangian (Beris and Edwards, 1994)

$$H[\rho, s, \mathbf{M}, \mathbf{C}] = \int_{\Omega'} \left(\frac{M_\gamma M_\gamma}{2\rho} + e_p(\rho) + u(\rho, s, \mathbf{C}) \right) d^3x. \quad (2.14)$$

From the above expression it is immediately evident that the Hamiltonian quantifies the total system energy consisting of a kinetic energy contribution, an external field potential, $e_p(\rho)$, and a thermodynamic contribution represented by the internal energy density, u . The Volterra derivatives of the Hamiltonian functional can be easily evaluated to give

$$\frac{\delta H}{\delta\rho} = -\frac{M_\gamma M_\gamma}{2\rho^2} + \frac{\partial e_p}{\partial\rho} + \frac{\partial u}{\partial\rho}, \quad (2.15a)$$

$$\frac{\delta H}{\delta s} = -\frac{\partial u}{\partial s} = T, \quad (2.15b)$$

$$\frac{\delta H}{\delta M_\alpha} = \frac{M_\alpha}{\rho} = v_\alpha, \quad (2.15c)$$

$$\frac{\delta H}{\delta C_{\alpha\beta}} = -\frac{\partial u}{\partial C_{\alpha\beta}}. \quad (2.15d)$$

We remark that Eq. (2.14) is a general representation of the total system energy and that the specification of the internal energy contribution is essential to obtain specific descriptions for the fluid. Appropriate expressions for the potential, suitable for the modeling of emulsions, will be introduced in the next chapter.

Flow Equations

We now use the expressions for the Poisson bracket, the dissipation bracket, and the Hamiltonian to derive flow equations from the Master Equation. The two versions of the dynamical equation for F , Eqs. (2.1) and (2.3), together with the brackets (2.11) and (2.13) are compared to obtain the equations of motion for the spatial variables. It is straight forward to identify the following general set of partial differential equations if the arbitrary functional G has been replaced with the Hamiltonian (2.14)

$$\frac{\partial \rho}{\partial t} = -\nabla_\beta (v_\beta \rho), \quad (2.16a)$$

$$\frac{\partial s}{\partial t} = -\nabla_\beta (v_\beta s) + \Sigma, \quad (2.16b)$$

$$\rho \frac{\partial v_\alpha}{\partial t} = -\rho v_\beta \nabla_\beta v_\alpha - \rho \nabla_\alpha e_p - \nabla_\alpha p + \nabla_\beta \sigma_{\alpha\beta}, \quad (2.16c)$$

$$\begin{aligned} \frac{\partial C_{\alpha\beta}}{\partial t} = & -\nabla_\gamma (v_\gamma C_{\alpha\beta}) + C_{\gamma\alpha} \nabla_\gamma v_\beta + C_{\gamma\beta} \nabla_\gamma v_\alpha - \Lambda_{\alpha\beta\gamma\epsilon} \frac{\delta H}{\delta C_{\gamma\epsilon}} + P_{\alpha\beta\gamma\epsilon} \nabla_\gamma v_\epsilon \\ & + \nabla_\gamma \left(R_{\gamma\alpha\beta\epsilon\eta\nu} \nabla_\epsilon \frac{\delta H}{\delta C_{\eta\nu}} \right). \end{aligned} \quad (2.16d)$$

Equation (2.16a) is the continuity equation reflecting local mass conservation. Equation (2.16b) is the entropy balance equation, where the first term on the right hand side is the entropy change due to convection of the fluid particle and Σ is the irreversible entropy production rate (per unit volume) in the system which is given by Eq. (2.19) below. Equation (2.16c) is the momentum balance equation. The form of the extra stress tensor in Eq. (2.16c) is determined through the Poisson bracket and the dissipation bracket

$$\sigma_{\alpha\beta} = 2C_{\beta\gamma} \frac{\delta H}{\delta C_{\alpha\gamma}} + Q_{\alpha\beta\gamma\epsilon} \nabla_\gamma v_\epsilon + P_{\alpha\beta\gamma\epsilon} \frac{\delta H}{\delta C_{\gamma\epsilon}}. \quad (2.17)$$

The first term on the right hand side of Eq. (2.17) represents elastic effects, the second term takes into account viscous dissipation, and the third term represents effects of non-affine motion. The form of the pressure in the momentum balance (2.16c) arises naturally through the form of the Poisson bracket

$$p = -u + \rho \left. \frac{\partial u}{\partial \rho} \right|_{s, \mathbf{C}} + s \left. \frac{\partial u}{\partial s} \right|_{\rho, \mathbf{C}} + C_{\alpha\beta} \left. \frac{\partial u}{\partial C_{\alpha\beta}} \right|_{\rho, s}. \quad (2.18)$$

Equation (2.16d) is the time evolution equation for the internal variable, \mathbf{C} . The first three terms on the left hand side of Eq. (2.16d) describe how the structural variable is convected with the velocity field and they represent Oldroyd's upper convected (Oldroyd-B) derivative for a contravariant second rank tensor. Note that the Oldroyd-B derivative arises naturally from the Poisson bracket (Beris and Edwards, 1994). The remaining three terms account for relaxation, non-affine motion, and translational diffusivity, respectively. The rate of entropy production per unit volume in the system is

$$\begin{aligned} \Sigma = & \frac{1}{T} \nabla_{\alpha} (B_{\alpha\beta} T \nabla_{\beta} T) + \frac{1}{T} Q_{\alpha\beta\gamma\epsilon} \nabla_{\alpha} v_{\beta} \nabla_{\gamma} v_{\epsilon} \\ & + \frac{1}{T} R_{\alpha\beta\gamma\epsilon\eta\nu} \nabla_{\alpha} \frac{\delta H}{\delta C_{\beta\gamma}} \nabla_{\epsilon} \frac{\delta H}{\delta C_{\eta\nu}} + \frac{1}{T} \Lambda_{\alpha\beta\gamma\epsilon} \frac{\delta H}{\delta C_{\alpha\beta}} \frac{\delta H}{\delta C_{\gamma\epsilon}}. \end{aligned} \quad (2.19)$$

In a numerical scheme which computes particular solutions of the set of partial differential equations (2.16) the property $\Sigma \cdot T = [S, H] \cdot T \geq 0$ can be adopted as a consistency requirement to check the positive rate of entropy production within the system.

For the elements of the operational space, \mathcal{P} , the equations of motion Eq. (2.16) represent the most general form for describing the dynamics of a complex continuum without constraints on the tensorial variable, \mathbf{C} . The set of balance equations (2.16) accounts for compressibility of the medium, it is fully non-isothermal, and it allows for elastic and viscous stresses.

A transformation of the bracket (2.11) to its counterpart in terms of a covariant tensorial variable or a second rank mixed tensorial variable is reported in Beris and Edwards (1994). Transformation to a covariant tensor gives the *lower* convected (Oldroyd-A) derivative in the time evolution equation for \mathbf{C} , Eq. (2.16d). Transformation to a *mixed* tensorial variable gives a positive sign in front of integral I2 if index α is transformed to a covariant tensor index and it yields the *mixed* convected time derivative in the time evolution equation for \mathbf{C} .

In order to obtain a specific set of model equations it is necessary to adopt a microstructural interpretation of the structural variable, \mathbf{C} , and to specify the Hamiltonian, H , of the system together with the phenomenological matrices, \mathbf{B} , \mathbf{Q} , $\mathbf{\Lambda}$, \mathbf{P} , \mathbf{R} . It is possible to use established continuum descriptions as a guide for the specification for

the Hamiltonian and the phenomenological matrices (Beris and Edwards, 1994; Dressler et al., 1999), or to adopt statistical mechanics to obtain appropriate expressions.

2.4.2. Volume Preserving Microstructure

In the preceding section we derived a general set of time evolution equations for a complex fluid with a microstructure described in terms of the unconstrained variable, \mathbf{C} . Let us examine now the consequences of imposing the volume preservation constraint on the variable, \mathbf{C} , and understand how the flow equations change. Following ideas that were developed in Edwards et al. (2003) we define a projection which maps the unconstrained variable onto one with constant determinant and we derive Poisson and dissipation brackets for this new variable.

Projection Mapping

It is clear that the microstructural equation (2.16d) describes a spatio-temporal variation of the variable \mathbf{C} which does not conserve its third invariant, since \mathbf{C} is unconstrained. In order to obtain time evolution equations for the microstructural variable that respect the constraint $I_3 = 1$ we introduce a projection which maps the unconstrained variable, \mathbf{C} , onto a tensorial variable which respects the volume preservation constraint, Eq. (2.6). We identify this as a new variable, \mathbf{S} , for which we derive appropriate dynamic equations.

For the mathematical analysis of the constraint (2.6) we adopt the operational space \mathcal{P} , (2.8) and we define the following projection operation

$$P_S[C_{\alpha\beta}] = \frac{C_{\alpha\beta}}{\sqrt[3]{\det \mathbf{C}}} \equiv S_{\alpha\beta}, \quad (2.20)$$

which constrains \mathbf{S} to be of unit determinant, $I_3 = 1$. For the inverse of the structural variable, \mathbf{S}^{-1} , we have

$$S_{\alpha\beta}^{-1} = \sqrt[3]{\det \mathbf{C}} C_{\alpha\beta}^{-1}, \quad (2.21)$$

which means that $S_{\alpha\beta}^{-1} S_{\gamma\epsilon} = C_{\alpha\beta}^{-1} C_{\gamma\epsilon}$. Furthermore, by taking the derivative of (2.20) we see

$$\frac{\partial S_{\gamma\epsilon}}{\partial C_{\alpha\beta}} = \frac{1}{\sqrt[3]{\det \mathbf{C}}} \left(\delta_{\alpha\gamma} \delta_{\beta\epsilon} - \frac{1}{3} C_{\gamma\epsilon} C_{\alpha\beta}^{-1} \right). \quad (2.22)$$

For $I_3 = 1$ we restrict the arbitrary functionals F, G to those which depend on \mathbf{S} (and $\nabla\mathbf{S}$) only through their dependence on \mathbf{C} (and $\nabla\mathbf{C}$): $F[\rho, s, \mathbf{M}, \mathbf{S}]$ and $G[\rho, s, \mathbf{M}, \mathbf{S}]$. Hence we define the total time derivative of F through the sum of four inner products once again as

$$\frac{dF}{dt} = \left\langle \frac{\delta F}{\delta \rho}, \frac{\partial \rho}{\partial t} \right\rangle + \left\langle \frac{\delta F}{\delta s}, \frac{\partial s}{\partial t} \right\rangle + \left\langle \frac{\delta F}{\delta M_\alpha}, \frac{\partial M_\alpha}{\partial t} \right\rangle + \left\langle \frac{\delta F}{\delta S_{\alpha\beta}}, \frac{\partial S_{\alpha\beta}}{\partial t} \right\rangle. \quad (2.23)$$

The Volterra derivatives of the hydrodynamic variables ρ, s, \mathbf{M} are still unconstrained. To obtain an expression for the constrained Volterra derivative $\delta F/\delta\mathbf{S}$ we compute the partial time derivative of $I_3 = \det \mathbf{S} = 1$ which is

$$\frac{\partial I_3}{\partial t} = \frac{\partial I_3}{\partial S_{\alpha\beta}} \frac{\partial S_{\alpha\beta}}{\partial t} = S_{\alpha\beta}^{-1} \frac{\partial S_{\alpha\beta}}{\partial t} = 0, \quad (2.24)$$

where we adopted the chain rule of differentiation to obtain the first identity and we used the Boussinesq relation to obtain the second identity. Since both subjects of the fourth inner product in Eq. (2.23) must belong to the same operating space, and therefore due to the above Eq. (2.24), we require

$$S_{\alpha\beta}^{-1} \frac{\delta F}{\delta S_{\alpha\beta}} = 0. \quad (2.25)$$

Hence we define the Volterra derivative $\delta F/\delta\mathbf{S}$ through the relationship

$$\frac{\delta F}{\delta S_{\alpha\beta}} = \frac{\partial f}{\partial S_{\alpha\beta}} - \frac{1}{3} \frac{\partial f}{\partial S_{\gamma\epsilon}} S_{\gamma\epsilon}^{-1} S_{\alpha\beta} - \nabla_\eta \left(\frac{\partial f}{\partial (\nabla_\eta S_{\alpha\beta})} \right) + \frac{1}{3} \nabla_\eta \left(\frac{\partial f}{\partial (\nabla_\eta S_{\gamma\epsilon})} \right) S_{\gamma\epsilon}^{-1} S_{\alpha\beta}, \quad (2.26)$$

which is seen to satisfy the above requirement, Eq. (2.25). Disposing of the projection mapping Eq. (2.20) we can now inspect the Poisson and dissipation brackets.

Transformation of the Poisson Bracket

To transform the Poisson bracket (2.11) in terms of the contravariant tensor \mathbf{C} into its equivalent expression in terms of a second-rank tensor, \mathbf{S} , with $I_3 = 1$, it suffices to inspect the $\{\cdot, \cdot\}_E^C = I1 + I2 + I3$ sub-bracket in (2.11) and to adopt the projection mapping, P_S as defined in Eq. (2.22). The derivation of the Poisson bracket in terms of \mathbf{S} is explained next.

To perform the transformation of the $\{\cdot, \cdot\}_E^C$ sub-bracket in (2.11) the Volterra derivative $\delta F/\delta\mathbf{C}$ has to be written in terms of $\delta F/\delta\mathbf{S}$, once again

$$\frac{\delta F}{\delta C_{\alpha\beta}} = \frac{\delta F}{\delta S_{\gamma\epsilon}} \frac{\partial S_{\alpha\beta}}{\partial C_{\gamma\epsilon}} = \frac{\delta F}{\delta S_{\gamma\epsilon}} \frac{1}{\sqrt[3]{\det \mathbf{C}}} \left(\delta_{\alpha\gamma} \delta_{\beta\epsilon} - \frac{1}{3} C_{\alpha\beta}^{-1} C_{\gamma\epsilon} \right), \quad (2.27)$$

where we have used Eq. (2.22). Next, the above relationship is inserted into the Poisson and dissipation sub-brackets. The mathematical manipulations to obtain the new brackets are described in what follows.

Inserting the relationship for the Volterra derivative (2.27) into integral I2 and adopting the definition (2.20) for \mathbf{S} we obtain

$$\begin{aligned} \text{I2} \equiv & - \int_{\Omega'} S_{\gamma\alpha} \left[\frac{\delta G}{\delta S_{\alpha\beta}} \nabla_\gamma \frac{\delta F}{\delta M_\beta} - \frac{\delta F}{\delta S_{\alpha\beta}} \nabla_\gamma \frac{\delta G}{\delta M_\beta} \right] d^3x \\ & + \frac{1}{3} \int_{\Omega'} S_{\rho\eta} \left[\frac{\delta G}{\delta S_{\rho\eta}} \nabla_\gamma \frac{\delta F}{\delta M_\gamma} - \frac{\delta F}{\delta S_{\rho\eta}} \nabla_\gamma \frac{\delta G}{\delta M_\gamma} \right] d^3x, \end{aligned} \quad (2.28)$$

likewise, integral I3 becomes

$$\begin{aligned} \text{I3} \equiv & - \int_{\Omega'} S_{\gamma\beta} \left[\frac{\delta G}{\delta S_{\alpha\beta}} \nabla_\gamma \frac{\delta F}{\delta M_\alpha} - \frac{\delta F}{\delta S_{\alpha\beta}} \nabla_\gamma \frac{\delta G}{\delta M_\alpha} \right] d^3x \\ & + \frac{1}{3} \int_{\Omega'} S_{\rho\eta} \left[\frac{\delta G}{\delta S_{\rho\eta}} \nabla_\gamma \frac{\delta F}{\delta M_\gamma} - \frac{\delta F}{\delta S_{\rho\eta}} \nabla_\gamma \frac{\delta F}{\delta M_\gamma} \right] d^3x. \end{aligned} \quad (2.29)$$

For integral I1 in Eq. (2.11) we have to perform more involved manipulations due to the appearance of the $\nabla_\gamma(\delta F/\delta M_\gamma C_{\alpha\beta})$ terms. Inserting the expression for the Volterra derivative (2.27) into I1 of Eq. (2.11) we get

$$\begin{aligned} \text{I1} \equiv & - \int_{\Omega'} \frac{1}{\sqrt[3]{\det \mathbf{C}}} \left[\frac{\delta F}{\delta S_{\alpha\beta}} \nabla_\gamma \left(\frac{\delta G}{\delta M_\gamma} C_{\alpha\beta} \right) - \frac{\delta G}{\delta S_{\alpha\beta}} \nabla_\gamma \left(\frac{\delta F}{\delta M_\gamma} C_{\alpha\beta} \right) \right] d^3x \quad \boxed{\text{A}} \\ & + \frac{1}{3} \int_{\Omega'} \frac{1}{\sqrt[3]{\det \mathbf{C}}} \left[\frac{\delta F}{\delta S_{\rho\eta}} C_{\rho\eta} C_{\alpha\beta}^{-1} \nabla_\gamma \left(\frac{\delta G}{\delta M_\gamma} C_{\alpha\beta} \right) - \frac{\delta G}{\delta S_{\rho\eta}} C_{\rho\eta} C_{\alpha\beta}^{-1} \nabla_\gamma \left(\frac{\delta F}{\delta M_\gamma} C_{\alpha\beta} \right) \right] d^3x. \end{aligned} \quad \boxed{\text{B}}$$

Next, we inspect integral A to which we apply the product rule of differentiation

$$\text{A} \equiv - \int_{\Omega'} \left[\frac{\delta F}{\delta S_{\alpha\beta}} S_{\alpha\beta} \nabla_\gamma \left(\frac{\delta G}{\delta M_\gamma} \right) - \frac{\delta G}{\delta S_{\alpha\beta}} S_{\alpha\beta} \nabla_\gamma \left(\frac{\delta F}{\delta M_\gamma} \right) \right] d^3x \quad \boxed{\text{C}}$$

$$+ \int_{\Omega'} \left[\frac{\delta F}{\delta S_{\alpha\beta}} \frac{\delta G}{\delta M_\gamma} \frac{\nabla_\gamma C_{\alpha\beta}}{\sqrt[3]{\det \mathbf{C}}} - \frac{\delta G}{\delta S_{\alpha\beta}} \frac{\delta F}{\delta M_\gamma} \frac{\nabla_\gamma C_{\alpha\beta}}{\sqrt[3]{\det \mathbf{C}}} \right] d^3x. \quad \boxed{\text{D}}$$

Application of the product rule of differentiation and the projection (2.20) to integral D gives

$$\text{D} \equiv - \int_{\Omega'} \left[\frac{\delta F}{\delta S_{\alpha\beta}} \frac{\delta G}{\delta M_\gamma} \nabla_\gamma S_{\alpha\beta} - \frac{\delta G}{\delta S_{\alpha\beta}} \frac{\delta F}{\delta M_\gamma} \nabla_\gamma S_{\alpha\beta} \right] d^3x \quad \boxed{\text{E}}$$

$$+ \int_{\Omega'} \left[C_{\alpha\beta} \frac{\delta F}{\delta S_{\alpha\beta}} \frac{\delta G}{\delta M_\gamma} \nabla_\gamma \left(\frac{1}{\sqrt[3]{\det \mathbf{C}}} \right) - C_{\alpha\beta} \frac{\delta G}{\delta S_{\alpha\beta}} \frac{\delta F}{\delta M_\gamma} \nabla_\gamma \left(\frac{1}{\sqrt[3]{\det \mathbf{C}}} \right) \right] d^3x. \quad \boxed{\text{F}}$$

Next we turn to integral B which we rewrite

$$\begin{aligned} \text{B} \equiv & \int_{\Omega'} \frac{1}{\sqrt[3]{\det \mathbf{C}}} \left[\frac{\delta F}{\delta S_{\rho\eta}} C_{\rho\eta} \nabla_\gamma \frac{\delta G}{\delta M_\gamma} - \frac{\delta G}{\delta S_{\rho\eta}} C_{\rho\eta} \nabla_\gamma \frac{\delta F}{\delta M_\gamma} \right] d^3x \\ & + \frac{1}{3} \int_{\Omega'} \frac{1}{\sqrt[3]{\det \mathbf{C}}} \left[\frac{\delta F}{\delta S_{\rho\eta}} C_{\rho\eta} \frac{\delta H}{\delta M_\gamma} C_{\alpha\beta}^{-1} \nabla_\gamma C_{\alpha\beta} - \frac{\delta H}{\delta S_{\rho\eta}} C_{\rho\eta} \frac{\delta F}{\delta M_\gamma} C_{\alpha\beta}^{-1} \nabla_\gamma C_{\alpha\beta} \right] d^3x. \end{aligned}$$

Now we take $\text{II} = \text{B} + \text{C} + \text{E} + \text{F}$ and we get

$$\text{II} \equiv \int_{\Omega'} \left[\frac{\delta F}{\delta S_{\alpha\beta}} \frac{\delta G}{\delta M_\gamma} \nabla_\gamma S_{\alpha\beta} - \frac{\delta G}{\delta S_{\alpha\beta}} \frac{\delta F}{\delta M_\gamma} \nabla_\gamma S_{\alpha\beta} \right] d^3x, \quad (2.30)$$

since B cancels with C and F and we have applied the relationship

$$\nabla_\gamma \frac{1}{\sqrt[3]{\det \mathbf{C}}} = -\frac{1}{3\sqrt[3]{\det \mathbf{C}}} C_{\rho\eta}^{-1} \nabla_\gamma C_{\rho\eta},$$

to integral F. The desired sub-bracket for the constraint $I_3 = 1$ is given as the sum of $\text{II} + \text{I2} + \text{I3}$ from Eqs. (2.30), (2.28), (2.29).

$$\begin{aligned} \{F, G\}_E^S = & - \int_{\Omega'} \left[\frac{\delta F}{\delta S_{\alpha\beta}} \frac{\delta G}{\delta M_\gamma} \nabla_\gamma (S_{\alpha\beta}) - \frac{\delta G}{\delta S_{\alpha\beta}} \frac{\delta F}{\delta M_\gamma} \nabla_\gamma (S_{\alpha\beta}) \right] d^3x \\ & - \int_{\Omega'} S_{\gamma\alpha} \left[\frac{\delta G}{\delta S_{\alpha\beta}} \nabla_\gamma \left(\frac{\delta F}{\delta M_\beta} \right) - \frac{\delta F}{\delta S_{\alpha\beta}} \nabla_\gamma \left(\frac{\delta G}{\delta M_\beta} \right) \right] d^3x \\ & - \int_{\Omega'} S_{\gamma\beta} \left[\frac{\delta G}{\delta S_{\alpha\beta}} \nabla_\gamma \left(\frac{\delta F}{\delta M_\alpha} \right) - \frac{\delta F}{\delta S_{\alpha\beta}} \nabla_\gamma \left(\frac{\delta G}{\delta M_\alpha} \right) \right] d^3x \\ & + \frac{2}{3} \int_{\Omega'} S_{\alpha\beta} \left[\frac{\delta G}{\delta S_{\alpha\beta}} \nabla_\gamma \left(\frac{\delta F}{\delta M_\gamma} \right) - \frac{\delta F}{\delta S_{\alpha\beta}} \nabla_\gamma \left(\frac{\delta G}{\delta M_\gamma} \right) \right] d^3x. \end{aligned} \quad (2.31)$$

This bracket is bilinear, antisymmetric, and it satisfies the Jacobi identity since it has been obtained from a transformation of the unconstrained bracket (2.11) using the relationship of Eq. (2.27). It has been derived originally in Edwards et al. (2003). We have thus found a Poisson bracket that allows to describe the dynamics of a fluid with a volume preserving microstructure. We proceed to perform similar manipulations with the dissipation bracket.

Transformation of the Dissipation Bracket

Inserting (2.27) into the sub-bracket $[\cdot, \cdot]_E^C$ of Eq. (2.13) and rearranging the terms we obtain

$$\begin{aligned}
 [F, G]_E^S &= - \int_{\Omega'} \left\{ R_{\alpha\beta\gamma\epsilon\eta\nu}^* \nabla_\alpha \frac{\delta F}{\delta S_{\beta\gamma}} \nabla_\epsilon \frac{\delta G}{\delta S_{\eta\nu}} \right. \\
 &\quad \left. - \frac{1}{3} R_{\alpha\beta\gamma\epsilon\eta\nu}^* \nabla_\alpha \left(\frac{\delta F}{\delta S_{\rho\theta}} S_{\rho\theta} S_{\beta\gamma}^{-1} \right) \nabla_\epsilon \left(\frac{\delta G}{\delta S_{\eta\nu}} \right) \right\} d^3x \\
 &\quad - \int_{\Omega'} \left[\Lambda_{\alpha\beta\gamma\epsilon}^* \frac{\delta F}{\delta S_{\alpha\beta}} \frac{\delta G}{\delta S_{\gamma\epsilon}} - \frac{1}{3} \Lambda_{\alpha\beta\gamma\epsilon}^* S_{\alpha\beta}^{-1} \frac{\delta F}{\delta S_{\eta\xi}} S_{\eta\xi} \frac{\delta G}{\delta S_{\gamma\epsilon}} \right] d^3x \\
 &\quad - \int_{\Omega'} \left[P_{\alpha\beta\gamma\epsilon}^* \left(\nabla_\alpha \frac{\delta F}{\delta M_\beta} \frac{\delta G}{\delta S_{\gamma\epsilon}} - \nabla_\alpha \frac{\delta G}{\delta M_\beta} \frac{\delta F}{\delta S_{\gamma\epsilon}} \right) \right. \\
 &\quad \left. - \frac{1}{3} P_{\alpha\beta\gamma\epsilon}^* \left(\nabla_\alpha \frac{\delta F}{\delta M_\beta} \frac{\delta G}{\delta S_{\rho\theta}} S_{\rho\theta} S_{\gamma\epsilon}^{-1} - \nabla_\alpha \frac{\delta G}{\delta M_\beta} \frac{\delta F}{\delta S_{\rho\theta}} S_{\rho\theta} S_{\gamma\epsilon}^{-1} \right) \right] d^3x \\
 &\quad + \text{additional terms involving } \frac{1}{T} \frac{\delta F}{\delta S},
 \end{aligned} \tag{2.32}$$

where $\Lambda^* = \Lambda / \sqrt[3]{(\det \mathbf{C})^2}$, $\mathbf{P}^* = \mathbf{P} / \sqrt[3]{(\det \mathbf{C})}$, and $\mathbf{R}^* = \mathbf{R} / \sqrt[3]{(\det \mathbf{C})^2}$ are arbitrary functions of the structural variable, \mathbf{S} , and the phenomenological matrices satisfy appropriate symmetry relationships. Let us now use the two brackets together with the Hamiltonian to obtain a set of flow equations for the fluid with a volume preserving microstructure.

Time Evolution Equations

Taking Eq. (2.1) together with the constrained Poisson and dissipation sub-brackets (2.31), (2.32) we obtain the time evolution equation of the volume preserving internal variable after the arbitrary functional G has been replaced with the Hamiltonian (2.14)

$$\begin{aligned}
 \frac{\partial S_{\alpha\beta}}{\partial t} &= -v_\gamma \nabla_\gamma S_{\alpha\beta} + S_{\gamma\alpha} \nabla_\gamma v_\beta + S_{\gamma\beta} \nabla_\gamma v_\alpha - \frac{2}{3} S_{\alpha\beta} \nabla_\gamma v_\gamma + P_{\gamma\epsilon\alpha\beta}^* \nabla_\gamma \frac{\delta H}{\delta M_\epsilon} \\
 &\quad - \frac{1}{3} P_{\rho\theta\eta\xi}^* \nabla_\rho \frac{\delta H}{\delta M_\theta} S_{\alpha\beta} S_{\eta\xi}^{-1} - \Lambda_{\alpha\beta\gamma\epsilon}^* \frac{\delta H}{\delta S_{\gamma\epsilon}} + \frac{1}{3} \Lambda_{\eta\xi\gamma\epsilon}^* S_{\eta\xi}^{-1} \frac{\delta H}{\delta S_{\gamma\epsilon}} S_{\alpha\beta} \\
 &\quad + \nabla_\gamma \left(R_{\gamma\alpha\beta\epsilon\eta\nu}^* \nabla_\epsilon \frac{\delta H}{\delta S_{\eta\nu}} \right) - \frac{1}{3} \nabla_\rho \left[R_{\rho\delta\gamma\epsilon\eta\nu}^* \nabla_\epsilon \left(\frac{\delta H}{\delta S_{\eta\nu}} \right) \right] S_{\delta\gamma}^{-1} S_{\alpha\beta}.
 \end{aligned} \tag{2.33}$$

Multiplication of the above Eq. (2.33) with $S_{\alpha\beta}^{-1}$ shows that the dynamical equation satisfies the requirement (2.24). This means that \mathbf{S} is volume preserving. We have

derived a thermodynamically consistent set of time evolution equations for our set of constrained variables. The structure of the balance equations for the mass density, the entropy density, and the momentum density remains unaltered. These are given by Eqs (2.16a)-(2.16c).

The set of time evolution equations (2.16a)-(2.16c) and (2.33) is the most general one for describing the dynamics of complex material with a volume preserving microstructure from a continuum level of description. Also this set of continuum equations accounts for compressibility, it is fully non-isothermal, and it allows for elastic and viscous stresses. Now, the extra stress in the momentum equation (2.16c) reads

$$\begin{aligned} \sigma_{\alpha\beta} = & 2S_{\beta\gamma} \frac{\delta H}{\delta S_{\gamma\alpha}} - \frac{1}{3} S_{\beta\gamma} \frac{\delta H}{\delta S_{\rho\theta}} S_{\rho\theta}^{-1} S_{\alpha\gamma} + Q_{\alpha\beta\gamma\epsilon}^* \nabla_{\gamma} v_{\epsilon} + P_{\alpha\beta\gamma\epsilon}^* \frac{\delta H}{\delta S_{\gamma\epsilon}} \\ & - \frac{1}{3} P_{\alpha\beta\gamma\epsilon}^* \frac{\delta H}{\delta S_{\rho\theta}} S_{\rho\theta} S_{\gamma\epsilon}^{-1}, \end{aligned} \quad (2.34)$$

where $\mathbf{Q}^* = \mathbf{Q}$ and we have to adopt Eq. (2.26) for the constrained Volterra derivative. The pressure in the momentum equation arises naturally through the Poisson bracket and it is given by the expression

$$p = -u + \rho \left. \frac{\partial u}{\partial \rho} \right|_{s, \mathbf{S}} + s \left. \frac{\partial u}{\partial s} \right|_{\rho, \mathbf{S}} + \frac{2}{3} S_{\alpha\beta} \left. \frac{\partial u}{\partial S_{\alpha\beta}} \right|_{\rho, s}, \quad (2.35)$$

which has an additional extra term over the usual thermodynamic expression for the pressure, Eq. (2.18). If one wishes to apply the set of balance equations (2.16a)-(2.16c), (2.33) a further thermodynamic transformation should be defined in order to work with the usual definition of the pressure. The rate of entropy production per unit volume in the system is now

$$\begin{aligned} \Sigma = & \frac{1}{T} \nabla_{\alpha} (B_{\alpha\beta}^* T \nabla_{\beta} T) + \frac{1}{T} Q_{\alpha\beta\gamma\epsilon}^* \nabla_{\alpha} v_{\beta} \nabla_{\gamma} v_{\epsilon} + \frac{1}{T} R_{\alpha\beta\gamma\epsilon\eta\nu}^* \nabla_{\alpha} \left(\frac{\delta H}{\delta S_{\beta\gamma}} \right) \nabla_{\epsilon} \left(\frac{\delta H}{\delta S_{\eta\nu}} \right) \\ & - \frac{1}{3T} R_{\alpha\beta\gamma\epsilon\eta\nu}^* \nabla_{\alpha} \left(\frac{\delta H}{\delta S_{\rho\theta}} S_{\rho\theta} S_{\beta\gamma}^{-1} \right) \nabla_{\epsilon} \left(\frac{\delta H}{\delta S_{\eta\nu}} \right) + \frac{1}{T} \Lambda_{\alpha\beta\gamma\epsilon}^* \frac{\delta H}{\delta S_{\alpha\beta}} \frac{\delta H}{\delta S_{\gamma\epsilon}} \\ & - \frac{1}{3T} \Lambda_{\alpha\beta\gamma\epsilon}^* S_{\alpha\beta}^{-1} \frac{\delta H}{\delta S_{\eta\zeta}} S_{\eta\zeta} \frac{\delta H}{\delta S_{\gamma\epsilon}}, \end{aligned} \quad (2.36)$$

where $\mathbf{B}^* = \mathbf{B}$.

In order to develop a useful theory it is necessary to supply a microstructural interpretation of the constrained structural variable, \mathbf{S} , to determine a suitable thermodynamic potential for the Hamiltonian, H , and to specify constitutive assumptions for the phenomenological matrices, \mathbf{B} , \mathbf{Q} , $\mathbf{\Lambda}$, \mathbf{P} , \mathbf{R} . This is topic of the following chapter.

3. Modeling

From the formal presentation of the dynamics of fluids in the last chapter we proceed to model highly viscous emulsions with main emphasis on the matrix-droplet interaction. In the specific treatment of emulsions with matrix viscoelasticity given below, we shall assume that break-up and coalescence do not occur. Later, we will relax this assumption to derive a model taking into account these phenomena. The main emphasis will be on how to derive flow equations for emulsions and how to assess their thermodynamic consistency, *i. e.* to ensure the models always respect the Laws of Thermodynamics.

3.1. Matrix Viscoelasticity

We model a highly viscous emulsion with droplet morphology which consists of a viscoelastic matrix phase and an incompressible Newtonian droplet phase. The emulsion is described as a thermodynamic system of two immiscible phases. We assume that the dispersed phase concentration and the material properties of the blend components are such that breakup and coalescence do not occur in equilibrium and under flow, being a reasonable approximation in appropriate deformation and strain rate regimes. Since the matrix fluid is viscoelastic we expect large normal stresses in the deforming emulsion. These normal stresses influence the deformation of the micro-droplets. Therefore, we develop a model which accounts for the influence of matrix deformation on the droplet shape. The coupling of matrix with droplet deformation is described phenomenologically.

3.1.1. System Variables

The physical variables for the description of the emulsion are the momentum density, $\mathbf{M} = \rho \mathbf{v}$, the unconstrained contravariant second-rank tensor, \mathbf{C} , describing the conformation of the polymer molecules in the matrix, and the constrained contravariant second-rank tensor, \mathbf{S} , to describe ellipsoidal droplet shapes: hence $x = [\mathbf{M}, \mathbf{C}, \mathbf{S}]$. Since

the disperse phase is assumed to be incompressible, we impose the microstructural constraint, $\det \mathbf{S} = 1$, to account for volume preservation of the deforming micro-droplets. Further droplet configuration tensors or conformation tensors may be included into the above set of variables to describe systems with non-uniform droplet size distribution or rheologically more complex matrix fluids, if desired (Yu et al., 2005).

3.1.2. Poisson and Dissipation Bracket

We can simply use the results of Chap. 2 to write down the Poisson bracket for the medium that is described in terms of $x = [\mathbf{M}, \mathbf{C}, \mathbf{S}]$. The Poisson brackets in terms of $x = [\mathbf{M}, \mathbf{C}]$ and $x = [\mathbf{M}, \mathbf{S}]$ are given by the last four integrals of Eq. (2.11) and the third integral of Eq. (2.11) together with Eq. (2.31), respectively. Consequently, the Poisson bracket expressed in terms of \mathbf{M} , \mathbf{C} , and \mathbf{S} reads

$$\begin{aligned}
 \{F, H_m\} = & - \int \left[\frac{\delta F}{\delta M_\gamma} \nabla_\beta \left(\frac{\delta H_m}{\delta M_\beta} M_\gamma \right) - \frac{\delta H_m}{\delta M_\gamma} \nabla_\beta \left(\frac{\delta F}{\delta M_\beta} M_\gamma \right) \right] d^3x \\
 & - \int \left[\frac{\delta F}{\delta C_{\alpha\beta}} \nabla_\gamma \left(\frac{\delta H_m}{\delta M_\gamma} C_{\alpha\beta} \right) - \frac{\delta H_m}{\delta C_{\alpha\beta}} \nabla_\gamma \left(\frac{\delta F}{\delta M_\gamma} C_{\alpha\beta} \right) \right] d^3x \\
 & - \int C_{\gamma\alpha} \left[\frac{\delta H_m}{\delta C_{\alpha\beta}} \nabla_\gamma \left(\frac{\delta F}{\delta M_\beta} \right) - \frac{\delta F}{\delta C_{\alpha\beta}} \nabla_\gamma \left(\frac{\delta H_m}{\delta M_\beta} \right) \right] d^3x \\
 & - \int C_{\gamma\beta} \left[\frac{\delta H_m}{\delta C_{\alpha\beta}} \nabla_\gamma \left(\frac{\delta F}{\delta M_\alpha} \right) - \frac{\delta F}{\delta C_{\alpha\beta}} \nabla_\gamma \left(\frac{\delta H_m}{\delta M_\alpha} \right) \right] d^3x \\
 & - \int \left[\frac{\delta F}{\delta S_{\alpha\beta}} \frac{\delta H_m}{\delta M_\gamma} \nabla_\gamma (S_{\alpha\beta}) - \frac{\delta H_m}{\delta S_{\alpha\beta}} \frac{\delta F}{\delta M_\gamma} \nabla_\gamma (S_{\alpha\beta}) \right] d^3x \\
 & - \int S_{\gamma\alpha} \left[\frac{\delta H_m}{\delta S_{\alpha\beta}} \nabla_\gamma \left(\frac{\delta F}{\delta M_\beta} \right) - \frac{\delta F}{\delta S_{\alpha\beta}} \nabla_\gamma \left(\frac{\delta H_m}{\delta M_\beta} \right) \right] d^3x \\
 & - \int S_{\gamma\beta} \left[\frac{\delta H_m}{\delta S_{\alpha\beta}} \nabla_\gamma \left(\frac{\delta F}{\delta M_\alpha} \right) - \frac{\delta F}{\delta S_{\alpha\beta}} \nabla_\gamma \left(\frac{\delta H_m}{\delta M_\alpha} \right) \right] d^3x \\
 & + \frac{2}{3} \int S_{\alpha\beta} \left[\frac{\delta H_m}{\delta S_{\alpha\beta}} \nabla_\gamma \left(\frac{\delta F}{\delta M_\gamma} \right) - \frac{\delta F}{\delta S_{\alpha\beta}} \nabla_\gamma \left(\frac{\delta H_m}{\delta M_\gamma} \right) \right] d^3x.
 \end{aligned} \tag{3.1}$$

This bracket shares all properties of a Poisson bracket.

For the dissipation bracket, we adopt the following expression:

$$\begin{aligned}
 [F, H] = & - \int \Lambda_{\alpha\beta\gamma\epsilon}^{\text{C}} \frac{\delta F}{\delta C_{\alpha\beta}} \frac{\delta H}{\delta C_{\gamma\epsilon}} d^3x \\
 & - \int \Lambda_{\alpha\beta\gamma\epsilon}^{\text{S}} \frac{\delta F}{\delta S_{\alpha\beta}} \frac{\delta H}{\delta S_{\gamma\epsilon}} d^3x \\
 & + \frac{1}{3} \int \Lambda_{\alpha\beta\gamma\epsilon}^{\text{S}} S_{\rho\eta} S_{\alpha\beta}^{-1} \frac{\delta F}{\delta S_{\rho\eta}} \frac{\delta H}{\delta S_{\gamma\epsilon}} d^3x \\
 & - \int A_{\alpha\beta\gamma\epsilon} \left(\frac{\delta F}{\delta C_{\alpha\beta}} \frac{\delta H}{\delta S_{\gamma\epsilon}} + \frac{\delta H}{\delta C_{\alpha\beta}} \frac{\delta F}{\delta S_{\gamma\epsilon}} \right) d^3x \\
 & + \frac{1}{3} \int A_{\alpha\beta\gamma\epsilon} \left(\frac{\delta F}{\delta C_{\alpha\beta}} \frac{\delta H}{\delta S_{\rho\eta}} S_{\rho\eta} S_{\gamma\epsilon}^{-1} + \frac{\delta H}{\delta C_{\alpha\beta}} \frac{\delta F}{\delta S_{\rho\eta}} S_{\rho\eta} S_{\gamma\epsilon}^{-1} \right) d^3x,
 \end{aligned} \tag{3.2}$$

with the three phenomenological matrices Λ^{C} , Λ^{S} , and \mathbf{A} . The first integral in the above dissipation bracket is the relaxation of the viscoelastic matrix, Eq. (2.12). The second and the third integral account for the relaxation of the droplet inclusions under the auspices of the constraint $\det \mathbf{S} = 1$, Eq. (2.32) derived in Edwards et al. (2003). The most strikingly feature of the dissipation bracket (3.2) are the integrals with the phenomenological matrix \mathbf{A} . These two integrals describe the coupling of the viscoelastic matrix fluid with the droplet interface and they have been derived with the procedure presented in Sec. 2.4.2. In the above dissipation bracket, we neglect viscous dissipation of the matrix fluid since it appears implicitly in the Maxwell viscosity related to the phenomenological matrix Λ^{C} . Let us in the next paragraph consider the dynamical equations obtained from the above brackets.

3.1.3. General Flow Equations

The Poisson and dissipation brackets yield the following general set of dynamical evolution equations, where $u \equiv u(\mathbf{S}, \mathbf{C})$ in the Hamiltonian (2.14)

$$\rho \frac{\partial v_\alpha}{\partial t} = -\rho v_\beta \nabla_\beta v_\alpha - \nabla_\alpha p + \nabla_\beta \sigma_{\alpha\beta}, \tag{3.3a}$$

$$\begin{aligned}
 \frac{\partial C_{\alpha\beta}}{\partial t} = & -v_\gamma \nabla_\gamma C_{\alpha\beta} + C_{\alpha\gamma} \nabla_\gamma v_\beta + C_{\beta\gamma} \nabla_\gamma v_\alpha - \Lambda_{\alpha\beta\gamma\epsilon}^{\text{C}} \frac{\delta H_{\text{m}}}{\delta C_{\gamma\epsilon}} - A_{\alpha\beta\gamma\epsilon} \frac{\delta H_{\text{m}}}{\delta S_{\gamma\epsilon}} \\
 & + \frac{1}{3} A_{\alpha\beta\gamma\epsilon} \frac{\delta H_{\text{m}}}{\delta S_{\rho\nu}} S_{\rho\nu} S_{\gamma\epsilon}^{-1},
 \end{aligned} \tag{3.3b}$$

$$\begin{aligned}
 \frac{\partial S_{\alpha\beta}}{\partial t} = & -v_\gamma \nabla_\gamma S_{\alpha\beta} - \frac{2}{3} \nabla_\gamma v_\gamma S_{\alpha\beta} + S_{\alpha\gamma} \nabla_\gamma v_\beta + S_{\beta\gamma} \nabla_\gamma v_\alpha - \Lambda_{\alpha\beta\gamma\epsilon}^{\text{S}} \frac{\delta H_{\text{m}}}{\delta S_{\gamma\epsilon}} \\
 & + \frac{1}{3} \Lambda_{\rho\eta\gamma\epsilon}^{\text{S}} S_{\alpha\beta} S_{\rho\eta}^{-1} \frac{\delta H_{\text{m}}}{\delta S_{\gamma\epsilon}} - A_{\alpha\beta\gamma\epsilon} \frac{\delta H_{\text{m}}}{\delta C_{\gamma\epsilon}} + \frac{1}{3} A_{\rho\nu\gamma\epsilon} \frac{\delta H_{\text{m}}}{\delta C_{\rho\nu}} S_{\gamma\epsilon}^{-1} S_{\alpha\beta}.
 \end{aligned} \tag{3.3c}$$

3. Modeling

Equation (3.3a) is the momentum balance equation in a spatial description of macroscopic fluid flow, where the pressure and the extra stress tensor have been denoted with p , $\boldsymbol{\sigma}$, respectively. As already mentioned, pressure and velocity are viewed as averaged quantities at each location in space-time coordinates; *i. e.*, they are coarse-grained averages of the matrix fluid particles and droplets contained in the fluid particle at coordinates (\mathbf{x}, t) . They arise naturally through the mathematical structure of the Poisson bracket. The pressure obeys a Poisson equation with appropriate boundary conditions, and the extra stress tensor is obtained as

$$\sigma_{\alpha\beta} = 2C_{\alpha\gamma} \frac{\delta H_m}{\delta C_{\gamma\beta}} + 2S_{\alpha\gamma} \frac{\delta H_m}{\delta S_{\gamma\beta}} - \frac{2}{3} S_{\gamma\epsilon} \frac{\delta H_m}{\delta S_{\gamma\epsilon}} \delta_{\alpha\beta}, \quad (3.3d)$$

where the first term accounts for matrix phase elasticity and the remaining two terms for interfacial elasticity, respectively. The two contributions are different since the droplet shape tensor is volume preserving.

Equation (3.3b) is the conformation tensor equation describing the average deformation and orientation of polymer molecules in the matrix. The first three terms on the right hand-side of Eq. (3.3b) represent the upper-convected derivative of the unconstrained, second-rank contravariant tensorial variable, and they arise from the mathematical structure of the Poisson bracket, Eq. (3.1). The remaining three terms on the right hand-side of Eq. (3.3b) are of dissipative nature and they arise from the dissipation bracket (3.13). The third term captures the relaxational dynamics of the matrix molecules and the last two terms in Eq. (3.3b) account for the influence of droplet deformation on the conformation tensor dynamics.

Equation (3.3c) is the droplet shape tensor equation describing the average shape and orientation of micro-droplets in the emulsion. The first four terms on the right hand-side of Eq. (3.3c) represent a generalized upper-convected derivative for a second-rank, contravariant tensorial variable with the constraint $\det \mathbf{S} = 1$, obtained from the Poisson bracket (3.1). The last four terms in Eq. (3.3c) arise from the dissipation bracket (3.13), and account for the relaxation of micro-droplets (fifth and sixth terms) and the influence of the conformation tensor dynamics on the droplet dynamics (the last two terms). With the procedure presented in Chap. 2 (*cf.* Edwards et al., 2003), it can be shown for Eqs. (3.3b) and (3.3c) that $\det \mathbf{S}$ is a conserved quantity independent of the mathematical form of the phenomenological matrices $\boldsymbol{\Lambda}^C$, $\boldsymbol{\Lambda}^S$, \mathbf{A} , and the Hamiltonian, $H_m[\mathbf{M}, \mathbf{C}, \mathbf{S}]$.

In order to obtain a specific set of system equations from the set of Eqs. (3.3), we have to find expressions for the Hamiltonian and the phenomenological matrices appearing in the dissipation bracket, Eq. (3.2). These are the four ingredients required to reduce the set of general time evolution equations (3.3) to a specific model for the emulsion. We continue to specify the most simple relationships for the system Hamiltonian and the phenomenological matrices, *i. e.* we will reduce the general set of equations (3.3) to a specific emulsion model.

3.1.4. System Hamiltonian

Let us suppose that the emulsion can be envisioned as a Maxwell fluid with characteristic elastic constant, K , coupling non-linearly to an elastic interface with interfacial tension, Γ' . One particular realization of such a system can be described in terms of the Hamiltonian

$$H_m[\mathbf{M}, \mathbf{C}, \mathbf{S}] = K[\mathbf{M}] + A[\mathbf{C}, \mathbf{S}] = \int \left[\frac{M_\alpha M_\alpha}{2\rho} + \frac{1}{2} n_C K (1 - \phi) \text{tr} \mathbf{C} - \frac{1}{2} n_C k_B T (1 - \phi) \ln(\det \mathbf{C}) + \frac{1}{2} \Gamma \phi I_2^S \right] d^3x, \quad (3.4)$$

where I_2^S is the second invariant of \mathbf{S} , ϕ is the concentration of droplets, n_C is the degree of elasticity per unit volume of the matrix, and $\Gamma = \Gamma'/R$ where R is the average droplet radius in the undeformed state. Eq. (3.4) represents the kinetic energy of the system (first term in the integral) plus a linear superposition of the elastic free energy of an ensemble of Hookean springs (second and third terms) and the energy of the elastic interface, with I_2^S being associated with the droplet surface area (fourth term). The subscript “m” in the Hamiltonian denotes that the description of the polymer blend is purely mechanical, *i.e.*, we have not considered a balance equation for the entropy density to account for the transfer of mechanical energy into internal degrees of freedom. Note that the last term in the integral of Eq. (3.4) is different from the expression for the thermodynamic potential introduced in Grmela et al. (2001). A physical justification for the choice for this term is that the specific surface energy is proportional to the surface area (at least for small deviations from sphericity) and it assumes a minimum for the spherical droplet.

3.1.5. Phenomenological Matrices

Let us continue with the specification of the dissipative phenomenological coefficients appearing in the bracket of Eq. (3.2). We adopt the phenomenological matrix for the Maxwell Model to describe the relaxation of the matrix fluid (Beris and Edwards, 1994)

$$\Lambda_{\alpha\beta\gamma\epsilon}^C = \frac{1}{2G\lambda_C} \frac{k_B T}{K} (C_{\alpha\gamma} \delta_{\beta\epsilon} + C_{\alpha\epsilon} \delta_{\beta\gamma} + C_{\beta\gamma} \delta_{\alpha\epsilon} + C_{\beta\epsilon} \delta_{\alpha\gamma}), \quad (3.5a)$$

where λ_C is a characteristic relaxation time associated with the continuous phase and we have introduced the elastic modulus of the continuous phase $G = n_C k_B T$. In conjunction with the \mathbf{C} -terms in the above Hamiltonian, Eq. (3.4), and with $\mathbf{A} = 0$, this expression gives the Upper-Convected Maxwell Model (UCMM) for the matrix phase.

For the relaxation matrix of the interface we adopt the following expression

$$\Lambda_{\alpha\beta\gamma\epsilon}^S = \frac{1}{\Gamma\lambda_S} \left[\frac{(1+p^*)^2 p^*}{2} (S_{\alpha\gamma}\delta_{\beta\epsilon} + S_{\alpha\epsilon}\delta_{\beta\gamma} + S_{\beta\gamma}\delta_{\alpha\epsilon} + S_{\beta\epsilon}\delta_{\alpha\gamma}) + \frac{3p^*}{I_1^S I_2^S} (\delta_{\alpha\gamma}\delta_{\beta\epsilon} + \delta_{\alpha\epsilon}\delta_{\beta\gamma}) \right], \quad (3.5b)$$

where λ_S is a characteristic time scale associated with the elastic interface and I_1^S, I_2^S are the first and the second invariant of \mathbf{S} , respectively. The quantity p^* is a phenomenological parameter that controls whether the droplet deformation is more oblate or prolate, and it depends on the viscous and/or elastic properties of the two phases. The first term in the square brackets accounts for droplets which deform into oblates for startup of steady shearing flow, the second term accounts for droplets which deform into prolates for startup of steady shearing flow. The difference between oblate and prolate droplet shapes is illustrated in the figures of Chap. 4, Sec. 4.1.

The phenomenological matrix \mathbf{A} is adopted in analogy with the coupling matrix introduced in Beris and Edwards (1994); Dressler and Edwards (2004); Edwards et al. (1996)

$$A_{\alpha\beta\gamma\epsilon} = \frac{1}{2} \frac{(1+p^*)^2 \theta}{\sqrt{G\Gamma\lambda_C\lambda_S}} (C_{\alpha\gamma}S_{\beta\epsilon} + C_{\alpha\epsilon}S_{\beta\gamma} + C_{\beta\gamma}S_{\alpha\epsilon} + C_{\beta\epsilon}S_{\alpha\gamma}), \quad (3.5c)$$

where θ is a phenomenological coupling parameter. The relaxation matrix (3.5c) is linear in the conformation tensor and in the droplet shape tensor and consequently it is the easiest way to quantify matrix-disperse phase coupling in highly viscous emulsions. For $\theta > 0$, the above phenomenological matrix gives oblate droplet configurations. Note that the coupling matrix vanishes for $p^* = -1$. The phenomenological coefficient θ may be taken as a function of the scalar invariants of the structural variables, if so desired; however, here we want to work with θ being a constant, real number for simplicity. Next we need to make some remarks concerning the scalar coefficients in the three phenomenological matrices and their determination from experiment.

To fit the model to experimental data it is necessary to incorporate the viscoelastic characteristics of the matrix phase into the relaxation matrix Λ_C . Here we use a variable relaxation time,

$$\lambda_c \equiv \lambda_c (1/3\text{tr}\tilde{\mathbf{C}})^k, \quad (3.6)$$

with $\tilde{\mathbf{C}} = \mathbf{C}K/k_B T$ and k being a power law index according to the Extended White-Metzner (EWM) Model (Souvaliotis and Beris, 1992). This allows to incorporate the effects of matrix shear thinning into the model. The inclusion of matrix viscoelasticity into the description is essential for fitting experimental data in App. A. In the development of the model equations we work in terms of the phenomenological coefficient of

the UCM Model to keep the equations as simple as possible. Equation (3.5c) has to be generalized in analogy to Eq. (3.5a) if the shear thinning behavior of the matrix phase is incorporated into the modeling, *i. e.* $\lambda_c \equiv \lambda_c(1/3\text{tr}\tilde{\mathbf{C}})^k$.

Note that the prefactors that contain the viscosity ratio in the phenomenological matrices, Eqs. (3.5b, 3.5c) have been introduced ad hoc: $\zeta_o = (1 + p^*)^2 p^*$, $\zeta_p = p^*$, $\zeta_c = (1 + p^*)^2$. It may be necessary to adopt more appropriate functional dependencies if one wants to fit experimental data or to make predictions over an extended range of viscosity ratios, p^* .

Since experiments show that the deformation behavior of viscous droplets in a continuous phase into prolates or oblates depends on the viscosity and the linear viscoelastic response of the phases (Guido and Villone, 1998; Levitt et al., 1996), the coefficient p^* should be related to the viscous properties of both phases. In principle, we can consider two possibilities to relate the phenomenological coefficient, p^* , to the material properties of the emulsion components.

If droplet deformation into oblate or prolate configurations is assumed to depend on the viscous properties of the two phases, then p^* should be taken as the negative viscosity ratio of the emulsion components¹

$$p^* = -\frac{\eta_d}{\eta_c}. \quad (3.7a)$$

For this choice of the coefficient p^* droplet deformation depends on the two dimensionless groups viscosity ratio of emulsion components and Deborah number. The Toy Model in Sec. 1.2 works with this definition of the coefficient p^* . It is also possible to define the Capillary number instead of the Deborah number (Taylor, 1932, 1934)

If droplet deformation into oblate or prolate configurations is assumed to depend on the viscoelastic properties of the interface, instead of the Newtonian viscosity of the droplet phase, one may introduce an interfacial viscosity, $\eta^* = \Gamma\lambda_S$, and define $p^* = -\eta^*/\eta_c$. Then, if $\eta_c = G\lambda_C$ is identified as a Maxwellian viscosity of the continuous phase

$$p^* = -\frac{\Gamma\lambda_S}{G\lambda_C}. \quad (3.7b)$$

Now the coefficient p^* is determined through the linear viscoelastic properties of the matrix and the interface and emulsion behavior does not depend on the Newtonian viscosity of the droplet liquid. Consequently, for this choice of p^* droplet deformation is governed by a single dimensionless group and the Deborah or Capillary number is

¹The point that p^* is a negative number will become clear below, when we evaluate the rate of mechanical energy dissipation due to droplet relaxation, Eq. (3.9).

the negative inverse of p^* (*cf.* Sec. 4.1). In the sample calculations of Chap. 4 and 5 we investigate the model equations for both definitions of the coefficient p^* , Eqs. (3.7).

There is no universal recipe available to determine the phenomenological parameter, θ , and there are several possibilities how this coefficient could be related either to morphological or viscometric properties of the blend: If morphological properties of the blend can be measured easily in a well-defined flow field (*e. g.* in steady shear flow) then one might study the corresponding solutions of the system equations as a function of θ and use the value for θ that gives the most satisfactory fit to experimental data. If morphological properties cannot be measured easily, then one might refer to nonlinear viscometric properties of the blend and to calculate these properties as a function of the coupling parameter from the time evolution equations. This method has been proposed in Edwards et al. (1996) where the negative ratio of the normal stress differences has been chosen as the viscometric property from which to obtain a value for the coupling parameter.

3.1.6. Mechanical Energy Dissipation

We show next that it is important to evaluate the rate of mechanical energy dissipation in the fluid. This property determines if the dynamics of the system described by Eq. (2.1), is thermodynamically admissible for a given set of phenomenological coefficients λ_C , λ_S , p^* , θ in Eqs. (3.5)

The rate of mechanical energy dissipation generated by the Hamiltonian, Eq. (3.4), is given as

$$\frac{dH_m}{dt} = [H_m, H_m] \leq 0, \quad (3.8)$$

and is a decreasing function of time (Beris and Edwards, 1994). Equation (3.8) is obtained directly from Eq. (2.1) considering the antisymmetry of the Poisson bracket and the fact that mechanical energy has to be dissipated into internal degrees of freedom in the long time limit.

Inequality (3.8) is the appropriate condition to give a physically meaningful description of the system, and it can lead to counterintuitive results for the range of thermodynamically admissible phenomenological coefficients adopted herein. Mathematical criteria which are imposed directly onto the dissipative phenomenological coefficients, *e.g.*, on the relaxation times, λ_C and λ_S , on the coupling parameter, θ , or on the dissipative coefficient, p^* , do not necessarily satisfy Inequality (3.8), and may therefore lead to aphysical results. This will become evident in the following paragraph, where we notice

that the dissipative phenomenological coefficient, p^* , has to be negative to account for a physically meaningful droplet relaxation according to the phenomenological matrix of Eq. (3.5b).

For the dissipation bracket of Eq. (3.2), Inequality (3.8) is equivalent to

$$\begin{aligned}
 [H_m, H_m] &= [H_m, H_m]_C + [H_m, H_m]_S + [H_m, H_m]_{CS} \\
 &= -\frac{(1-\phi)^2 G}{2\lambda_C} \int \left(\frac{K}{k_B T} I_1^C + \frac{k_B T}{K} I_{-1}^C - 6 \right) d^3x \\
 &\quad - \frac{(1+p^*)^2 p^* \phi^2 \Gamma}{2\lambda_S} \int \left(3 - \frac{1}{3} I_1^S I_2^S \right) d^3x \\
 &\quad - \frac{p^* \phi^2 \Gamma}{\lambda_S} \int I_2^S \left(3 \frac{I_1^S}{(I_2^S)^2} - 1 \right) d^3x \\
 &\quad - \frac{(1+p^*)^2 \phi (1-\phi) \theta \sqrt{G\Gamma}}{\sqrt{\lambda_C \lambda_S}} \frac{K}{k_B T} \times \\
 &\quad \times \int \left(I_1^S C_{\alpha\beta} S_{\alpha\beta} - C_{\alpha\gamma} S_{\beta\gamma} S_{\alpha\beta} - \frac{2}{3} I_1^C I_2^S \right) d^3x \leq 0,
 \end{aligned} \tag{3.9}$$

where $I_{-1}^C = C_{\alpha\alpha}^{-1} = I_2^C / I_3^C$. The first integral is the mechanical energy dissipation of a Maxwell fluid, $[H_m, H_m]_C$, the second and third integrals are the mechanical energy dissipation due to droplet relaxation including oblate and prolate relaxation, $[H_m, H_m]_S$, and the fourth integral is the rate of mechanical energy dissipation due to the irreversible coupling of the matrix fluid and the droplet interface, $[H_m, H_m]_{CS}$. Each of the first three integrals on the right-hand side of Eq. (3.9) has to be negative since they account for matrix chain relaxation and droplet retraction, respectively. This specifies the range of thermodynamically admissible phenomenological coefficients, λ_C , λ_S , p^* . Furthermore, the last integral should be negative since the irreversible coupling between the two phases should not lead to an increase of mechanical energy in the long time limit. If one of the four integrals was positive, the mechanical dissipation rate could become positive for specific values of the physical variables.

In the following, we want to evaluate generically the four integrals in Eq. (3.9) for start-up of homogeneous, weak shear flow, $\dot{\gamma} \ll 1$, and for vanishing coupling parameter, $\theta = 0$, to find the correct range of the thermodynamically admissible phenomenological coefficient p^* . Numerical calculations (*cf.* Fig. 4.1) corroborate that the scalar invariants of the structural variables increase upon start-up of steady shear flow (except the third invariant of the droplet shape tensor, $\det \mathbf{S} = 1$). The invariant I_{-1}^C assumes values above its equilibrium value, $I_{-1}^C = 3K/(k_B T)$; however, the variations in I_{-1}^C are small compared to the variations of I_1^C . Therefore, the first integral in Eq. (3.9) is negative since the expression in parentheses is positive (the relaxation times, λ_C , λ_S , and the elastic moduli, G , Γ , are positive numbers). Due to $I_1^S \geq 3$ and $I_2^S \geq 3$, the expressions

3. Modeling

in parentheses in the second and the third integrals are negative. Consequently, the phenomenological friction coefficient, p^* , has to be negative to give a negative dissipation rate due to droplet relaxation.

Neglecting the prolate contribution in Eq. (3.5b) for the time being (but still keeping $\theta = 0$), we notice that the range of thermodynamically admissible phenomenological coefficients λ_C , λ_S , and p^* in the two relaxation matrices (3.5a) and (3.5b) is different, although both expressions have an identical mathematical form. The deduction of the thermodynamic admissibility criterion $p^* < 0$ from Eq. (3.5b), arguing that the droplets relax to the lowest energy state of the spherical droplet in absence of entropic forces and flow, is not obvious. Instead the admissibility criterion $p^* < 0$ is obtained from Eq. (3.8). Our analysis shows that the constraint $\det(\mathbf{S}) = 1$ and the functional form of the thermodynamic potential, $E_S = 1/2\Gamma\phi I_2^S$, produce this counterintuitive example of a phenomenological dissipative coefficient being negative. Nevertheless, if p^* is taken as positive, then there is a direct violation of the Second Law of Thermodynamics. This is the reason why the coefficient f_1 has been taken as a negative number in the Toy Model of Sec. 1.2.

For a vanishing coupling parameter, $\theta = 0$, the last integral in Eq. (3.9) is zero. For a small value of the coupling parameter, $\theta \ll 1$, the coupling parameter has to be positive to yield a negative dissipation of mechanical energy due to the coupling between the two variables. Note that the possibility of a negative phenomenological friction coefficient was also found in Edwards et al. (1996), where the coupling parameter was shown to be $\theta \in [-1, 1]$. Furthermore, note that the aspect of a negative friction coefficient in the droplet configuration equation is not worked out rigorously in Grmela et al. (2001) and Yu et al. (2002).

3.1.7. Model Equations

To complete the modeling of emulsions with matrix phase viscoelasticity we shall now obtain the equations for the thermodynamic fields \mathbf{M} , \mathbf{C} , \mathbf{S} . Evaluating the Volterra derivatives of the Hamiltonian (3.4) and inserting the phenomenological matrices of Eqs. (3.5) into Eqs. (3.3), we obtain the following set of time evolution equations:

$$\rho \frac{\partial v_\alpha}{\partial t} = -\rho v_\beta \nabla_\beta v_\alpha - \nabla_\alpha p + \nabla_\beta \sigma_{\alpha\beta}, \quad (3.10a)$$

$$\begin{aligned} \frac{\partial C_{\alpha\beta}}{\partial t} = & -v_\gamma \nabla_\gamma C_{\alpha\beta} + C_{\alpha\gamma} \nabla_\gamma v_\beta + C_{\beta\gamma} \nabla_\gamma v_\alpha - \frac{1-\phi}{\lambda_C} C_{\alpha\beta} + \frac{k_B T}{\lambda_C K} (1-\phi) \delta_{\alpha\beta} \\ & - \frac{1}{2} \sqrt{\frac{\Gamma}{G}} \frac{(1+p^*)^2 \phi \theta}{\sqrt{\lambda_C \lambda_S}} \left[(I_1^S \delta_{\gamma\epsilon} - S_{\gamma\epsilon})(C_{\alpha\gamma} S_{\beta\epsilon} + C_{\beta\gamma} S_{\alpha\epsilon}) - \frac{4}{3} I_2^S C_{\alpha\beta} \right], \end{aligned} \quad (3.10b)$$

$$\begin{aligned}
 \frac{\partial S_{\alpha\beta}}{\partial t} = & -v_\gamma \nabla_\gamma S_{\alpha\beta} - \frac{2}{3} \nabla_\gamma v_\gamma S_{\alpha\beta} + S_{\alpha\gamma} \nabla_\gamma v_\beta + S_{\beta\gamma} \nabla_\gamma v_\alpha \\
 & - \frac{(1+p^*)^2 p^* \phi}{\lambda_S} \left(\frac{1}{3} I_1^S S_{\alpha\beta} - S_{\alpha\gamma} S_{\gamma\beta} \right) + \frac{p^* \phi}{\lambda_S} \left(S_{\alpha\beta} - \frac{3\delta_{\alpha\beta}}{I_2^S} \right) \\
 & - \frac{K}{2k_B T} \sqrt{\frac{G}{\Gamma}} \frac{(1+p^*)^2 (1-\phi)\theta}{\sqrt{\lambda_C \lambda_S}} \left(C_{\alpha\gamma} S_{\beta\gamma} + C_{\beta\gamma} S_{\alpha\gamma} - \frac{2}{3} I_1^C S_{\alpha\beta} \right).
 \end{aligned} \tag{3.10c}$$

The elastic extra stress tensor in the Cauchy Momentum balance equation is a linear combination of the extra stress tensor of the two components. With Eq. (3.4), the general expression of Eq. (3.3d) for the extra stress tensor is equivalent to

$$\begin{aligned}
 \sigma_{\alpha\beta} = & \sigma_{\alpha\beta}^C + \sigma_{\alpha\beta}^S \\
 = & (1-\phi) (n_C K C_{\alpha\beta} - n_C k_B T \delta_{\alpha\beta}) + \Gamma \phi \left(I_1^S S_{\alpha\beta} - S_{\alpha\gamma} S_{\gamma\beta} - \frac{2}{3} I_2^S \delta_{\alpha\beta} \right).
 \end{aligned} \tag{3.10d}$$

For the dilute regime ($\phi \rightarrow 0$), we have mainly a stress contribution due to the matrix phase and the droplet configuration is governed by the coupling term in Eq. (3.10c). For the concentrated regime ($\phi \rightarrow 1$), the extra stress is due to the droplet phase and the non-linear coupling terms are the only contributions in the conformation tensor evolution equation, Eq. (3.10b). Equation (3.10d) is consistent with the extra stress tensor obtained by Grmela et al. (2001).

Equation (3.10b) is the conformation tensor equation. For $\theta = 0$, we obtain the relaxation terms of the UCMM and our set of equations reduces to an uncoupled multi-mode model. For $\theta \neq 0$ and $p^* \neq -1$, we have a non-trivial coupling of the droplet phase to the matrix. This means that the droplet deformation induces changes in the average conformation of the molecules in the matrix phase. Equation (3.10c) is the droplet shape equation dynamics. The first four terms on the right hand side of Eq. (3.10c) are the reversible contribution to the \mathbf{S} -dynamics, the fifth term accounts for oblate droplets and the sixth term accounts for prolate droplets. The last term captures the influence of the local polymer conformation in the matrix phase on the shape and relaxational behavior of the droplets, and it gives oblate droplets for $\theta > 0$. It arises from the phenomenological matrix (3.5c) and it is the most simple representation of matrix-droplet coupling compatible with the Second Law of Thermodynamics.

It is useful to discuss the emulsion model (3.10) for several limiting cases of the viscosity ratio, p^* , and to explore the consequences for matrix microstructure, droplet shape, and matrix-droplet coupling. This is easily achieved giving a closer look to the system equations (3.10). Let us explore equi-viscosity emulsions, $p^* = -1$, emulsions with vanishing interfacial tension, $p^* = 0$, and droplets with large interfacial tension, $p^* = -\infty$.

3. Modeling

For $p^* = -1$, *i.e.*, equi-viscosity blends, the oblate term in the droplet configuration equation and the coupling terms drop out and we recover a model of the MM type together with a UCMM. Note that for equi-viscosity blends, the droplet deformation in the MM model is described by the upper-convected time derivative and the prolate relaxation term since the degree of non-affine motion was taken as $f_2 = 5/(3 - 2p^*)$ in Maffettone and Minale (1998); consequently, it vanishes for equi-viscosity liquids. For $p^* \neq -1$, the prolate contribution in the droplet configuration equation and the coupling terms become different from zero, and the droplets deform into non-axisymmetric shapes for start-up of steady shearing flow. In the MM model this effect is obtained through the inclusion of the Gordon-Schowalter derivative into the droplet configuration equation.

For $p^* \rightarrow 0^-$, the interfacial tension between the two phases is negligible, and variations of the droplet shape are due to the coupling of the viscoelastic matrix to the droplets, *i.e.*, the last term in Eq. (3.10c). Vice versa, droplet deformation induces structural changes in the matrix fluid via the coupling term in Eq. (3.10b). The coupling term in Eq. (3.10b) is a consequence of the modeling approach and it ensures thermodynamic consistency of the partial differential equations. Consequently, droplet deformation is always coupled with structural changes in the matrix for thermodynamic consistency requirements. However, for specific choices of the physical parameters (G , λ_C) and (Γ , λ_S), the coupling terms in Eq. (3.10b) can be small compared to those in Eq. (3.10c) so that there is only a small effect of droplet deformation on the structural properties of the matrix. Note that in the limit $p \rightarrow 0^-$, the degree of non-affine motion as defined in Maffettone and Minale (1998) is $f_2 = 5/3 > 1$. For this value of f_2 , the deformation of the droplets is not described by the usual Gordon-Schowalter derivative since $f_2 \notin [-1, 1]$.

For $p^* = -\infty$, the droplet relaxation terms in Eq. (3.10c) become the dominant ones, and the drops behave like rigid particles (note that the coupling term in Eq. (3.10b) vanishes for $\mathbf{S} = \boldsymbol{\delta}$, *i.e.*, in the undeformed state or for non-deformable droplets). For the dilute regime, $\phi \rightarrow 0$, only the coupling term in Eq. (3.10c) is different from zero, which predicts oblate droplet shapes. However, the presence of the droplet phase allows changes in the local polymer conformation of the matrix phase constituents.

We conclude this section remarking that the emulsion model reduces to a model in the spirit of the Toy Model for equi-viscosity conditions, $p^* = -1$, vanishing matrix-droplet interaction, $\theta = 0$, and in the limit of diluteness $\phi \rightarrow 0$. In this case we recover drops which deform into prolates and the extra stress tensor of Eq. (1.1d).

3.2. Break-up and Coalescence

Let us now model an emulsion with a narrow, non-uniform droplet size distribution. We assume that the Weibull distribution function (Bronshtein and Semendyayev, 1985),

$$f(R) = \frac{1}{V} \gamma q R^{q-1} e^{-\gamma R^q}, \quad (3.11)$$

gives a reasonable description of the average droplet size distribution, where $R > 0$ is a dimensionless droplet radius, $f(R)$ is the number density of micro-droplets with radii between R and $R + dR$ per unit volume, V , and $q > 1$, $\gamma > 0$ are positive real numbers. Note that the above droplet distribution function (DDF) is fully specified if the location, \tilde{R} , and the height, $f(\tilde{R})$, of its absolute maximum are known. Therefore, we can introduce two representative thermodynamic variables to account for the non-uniform droplet morphology of the polymer blend. Another droplet distribution function (DDF), such as the log-normal distribution (Caserta et al., 2004), can also be adopted if desired.

We should explain how to obtain the DDF (3.11) from the thermodynamic variables \mathbf{S} , n because the emulsion model is developed in terms of \mathbf{S} , n . However, in our sample calculations of Sec. 4.2 we want to study the DDF. To obtain the DDF (3.11) from the variables \mathbf{S} , n we use the one-to-one relationship between the parameters, q , γ , in the Weibull distribution function and the thermodynamic variables, \mathbf{S} , n . The parameter q is obtained by solving the non-linear equation $n = f(\tilde{R})$, where $\tilde{R} \equiv 1/3\text{tr}\mathbf{S}$ is the location of the maximum of the DDF and n , \mathbf{S} are solutions of the continuum equations for a given initial and boundary conditions. Then also the second parameter of the Weibull distribution function is fixed since $\tilde{R}^q = (q-1)/\gamma q$.

3.2.1. System Variables

The macroscopic flow of the emulsion is quantified in terms of the momentum density field, \mathbf{M} , defined as the velocity of a fluid particle, \mathbf{v} , times its density, ρ . The average orientation and deformation of the matrix molecules at a fixed position in space is described in terms of the contravariant, second-rank conformation tensor field, \mathbf{C} . The droplet shape tensor, \mathbf{S} , is related to the location of the maximum of the DDF, $\text{tr}\mathbf{S}/3 \equiv \tilde{R}$, and is a contravariant, second-rank tensor field, with the constraint $\det \mathbf{S} = 1$ to account for volume preservation of the micro-droplets. A scalar variable, n , which represents the average number density of micro-droplets of representative shape \mathbf{S} , is related to the height of the maximum of the DDF, $n \equiv f(\tilde{R})$. We emphasize that the two internal variables, \mathbf{S} and n , are representative microstructural variables of the polymer

blend. The full droplet morphology is described in terms of an appropriate DDF, here $f(R)$. Hence our set of thermodynamical variables is $x \equiv [\mathbf{M}, \mathbf{C}, \mathbf{S}, n]$.

3.2.2. Droplet Number Equation

To obtain a set of continuum equations using Eq. (2.1), one has to specify the Poisson bracket, the dissipation bracket, and the generator of the dynamics. Now the Poisson bracket needs to be expressed in terms of $x = [\mathbf{M}, \mathbf{C}, \mathbf{S}, n]$. The Poisson bracket in terms of \mathbf{M} , \mathbf{C} , and \mathbf{S} has been given in the previous section. Due to the variable number density of droplets an additional integral has to be added to the Poisson bracket (3.1) which represents the Poisson bracket for the scalar variable n .

$$\{F, H_m\}^n = - \int \left[\frac{\delta F}{\delta n} \nabla_\beta \left(\frac{\delta H_m}{\delta M_\beta} n \right) - \frac{\delta H_m}{\delta n} \nabla_\beta \left(\frac{\delta F}{\delta M_\beta} n \right) \right] d^3x. \quad (3.12)$$

The bracket constructed from Eq. (3.1) plus the above sub-bracket (3.12) is the bracket for the variables $x = [\mathbf{M}, \mathbf{C}, \mathbf{S}, n]$.

Also for the dissipation bracket, we have to generalize Eq. (3.2) to take into account the variable number density of droplets

$$[F, H_m]^n = - \int \Lambda^n \frac{\delta F}{\delta n} \frac{\delta H_m}{\delta n} d^3x. \quad (3.13)$$

This sub-bracket with the phenomenological matrix Λ^n is the relaxation of the representative number density of micro-droplets in the fluid. Together with Eq. (3.2) this sub-bracket is adopted to describe the irreversible dynamics for an emulsion which can show droplet break-up and coalescence.

An irreversible coupling of the number density of droplets with the droplet shape tensor, \mathbf{S} , is not considered in Eq. (3.13) because it gives an antisymmetric contribution to the dissipation bracket, which does not contribute to the rate of mechanical energy dissipation. We wish to consider only contributions to the dissipation bracket that yield a non-vanishing rate of mechanical energy dissipation. (This is a completely arbitrary consideration, but we believe that it is better for a preliminary work to keep the final set of evolution equations as simple as possible.) The rate of mechanical energy dissipation associated with the new dissipation bracket, Eq. (3.13), is discussed below.

The Poisson and dissipation sub-brackets yield the following general dynamical evolution equation for the number density of micro-droplets

$$\frac{\partial n}{\partial t} = -\nabla_\alpha (n v_\alpha) - \Lambda^n \frac{\delta H_m}{\delta n}. \quad (3.14)$$

where the first term on the right hand side is the reversible contribution from the Poisson bracket and the second term is the irreversible term from the dissipation bracket.

3.2.3. System Hamiltonian

Next we make a constitutive assumption for the Hamiltonian functional, which represents the total energy of the polymer blend. Again, similar as before, we study a system that is envisioned as a superposition of a Maxwell fluid with characteristic elastic constant, K , an elastic droplet interface with interfacial tension, Γ' , and a non-linear coupling of matrix and interfacial elasticity with the variable number density, n , of representative micro-droplets, \mathbf{S} :

$$\begin{aligned} H_m[\mathbf{M}, \mathbf{C}, \mathbf{S}, n] &= K[\mathbf{M}] + A[\mathbf{C}, \mathbf{S}, n] \\ &= \int \left[\frac{M_\alpha M_\alpha}{2\rho} + \frac{1}{2}(1 - \phi)G \frac{K}{k_B T} I_1^C - \frac{1}{2}(1 - \phi)G \ln(\det \frac{K\mathbf{C}}{k_B T}) \right. \\ &\quad \left. + \frac{1}{2}\phi\Gamma \frac{n}{n_0} I_2^S - \frac{1}{6}\phi\Gamma \frac{K}{k_B T} \ln\left(\frac{n}{n_0}\right) I_1^C \epsilon(I_1^S, I_2^S) \right] d^3x. \end{aligned} \quad (3.15)$$

In this expression, I_n^C and I_n^S denote the n -th invariant of \mathbf{C} and \mathbf{S} , respectively, $\phi = 1/V \int_0^\infty f(R)dR$ is the constant total volume fraction of droplets, G is the elastic modulus of the matrix, $\Gamma = \Gamma'/R_0$ where R_0 is a representative droplet radius in the undeformed state, n_0 denotes the representative number density of micro-droplets at equilibrium, and $\epsilon = \epsilon(I_1^S, I_2^S)$ is a measure for the asphericity of the droplets.

Equation (3.15) represents the kinetic energy of the system (first term in the integral) plus a linear superposition of the Helmholtz free energy of a system of Hookean springs (second and third terms) and the energy of the elastic interface, with I_2^S being associated with the surface area (fourth term). Note that the energy of the elastic interface is proportional to the relative number of micro-droplets, n/n_0 , and therefore increases linearly with n . To represent the dynamic effects that determine the number density of droplets away from equilibrium, a fifth term is added to the Hamiltonian. We consider here a logarithmic term in n/n_0 similar to the Flory/Huggins mixing term. This mixing term is taken to depend on both microstructural variables, \mathbf{C} and \mathbf{S} . The mixing term depends on the microstructural tensor \mathbf{C} , since the conformation of the matrix molecules influences droplet shape and hence the break-up and coalescence processes. Here, we have chosen a linear dependence of the mixing term on the trace of the conformation tensor, I_1^C , for simplicity. Furthermore, the mixing term depends on the average asphericity of the micro-droplets, which can be expressed in terms of the non-unit scalar invariants of the droplet shape tensor, $\epsilon = \epsilon(I_1^S, I_2^S)$. Here we take the first invariant of the droplet configuration tensor, $\epsilon = I_1^S$, to express the asphericity of the droplet. Consequently,

we have $\epsilon = 3$ at equilibrium and $\epsilon \rightarrow \infty$ as the micro-droplets are stretched into long fibers or compressed into thin sheets. More elaborate expressions for the asphericity parameter in terms of the first and the second invariants of the droplet shape tensor can be introduced if necessary.

The subscript “m” in the Hamiltonian denotes that the description of the polymer blend is purely mechanical; *i.e.*, we will not consider the transfer of mechanical energy into internal degrees of freedom. Instead, we study an isothermal and incompressible system. Note that Eq. (3.15) duly satisfies the consistency requirement that, at equilibrium in absence of any stress and when the droplet shape is spherical, $\mathbf{S}_{\text{equil}} = \boldsymbol{\delta}$, the Hamiltonian is minimized for $n = n_0$, which can be considered in general as a function of the viscosity ratio and the temperature.

3.2.4. Phenomenological Matrices

We proceed to specify expressions for the phenomenological matrices $\boldsymbol{\Lambda}^C$, $\boldsymbol{\Lambda}^S$, Λ^n , and \mathbf{A} introduced in the dissipation bracket. For the phenomenological matrices $\boldsymbol{\Lambda}^C$, $\boldsymbol{\Lambda}^S$, and \mathbf{A} we adopt the expressions of the previous section, Eqs. (3.5), together with the EWM expression for the relaxation time, λ_C , Eq. (3.6). For the phenomenological matrix Λ^n , the following general expression is introduced:

$$\Lambda^n = 2f_c \frac{n_0 n}{\lambda_n \Gamma}, \quad (3.16)$$

where λ_n is a characteristic time scale of the break-up/coalescence process and f_c is a general function of the phenomenological parameter, p^* , and the scalar invariants of the conformation tensor and the droplet shape tensor, $f_c = f_c(p^*, \tilde{\mathbf{C}}, \mathbf{S})$. This quantity can be related to the probability of the coalescence process (Fortelný, 2001). In what follows, we will take $f_c = 1$ for simplicity; *i.e.*, we neglect a direct influence of the viscosity ratio on the break-up/coalescence processes for simplicity.

Equation (3.16) is the most simple relaxation matrix since it depends linearly on the number density of droplets. Note that the matrices $\boldsymbol{\Lambda}^S$ and \mathbf{A} , Eqs. (3.5), depend on p^* and thus the viscosity ratio will influence break-up and coalescence rates due to the non-linear character of the resulting model equations (3.18).

3.2.5. Mechanical Energy Dissipation

Next we calculate the rate of mechanical energy dissipation in order to evaluate Inequality (3.8) for the rate of mechanical energy dissipation. For the dissipation bracket of

Eq. (3.13), Ineq. (3.8) is equivalent to

$$\begin{aligned}
 [H_m, H_m] &= [H_m, H_m]_C + [H_m, H_m]_S + [H_m, H_m]_n + [H_m, H_m]_{CS} \\
 &= -\frac{1}{2\lambda_C} \int (\text{tr}\tilde{\mathbf{C}}/3)^{-k} \left[(1-\phi)^2 G \left(\frac{K}{k_B T} I_1^C + \frac{k_B T}{K} I_{-1}^C - 6 \right) \right. \\
 &\quad + 2\phi(1-\phi)\Gamma \ln \left(\frac{n}{n_0} \right) I_1^S \left(1 - \frac{K}{3k_B T} I_1^C \right) \\
 &\quad \left. + \frac{1}{9} \phi^2 \frac{\Gamma^2}{G} \left(\ln \frac{n}{n_0} \right) r \frac{K}{k_B T} I_1^C I_1^S I_1^S \right] d^3x \\
 &- \frac{(1+p^*)^2 p^* \phi^2 \Gamma}{2\lambda_S} \int \left[\left(\frac{n}{n_0} \right)^2 \left(3 - \frac{1}{3} I_1^S I_2^S \right) \right. \\
 &\quad \left. + \frac{2}{3} \frac{K}{k_B T} \frac{n}{n_0} \ln \left(\frac{n}{n_0} \right) I_1^C I_2^S \left(\frac{I_1^S I_1^S}{3I_2^S} - 1 \right) \right] d^3x \\
 &- \frac{p^* \phi^2 \Gamma}{\lambda_S} \int \left[\frac{n}{n_0} - \frac{K}{3k_B T} \ln \left(\frac{n}{n_0} \right) \frac{I_1^C}{I_1^S} \right] \\
 &\quad \times \left[\frac{n}{n_0} I_2^S \left(3 \frac{I_1^S}{(I_2^S)^2} - 1 \right) + \frac{1}{6} \ln \left(\frac{n}{n_0} \right) \frac{K}{k_B T} \frac{I_1^C}{I_2^S} (I_1^S I_2^S - 9) \right] d^3x \\
 &- \frac{\phi^2 \Gamma}{2\lambda_n} \int f_c \left(\frac{n}{n_0} I_2^S I_2^S - \frac{2}{3} \frac{K}{k_B T} I_1^C I_1^S I_2^S + \frac{1}{9} \left(\frac{K}{k_B T} \right)^2 (I_1^C I_1^S)^2 \frac{n_0}{n} \right) d^3x \\
 &- \frac{(1+p^*)^2 \phi \theta}{\sqrt{\lambda_C \lambda_S}} \sqrt{\frac{\Gamma}{G}} \frac{K}{k_B T} \int (\text{tr}\tilde{\mathbf{C}}/3)^{-k/2} \left[(1-\phi)G - \frac{1}{3} \phi \Gamma \ln \left(\frac{n}{n_0} \right) I_1^S \right] \\
 &\quad \times \left[\frac{n}{n_0} \left(I_1^S C_{\alpha\beta} S_{\alpha\beta} - C_{\alpha\gamma} S_{\beta\gamma} S_{\alpha\beta} - \frac{2}{3} I_1^C I_2^S \right) \right. \\
 &\quad \left. - \frac{1}{3} \frac{K}{k_B T} \ln \left(\frac{n}{n_0} \right) I_1^C \left(C_{\alpha\beta} S_{\alpha\beta} - \frac{1}{3} I_1^C I_1^S \right) \right] d^3x \leq 0,
 \end{aligned} \tag{3.17}$$

where $I_{-1}^C = C_{\alpha\alpha}^{-1} = I_2^C / I_3^C$. The first integral is the mechanical energy dissipation of a Maxwell fluid, $[H_m, H_m]_C$, the second and third integrals are the mechanical energy dissipation due to droplet relaxation including oblate and prolate relaxation, $[H_m, H_m]_S$, the fourth integral is the rate of mechanical energy dissipation due to the change of the representative droplet number density, $[H_m, H_m]_n$, and the fifth integral is the rate of mechanical energy dissipation due to the irreversible coupling of the matrix fluid and the droplet interface, $[H_m, H_m]_{CS}$. The above expression for the rate of mechanical energy dissipation is negative, if each of the five integrals are negative.

Again, evaluation of the rate of mechanical energy dissipation is essential to generate thermodynamically admissible model predictions. In particular, it is found, that the phenomenological coefficient, p^* , identified with the viscosity ratio is again a negative number.

3.2.6. Model Equations

The last step in the modeling of emulsions with break-up and coalescence is to write down the flow equations for the dynamic variables. We obtain the following set of equations

$$\rho \frac{\partial v_\alpha}{\partial t} = -v_\beta \nabla_\beta v_\alpha - \nabla_\alpha p + \nabla_\beta \sigma_{\alpha\beta}, \quad (3.18a)$$

$$\begin{aligned} \frac{\partial C_{\alpha\beta}}{\partial t} = & -v_\gamma \nabla_\gamma C_{\alpha\beta} + C_{\alpha\gamma} \nabla_\gamma v_\beta + C_{\beta\gamma} \nabla_\gamma v_\alpha - \frac{1-\phi}{\lambda_C} (\text{tr} \tilde{\mathbf{C}}/3)^{-k} C_{\alpha\beta} \\ & + (1-\phi) \frac{k_B T}{\lambda_C K} (\text{tr} \tilde{\mathbf{C}}/3)^{-k} \delta_{\alpha\beta} + \frac{\phi \Gamma}{3 \lambda_C G} (\text{tr} \tilde{\mathbf{C}}/3)^{-k} \ln \left(\frac{n}{n_0} \right) I_1^S C_{\alpha\beta} \\ & - \frac{1}{2} \sqrt{\frac{\Gamma}{G}} \frac{(1+p^*)^2 \phi \theta}{\sqrt{\lambda_C \lambda_S}} (\text{tr} \tilde{\mathbf{C}}/3)^{-k/2} \left\{ \frac{n}{n_0} [(I_1^S \delta_{\gamma\epsilon} - S_{\gamma\epsilon})(C_{\alpha\gamma} S_{\beta\epsilon} + C_{\beta\gamma} S_{\alpha\epsilon}) \right. \\ & \left. - \frac{4}{3} I_2^S C_{\alpha\beta}] - \frac{K}{3 k_B T} \ln \left(\frac{n}{n_0} \right) I_1^C \left(C_{\alpha\gamma} S_{\beta\gamma} + C_{\beta\gamma} S_{\alpha\gamma} - \frac{2}{3} I_1^S C_{\alpha\beta} \right) \right\}, \end{aligned} \quad (3.18b)$$

$$\begin{aligned} \frac{\partial S_{\alpha\beta}}{\partial t} = & -v_\gamma \nabla_\gamma S_{\alpha\beta} - \frac{2}{3} \nabla_\gamma v_\gamma S_{\alpha\beta} + S_{\alpha\gamma} \nabla_\gamma v_\beta + S_{\beta\gamma} \nabla_\gamma v_\alpha \\ & - \frac{(1+p^*)^2 p^* \phi}{\lambda_S} \frac{n}{n_0} \left(\frac{1}{3} I_1^S S_{\alpha\beta} - S_{\alpha\gamma} S_{\gamma\beta} \right) \\ & + \frac{p^* \phi}{\lambda_S} \left[\frac{n}{n_0} - \frac{K}{3 k_B T} \ln \left(\frac{n}{n_0} \right) \frac{I_1^C}{I_1^S} \right] \left(S_{\alpha\beta} - \frac{3 \delta_{\alpha\beta}}{I_2^S} \right) \\ & - \frac{K}{2 k_B T} \frac{(1+p^*)^2 \theta}{\sqrt{\lambda_C \lambda_S}} (\text{tr} \tilde{\mathbf{C}}/3)^{-k/2} \left[(1-\phi) \sqrt{\frac{G}{\Gamma}} - \frac{\phi}{3} \sqrt{\frac{\Gamma}{G}} \ln \left(\frac{n}{n_0} \right) I_1^S \right] \\ & \times \left(C_{\alpha\gamma} S_{\beta\gamma} + C_{\beta\gamma} S_{\alpha\gamma} - \frac{2}{3} I_1^C S_{\alpha\beta} \right), \end{aligned} \quad (3.18c)$$

$$\frac{\partial n}{\partial t} = -\nabla_\alpha (n v_\alpha) - \frac{\phi f_c I_2^S}{\lambda_n} n + \frac{\phi f_c K I_1^C I_1^S}{3 k_B T \lambda_n} n_0. \quad (3.18d)$$

In the appropriate limits, the above set of model equations reduces to the emulsion model of the previous section. For $n = n_0$ we recover flow equations for emulsions with stable droplets. Equation (3.18b) is the conformation tensor equation which now is coupled with the number density equation (3.18d). Thus droplet break-up and coalescence have an influence on matrix flow behavior in our description. The same holds also for the droplet tensor equation (3.18c). We have an effect of break-up and coalescence on droplet shape. For $\theta = 0$, $k = 0$, and $n = n_0$, Eq. (3.18b) reduced to the UCMM. For $\theta \neq 0$ and $p^* \neq -1$, we have a non-trivial coupling of the droplet phase to the matrix phase. Equation (3.18d) is the number density equation with a reversible and two irreversible contributions. The second term on the right hand-side of Eq. (3.18d) has a negative sign and it accounts for a decrease of the representative number density of micro-droplets,

i.e., droplet coalescence. This term is proportional to the number density of droplets, n , *cf.* (Fortelný, 2001). The last term on the right hand-side of Eq. (3.18d) has a positive sign, and it accounts for an increase of the representative number density of droplets, *i.e.* break-up. Note that we have a single time scale for break-up and coalescence, λ_n . Furthermore, note that an equilibrium of coalescence and break-up rates is predicted by Eq. (3.18d) at any steady state. The last two terms on the right hand-side of Eq. (3.18c) represent effective coalescence and break-up rates, which involve the dispersed phase concentration and the invariants of the two structural variables. Though the time scale for coalescence and break-up are identical, the time evolution equations give different rates of coalescence and break-up far from thermodynamic equilibrium.

The elastic extra stress tensor of the blend is the linear combination of the extra stress tensor of the two components. With Eq. (3.15), the general expression of Eq. (3.3d) for the extra stress tensor is equivalent to

$$\begin{aligned} \sigma_{\alpha\beta} &= \sigma_{\alpha\beta}^C + \sigma_{\alpha\beta}^S \\ &= (1 - \phi)G \frac{K}{k_B T} C_{\alpha\beta} - (1 - \phi)G \delta_{\alpha\beta} + \phi \Gamma \frac{n}{n_0} \left(I_1^S S_{\alpha\beta} - S_{\alpha\gamma} S_{\gamma\beta} - \frac{2}{3} I_2^S \delta_{\alpha\beta} \right) \\ &\quad - \frac{\phi \Gamma K}{3k_B T} \ln \left(\frac{n}{n_0} \right) \left[I_1^C S_{\alpha\beta} + I_1^S C_{\alpha\beta} - \frac{1}{3} I_1^C I_1^S \delta_{\alpha\beta} \right]. \end{aligned} \quad (3.18e)$$

This expression generalizes the stress tensor derived for the model with matrix viscoelasticity. For the dilute regime ($\phi \rightarrow 0$), we have mainly a stress contribution due to the matrix phase and the droplet configuration is governed by the coupling term in Eq. (3.18c). For the concentrated regime ($\phi \rightarrow 1$), the extra stress is due to the droplet phase and the non-linear coupling terms are the only contributions in the conformation tensor evolution equation, Eq. (3.18b).

3.3. Surfactants

Emulsions can be unstable against coalescence or spontaneous phase separation, particularly if the continuous phase is low viscous and if the components have different densities. Therefore, surface active molecules are added in order to stabilize microdroplets against coalescence. These surface active molecules have, *e. g.* a hydrophilic and a hydrophobic end-group so that they aggregate at the interface. We assume that interfaces are surfactant covered (*i. e.* the surfactant concentration is larger than the critical micelle concentration) with the result of a stable emulsion, at least on a very long time scale. It is clear that the surface active molecules influence the elastic properties of the interface as well as the response of the interface to an external perturbation.

3. Modeling

Therefore, the elastic free energy of the interface is modified to account for an interfacial elastic modulus which is a function of droplet deformation

$$A[\mathbf{S}] = \frac{1}{2} \int \Gamma(I_1^S, I_2^S) \phi I_2^S d^3x, \quad (3.19)$$

where $\Gamma(I_1^S, I_2^S)$ is an arbitrary function of the first and second scalar invariant of the droplet shape tensor. This function should be obtained, *e. g.* from steady state droplet deformation experiments on covered droplets. If the concentration of surfactant molecules is large and droplet deformation is small a constant interfacial modulus, Γ , is to be adopted. For the relaxation matrix of the interface one can adopt

$$\Lambda_{\alpha\beta\gamma\epsilon}^S = \frac{1}{\Gamma \lambda_S(I_1^S, I_2^S)} \left[\frac{(1+p^*)^2 p^*}{2} (S_{\alpha\gamma} \delta_{\beta\epsilon} + S_{\alpha\epsilon} \delta_{\beta\gamma} + S_{\beta\gamma} \delta_{\alpha\epsilon} + S_{\beta\epsilon} \delta_{\alpha\gamma}) + \frac{3p^*}{I_1^S I_2^S} (\delta_{\alpha\gamma} \delta_{\beta\epsilon} + \delta_{\alpha\epsilon} \delta_{\beta\gamma}) \right], \quad (3.20)$$

i. e. the relaxation time of the interface is a function of the scalar invariants of the droplet shape tensor. One could take, *e. g.* $\lambda_S(I_1^S, I_2^S) = \lambda_{S0} (I_1^S)^{-k}$, where k is a phenomenological parameter. Note that the relaxation time is not taken as a function of the invariants of the rate-of-deformation tensor, but it is a function of the invariants of the droplet shape tensor. Especially for low surfactant concentrations at the interface and for large droplet deformation we expect λ_S to be a strong function of droplet deformation due to advection and diffusion of surfactants. Appropriate constitutive relationships have to be adopted for the relaxation matrix Λ^C and the phenomenological coupling matrix \mathbf{A} . For matrix fluids with low viscosity the relaxation matrix of the UCM Model is to be adopted for Λ^C and effects of matrix deformation on droplet shape can be neglected, $\mathbf{A} = 0$. If \mathbf{A} is non-trivial, the relaxation time λ_S has to be replaced by the variable interfacial relaxation time, $\lambda_S(I_1^S, I_2^S)$.

3.4. Highly Concentrated Emulsions

The models developed so far are intended for the dilute disperse phase regime. We explain how emulsions of high disperse phase concentration can be modeled. First of all we keep in mind that an increase of disperse phase volume fraction can lead to phase inversion. Let us assume therefore, that the highly concentrated emulsion is stable (*e. g.* due to a stabilizing surfactant) and that it is a fluid and not a solid (*i. e.* that the actual configuration can be taken as the reference configuration). In such systems we expect strong droplet-droplet interaction and the dynamics of single droplets is influenced by the neighboring drops. This should have an influence on the drop shape dynamics which

we account for in terms of the phenomenological friction coefficient, ζ . This approach is similar to the Giesekus model for highly concentrated solutions or polymer melts. Consequently, the rheological response of the emulsion is mainly due to the large amount of interface and the Newtonian flow behavior of the disperse phase fluid. Viscoelasticity of the matrix phase plays a minor role since its volume fraction is small. For the phenomenological matrix for interface relaxation we can adopt the following expression

$$\Lambda_{\alpha\beta\gamma\epsilon}^S = \frac{1}{\Gamma\lambda_S} \left[\frac{(1+p^*)^2 p^*}{2} (S_{\alpha\gamma}\delta_{\beta\epsilon} + S_{\alpha\epsilon}\delta_{\beta\gamma} + S_{\beta\gamma}\delta_{\alpha\epsilon} + S_{\beta\epsilon}\delta_{\alpha\gamma}) + \frac{3p^*}{I_1^S I_2^S} (\delta_{\alpha\gamma}\delta_{\beta\epsilon} + \delta_{\alpha\epsilon}\delta_{\beta\gamma}) + \zeta (S_{\alpha\gamma}S_{\beta\epsilon} + S_{\alpha\epsilon}S_{\beta\gamma}) \right], \quad (3.21)$$

which has an additional higher order term with respect to Eq. (3.5b). The number ζ is a phenomenological coefficient which accounts for anisotropic relaxation of the interface. Note that the values of ζ have to be such that the flow equations satisfy the Second Law of Thermodynamics. The Hamiltonian can be taken from the emulsion model with matrix viscoelasticity, since we expect only small deformation.

3.5. Critical Comment on Emulsion Models

Before evaluating the models for flows as encountered in rheometers and simple geometries we should comment on their ability to fit the complicated viscometric behavior of complex fluids. Remember that a single relaxation time as used for the modeling of the continuous phase allows to describe the non-linear viscoelastic behavior only qualitatively. With the EWM Model, *e. g.*, the shear thinning behavior of the viscosity and the first normal stress coefficient are recovered. To model fluids with non-trivial second normal stress coefficients, *e. g.* the Giesekus Model can be used. However, with a single relaxation time it is not possible to recover quantitative predictions for the viscosity and the normal stress coefficients. Therefore, to make quantitative predictions of the viscometric material functions a set of discrete relaxation times is needed (Bird et al., 1987). The use of a single relaxation time for droplet deformation is reasonable if drop behavior is dominated by the interfacial tension between the fluid phases.

4. Rheology

The discussion in this chapter will be concerned with some basic features of the models derived in the previous chapter. The main properties of the models in shear and elongational flows are discussed and the connection with experimental characterization is indicated. By resorting to computational means and by especially reporting results of numerical calculations we shall already be entering the realm of CFD.

4.1. Model with Matrix Viscoelasticity

The set of continuum equations (3.10), is solved for homogeneous deformation velocities, $\nabla \mathbf{v}$, as realized in shear and elongational rheometers and in the stagnation point of the four roll mill apparatus. We use a fourth order Runge-Kutta scheme with adaptive step-size and a Newton-Raphson algorithm (Press et al., 1992) to solve for transient and steady state material properties, respectively. In the long time limit the transient calculation gives the steady state model characteristics. The model equations are rendered dimensionless using $\tilde{t} = t/\sqrt{\lambda_C \lambda_S}$, $\tilde{\mathbf{C}} = K/k_B T \mathbf{C}$, $\tilde{\mathbf{S}} = \mathbf{S}$, and $\tilde{\boldsymbol{\sigma}} = \boldsymbol{\sigma}/(\sqrt{G\Gamma})$. In all that follows, we omit the tilde over dimensionless quantities. The groups that we adopt to render the system of equations dimensionless thus only involve characteristic material properties and intrinsic time scales. The viscosity ratio of the emulsion is defined in terms of the Maxwellian viscosities of the matrix fluid and the interface, *i. e.* $p^* = -(\Gamma \lambda_S)/(G \lambda_C)$, Eq. (3.7b).

With these dimensionless groups and the definition of the coefficient p^* , the Capillary Number is defined as $\text{Ca} = \eta_c R/(\Gamma' \lambda_S)$ in analogy with Edwards and Dressler (2003), *i. e.*, the intrinsic time scale of the viscoelastic interface is adopted in the definition of the Capillary Number instead of the time scale related to the velocity gradient. This is a more physically realistic definition if one incorporates matrix-phase viscoelasticity into the problem because the Capillary is defined in terms of material properties only and it does not depend on space and time. Using the standard definition of Ca, this quantity depends on space and time for transient and non-homogeneous flow fields; hence the advantage gained in using a Ca defined in terms of material properties only. With

the above relationship, we see that the Capillary Number is fixed once the viscoelastic properties of the two phases have been specified: $\text{Ca} = -1/p^*$. The reason for the Capillary Number being the only dimensionless group is the definition of the coefficient p^* in terms of Maxwellian viscosities, Eq. (3.7b).

We discuss sample calculations for various viscosity ratios, p^* , droplet concentration regimes, ϕ , and coupling parameter values, θ . First, we focus on a dilute model emulsion ($\text{Ca} = 4$) with linear viscoelastic properties defined as $G/\Gamma = 4$ for the ratio of elastic strengths and $\lambda_C/\lambda_S = 1$ for the ratio of relaxation times. Furthermore, the model is solved for $\text{Ca} = 0.1, 1, \text{ and } 10$ to discuss the predictions over a larger range of Capillary Numbers, and to compare our equations with the predictions of the MM Model and the ALS Model. The dispersed phase concentration is taken as $\phi = 0.1$ in the sample calculations.

4.1.1. Simple Shear Flow

First, we investigate the system equations for start-up of steady shear flow

$$\nabla \mathbf{v} = \begin{pmatrix} 0 & 0 & 0 \\ \dot{\gamma} & 0 & 0 \\ 0 & 0 & 0 \end{pmatrix}, \quad (4.1)$$

focusing on the non-linear rheological features of the two coupled modes description of the emulsion (Figs. 4.1-4.3). Then, we discuss the steady state rheological and morphological properties (Figs. 4.4 and 4.5)

Figure 4.1 illustrates the transient behavior of the scalar invariants of the structural variables as a function of shear strain, γ , for a given shear rate, $\dot{\gamma}$, and two values of the coupling parameter, θ , according to Eqs. (3.10). In this case, all fields are spatially homogeneous and the integrals in Eq. (3.9) give the total system volume, Ω . The calculations are for the $\text{Ca} = 4$ model emulsion, *i. e.* $p^* = -0.25 < 0$ to satisfy thermodynamic admissibility criteria for the system equations. We note that the invariants of \mathbf{C} (Figs. 4.1a-c) increase upon start-up of steady shear flow, and that they each attain a value greater than their equilibrium values. The solid lines in Figs. 4.1a-c correspond to the single-mode UCMM, and they can be obtained analytically solving this linear viscoelastic model. The first and the second invariant of \mathbf{S} (Figs. 4.1d, e) show a strongly non-linear behavior which is related to the increase of the surface area of the ellipsoidal inclusions. The third invariant of \mathbf{S} is always unity, as prescribed by the constant-volume constraint. Figure 4.1g displays the total rate of mechanical energy dissipation, $[H_m, H_m]/\Omega$, according to Eq. (3.9). Inequality (3.9) should be evaluated in

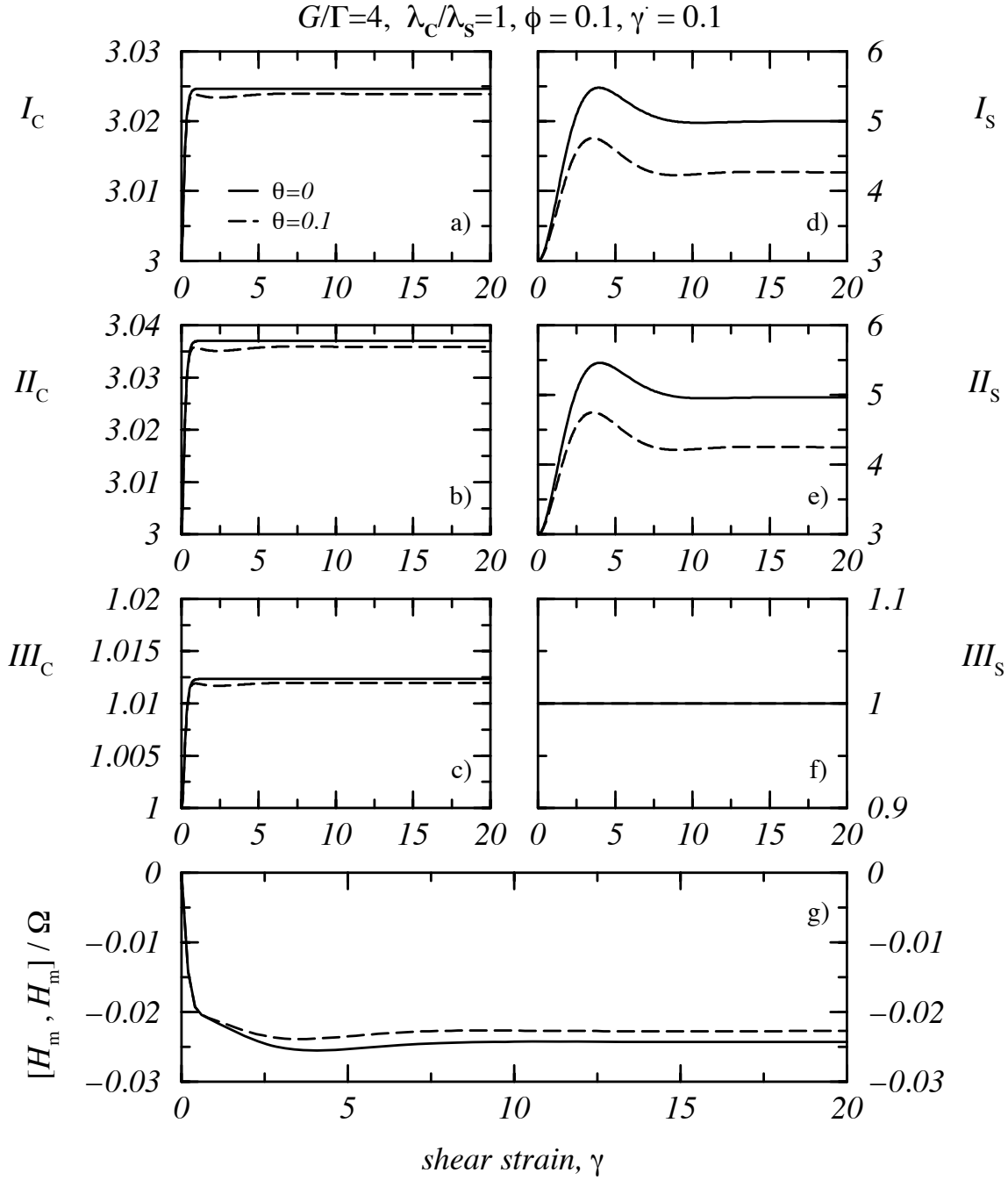


Figure 4.1.: The invariants of the structural variables, \mathbf{C} and \mathbf{S} , and the mechanical dissipation rate, $[H_m, H_m]/\Omega$ for start-up of steady shear flow, $\dot{\gamma} = 0.1$, as a function of strain, γ . The parameters in the model have been specified as follows: $G/\Gamma = 4$ for the ratio of elastic strengths, $\lambda_C/\lambda_S = 1$ for the ratio of relaxation times (*i.e.*, $p^* = -0.25$), and $\phi = 0.1$ for the dispersed phase concentration. We chose two values for the coupling parameter, $\theta = 0$ (solid lines) and 0.1 (dashed lines).

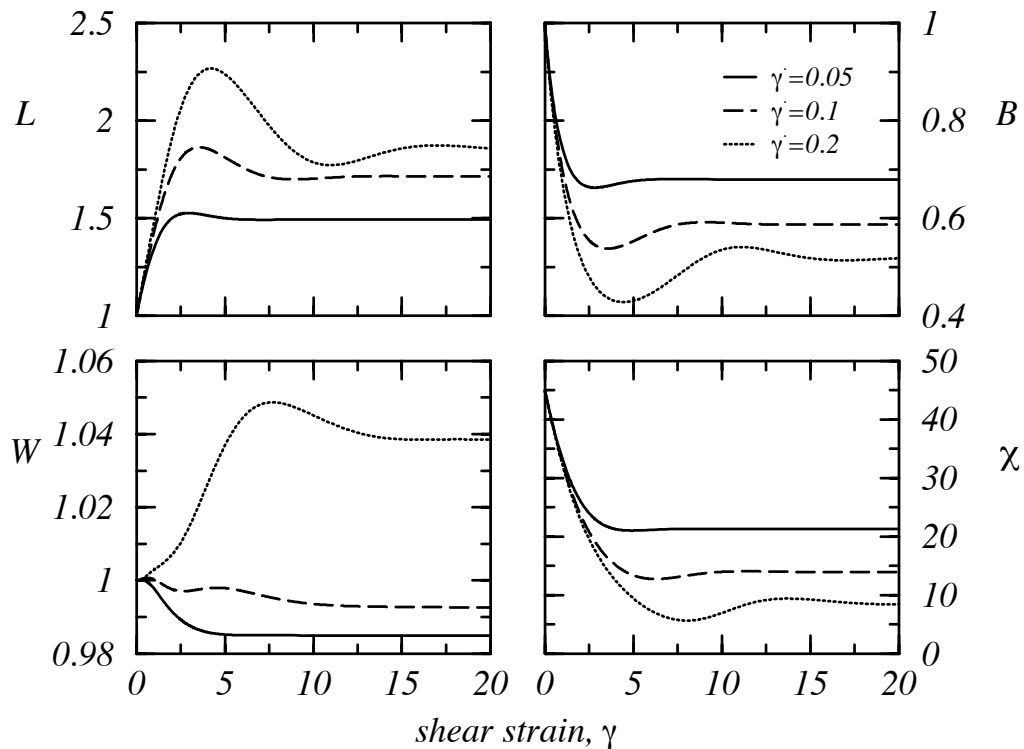


Figure 4.2.: The average semiaxes of the ellipsoidal droplets, L , B , W , and the orientation angle, χ , for start-up of steady shear flow for a coupling parameter, $\theta = 0.1$, and three shear rates $\dot{\gamma} = 0.05$ (solid lines), 0.1 (dashes lines), 0.2 (dotted lines) for the $Ca = 4$ emulsion with dispersed phase concentration $\phi = 0.1$. Depending on the shear rate, the model predicts either oblate droplets ($W > 1$) or prolate droplets ($W < 1$). For $\dot{\gamma} = 0.1$ and small shear strains, we observe a competition between oblate and the prolate configurations.

all flow calculations to ensure that model predictions are compatible with the Second Law of Thermodynamics.

The morphological properties of the disperse phase are represented by the average magnitude of the three semiaxes of the ellipsoidal droplets and the average orientation of the droplets with respect to the flow direction. The semiaxes of the droplets are the square roots of the eigenvalues of the droplet configuration tensor, \mathbf{S} , as already introduced with the Toy Model. The droplet semiaxes in the flow direction, in the direction of the shear gradient, and in the direction of the vorticity axis are denoted with L , B , W , respectively. Upon inception of weak steady shear flow, $\dot{\gamma} \lesssim 1$, the major droplet axis, L , increases and the minor droplet axis, B , decreases. However, the vorticity axis, W , can be greater than, smaller than, or equal to unity upon start-up of flow and the droplets are thus either oblate or prolate: one has oblate droplets for $W > 1$ and prolate droplets for $W < 1$. The orientation angle, χ , is the angle between the eigenvector corresponding

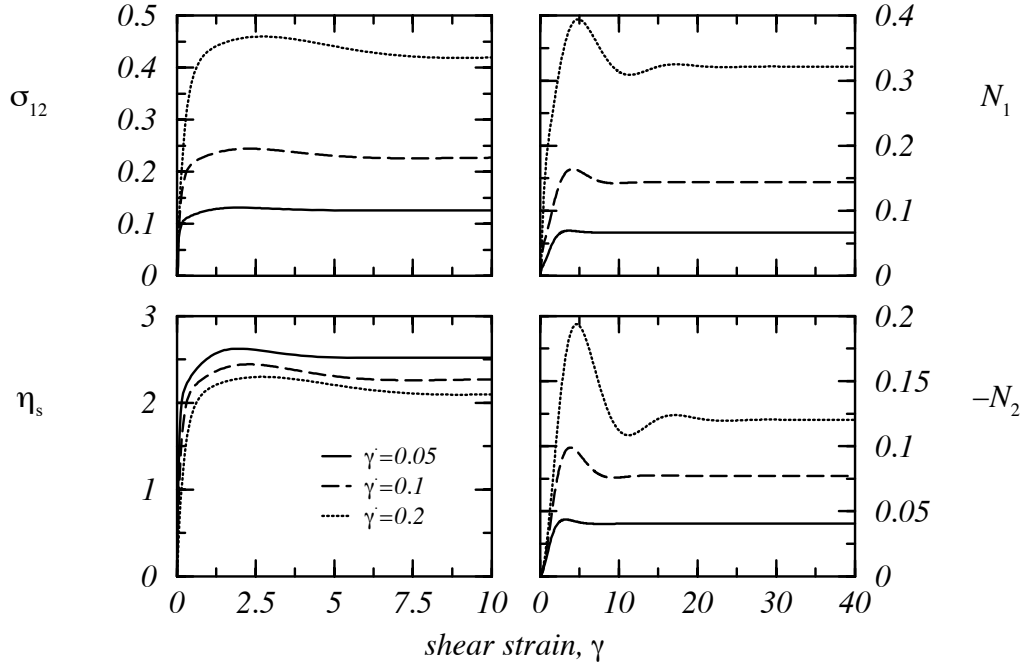


Figure 4.3.: The same as Fig. 4.2 for the transient viscometric properties of the $Ca = 4$ emulsion. The left column shows the start-up behavior of the shear stress and the shear viscosity, σ_{12} and η_s , while the right column displays the start-up behavior of the normal stress differences, N_1 and N_2 .

to the largest eigenvalue of the \mathbf{S} -tensor and the flow direction and it is defined as

$$\chi = \frac{1}{2} \arctan \left(\frac{2S_{12}}{S_{11} - S_{22}} \right). \quad (4.2)$$

Figure 4.2 displays the start-up behavior of the three droplet semiaxes upon inception of steady shear flow for a fixed value of the coupling parameter and three shear rates. We see that the model predicts a transition from the prolate to oblate droplet configurations for increasing shear rate when $\theta \neq 0$. At intermediate shear rates, there is a competition between the prolate and the oblate droplet deformations that ends up in a prolate non-equilibrium state for high shear strains. The start-up behavior of the three semiaxes and the orientation angle for fixed shear rate and various coupling parameters shows also a competition between oblate and prolate droplet configurations. An illustration for $\dot{\gamma} = 0.5$ and $\theta = 0.1, 0.2,$ and 0.4 which results in a steady state prolate droplet configuration can be found in Dressler and Edwards (2004, Fig. 3b).

In Fig. 4.3, we display the transient viscometric properties of the $Ca = 4$ emulsion for three shear rates. The continuum equations derived in the previous section predict a typical non-linear viscoelastic response known from synthetic polymer rheology. The right column in Fig. 4.3 displays the shear stress, σ_{21} , and the shear viscosity, $\eta_s = \sigma_{21}/\dot{\gamma}$,

as a function of shear strain. The shear stress shows a strongly non-linear transient behavior with over- and undershoots, which increase with increasing shear rate. The first normal stress difference, $N_1 = \sigma_{11} - \sigma_{22}$, is positive. Similarly to the shear stress, it shows a non-linear behavior with over- and undershoots, and it is of the same order of magnitude as the shear stress. The second normal stress difference, $N_2 = \sigma_{22} - \sigma_{33}$, is negative and, in the steady state, approximately half the magnitude of the first normal stress difference. The normal stress differences attain a steady state at higher shear strains compared to the shear stress. Finally, the transient shear viscosity, η_S , is also reported in Fig. 4.3; it displays the characteristic shear-thinning behavior. This is illustrated more clearly in Fig. 4.4a where we present the steady-state viscometric properties for the $Ca = 4$ emulsion.

It is interesting to determine correlations between the magnitude of the semiaxes of the ellipsoidal droplets and the viscometric functions of the material. Such a procedure is discussed, e.g., in Yu et al. (2002), who propose correlations between the viscometric properties of polymer blends and higher-order Taylor deformation parameters of the type, $D_{XY} = (X^2 - Y^2)/(X^2 + Y^2)$, where $X, Y \in \{L, B, W\}$ denote the semiaxes of the drop. Possibly, it is more instructive to establish correlations between the semiaxes and the viscometric functions instead of defining generalized Taylor deformation parameters. A comparison of Figs. 4.3 and 4.2 shows, e. g., that the first normal stress difference correlates with the major semiaxis, L , and the second normal stress difference correlates with the minor droplet semiaxis, B . However, such correlations should be used with caution due to the non-linear character of the underlying dynamics. Note that the Taylor Deformation Parameter, $D = (L - B)/(L + B)$, does not give information whether the droplets are oblates or prolates; however, the full droplet shape can be relevant for the viscoelastic response of the emulsion, as the calculations demonstrate. Therefore, the information contained in the Taylor Deformation Parameter is insufficient for correlating viscometric data with morphological characteristics of the emulsion.

The morphological properties of the matrix phase are described in terms of the conformation tensor, \mathbf{C} , being the second moment of the end-to-end vector of the linear polymer chains in the matrix. Upon start-up of steady shear flow the matrix chain conformations start to deviate from their equilibrium value, $\mathbf{C} = \mathbf{1}$, and after several strain rate units one obtains steady state conformations with non-trivial shear and normal conformations, C_{12} and C_{ii} , $i \in \{1, 2, 3\}$, respectively. The non-trivial second and third normal conformations are due to the coupling terms in the model equations. For $\theta = 0$ the conformation tensor equation can be solved analytically to recover the well known results for the UCM Model.

In Fig. 4.4, we present the steady-state viscometric and morphological properties of the $Ca = 4$ emulsion in shear flow. Figure 4.4a shows the viscometric functions for the emulsion with dispersed phase concentration $\phi = 0.1$. We observe a shear-thinning behavior

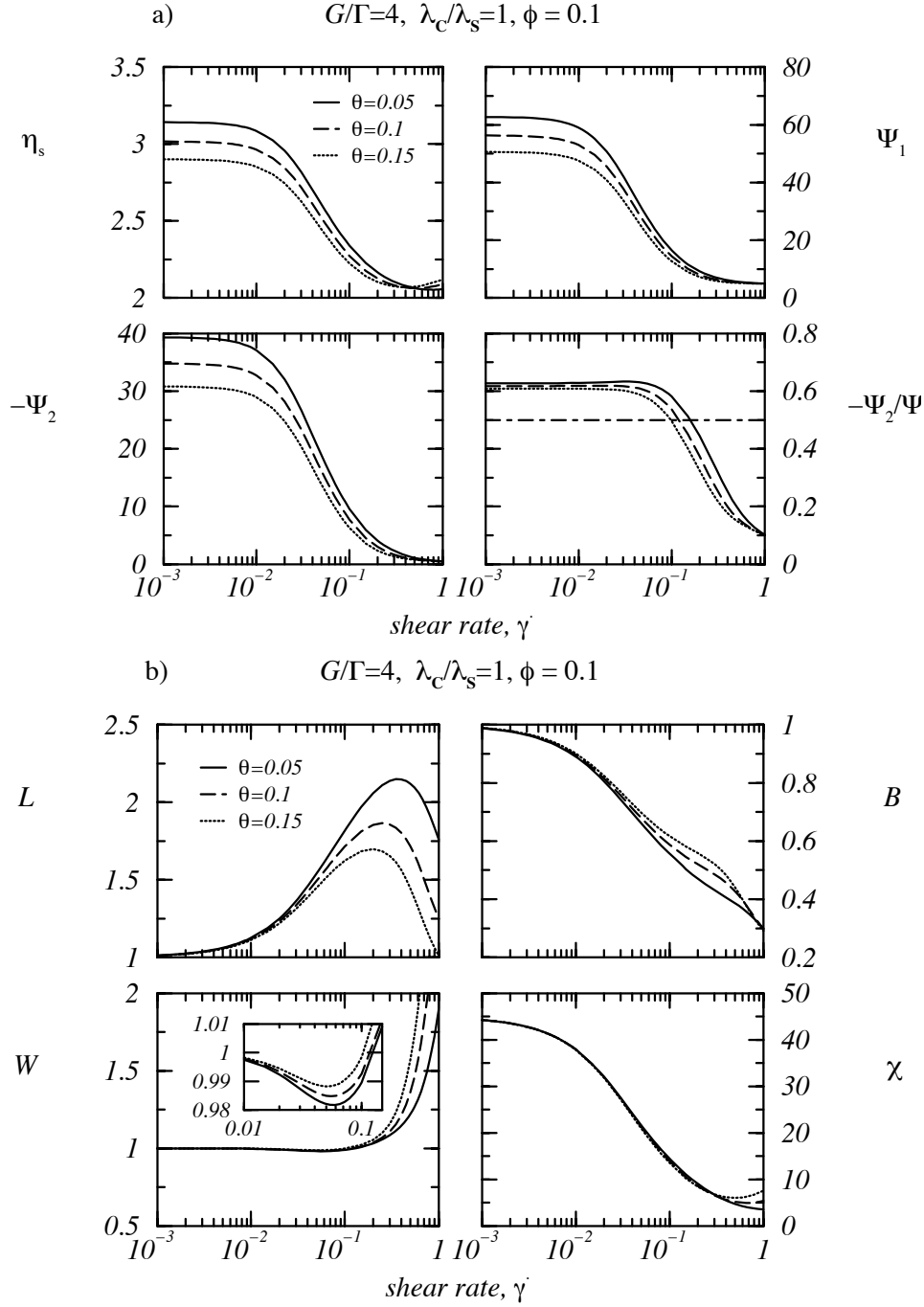


Figure 4.4.: The steady-state viscometric (a) and morphological (b) properties of the $Ca = 4$ emulsion with dispersed phase concentration, $\phi = 0.1$, for three coupling parameter values: $\theta = 0.05$ (solid lines), 0.1 (dashed lines), and 0.15 (dotted lines) in simple shear flow. a) Steady state viscometric functions η_s , Ψ_1 , Ψ_2 and the ratio Ψ_1/Ψ_2 , b) droplet semiaxes L , B , W , and orientation angle, χ .

in the three viscometric functions. The plateau values of the viscometric functions decrease as the coupling parameter is increased. The power-law index of the shear viscosity curve in the shear-thinning region decreases with increasing coupling parameter. However, the power-law indices of the steady-state normal stress coefficients increase with increasing coupling parameter. This is seen more clearly if the viscometric functions are normalized with respect to the zero shear-rate values of the respective flow curves (Dressler and Edwards, 2004, Fig. 8). We find that the shear-thinning regime sets in at shear rates of $\dot{\gamma} \approx 0.01$, and there is a broad transition from the plateau in the low shear-rate regime to the power-law region in the intermediate and high shear-rate regimes. For $\dot{\gamma} \approx 0.2$, the steady-state viscometric functions start to deviate from power-law behavior and a second Newtonian plateau is reached. For even higher shear rates, the onset of a shear-thickening region is observed where the shear viscosity begins to increase again. A dimensionless value of $\dot{\gamma} \approx 1$ corresponds to extremely high shear rates in reality since we have already left the power-law region of the flow curves. Finally, the ratio $-\Psi_2/\Psi_1$ is reported in Fig. 4.4a which varies between 0.1 and 0.6. The dot-dashed lines in Figs. 4.4a is the prediction of the Toy Model, $\Psi_2/\Psi_1 = -0.5$. We realize that our set of equations allows for a more general behavior of the ratio of normal stress differences compared to the Toy Model. We arrive at the important conclusion that the large value of normal stress differences found for the Toy Model is also recovered with an emulsion Model that is constructed in the framework of non-equilibrium Thermodynamics. It is worth to assess these model predictions experimentally.

Our emulsion model, (3.10), allows to predict steady-state viscometric properties over an extremely large shear rate regime that extends from a Newtonian plateau to a power-law regime at low and intermediate shear rates, to a second Newtonian plateau with the a shear-thickening region at high shear rates. The prediction of steady-state viscometric emulsion properties is critical for both the ALS Model and the MM Model. As has been pointed out in Jansseune et al. (2001), the original ALS Model does not yield a steady-state shear stress for start-up of simple shear flow. The problem with the MM Model is that it yields a critical shear rate, $\dot{\gamma}_c = f_1/(\sqrt{f_2^2 - 1} \lambda)$. Beyond $\dot{\gamma}_c$, the droplet shape tensor (and hence the extra stress tensor) increases to infinity for start-up of steady shear flow. Therefore, the steady-state shear viscosity and the first normal stress difference can be predicted only over a limited range of shear rates for the MM Model – see Yu et al. (2002, Fig. 5). Our model does not use the mixed convected derivative for the droplet configuration tensor, but is expressed in terms of the upper-convected derivative. However, this corresponds to $f_2 = 1$ which means $\dot{\gamma}_c \rightarrow \infty$ for the uncoupled set of evolution equations in simple shear flow. In the MM Model, the Gordon-Schowalter derivative has been adopted to describe droplet deformation in blends of Newtonian liquids with a viscosity ratio different from unity. In this article, we do not want to adopt the Gordon-Schowalter derivative since it is an irreversible contribution to the system dynamics which does not lead to dissipation of mechanical energy; i. e., it does not contribute to Eq. (3.8), even though it is irreversible!). Instead, we wish to study the

effect of the oblate relaxation term in Eq. (3.10c) and of the coupling terms in Eqs. (3.10) on the rheological and microstructural properties of the blend.

Figure 4.4b shows the steady-state morphological properties of the ellipsoidal inclusions in the viscoelastic matrix. We observe a strong increase in the major droplet axis, L , which reaches a maximum at $\dot{\gamma} \approx 0.4$ for our $\text{Ca} = 4$ model emulsion. This increase in L correlates with (i) flow alignment of the droplet inclusions since the orientation angle, χ , decreases with increasing shear rate, and (ii) with a strong increase of the vorticity axis, W . The minor droplet axis, B , is a decreasing function of shear rate over the entire range of shear rates investigated herein. A comparison with Fig. 4.4a shows that the increase in the major droplet axis, L , correlates with the beginning of the power-law region that is observed in the steady-state viscometric functions. The decrease of the major droplet axis, L , and the strong increase of the vorticity axis, W , correlate with the approach of the viscometric functions to a second Newtonian plateau. Also, the orientation angle approaches a plateau value for high shear rates, and an increase of χ is observed for $\theta = 0.15$ at very high shear rates.

The important result of Fig. 4.4b is that the major droplet axis is a non-monotonic function of shear rate. This model behavior is qualitatively different from the predictions of the Toy Model, where the major droplet axis is a monotonic function of shear rate. For highly viscous emulsions we expect an influence of matrix deformation on droplet morphology, especially at high shear rates and non-monotonic droplet length should be possible. The non-monotonic droplet length can also be taken as the motivation to include break-up and coalescence into the model.

Summarizing the results of Figs. 4.4b we can identify several steady-state droplet shape regimes. For small shear rates, $10^{-3} \lesssim \dot{\gamma} \lesssim 10^{-2}$, the steady-state droplet shape lies in the prolate deformation regime. The major droplet axis increases with increasing shear rate and the minor droplet axis decreases, whereas the vorticity axis, W , remains almost unity. The droplets are non-symmetric, $B \neq W$. In the intermediate shear rate regime, $10^{-2} \lesssim \dot{\gamma} \lesssim 10^{-1}$, we observe a further stretching of the droplets into prolates, which manifests as a further increase of the L -axis and a further decrease of the B -axis. Simultaneously, the vorticity semiaxis decreases below unity, and the droplets are stretched into long ellipsoids (*cf.* the inset in Fig. 4.4b). In the high shear rate regime, $\dot{\gamma} \gtrsim 0.3$, the vorticity axis shows a strong increase which is compensated by a simultaneous decrease of the major droplet axis to unity; *i. e.*, a compression of the droplets in flow direction. Hence, we recover flat prolates ($B \ll 1$) with major semiaxes $L \approx 1$, which are almost aligned parallel to the shearing planes ($\chi \approx 0$) and extend into the vorticity direction.

Figure 4.5 displays the steady-state shear viscosity and the first normal stress coefficient for the three model emulsions $\text{Ca} = 0.1, 1, \text{ and } 10$. We display results for three coupling

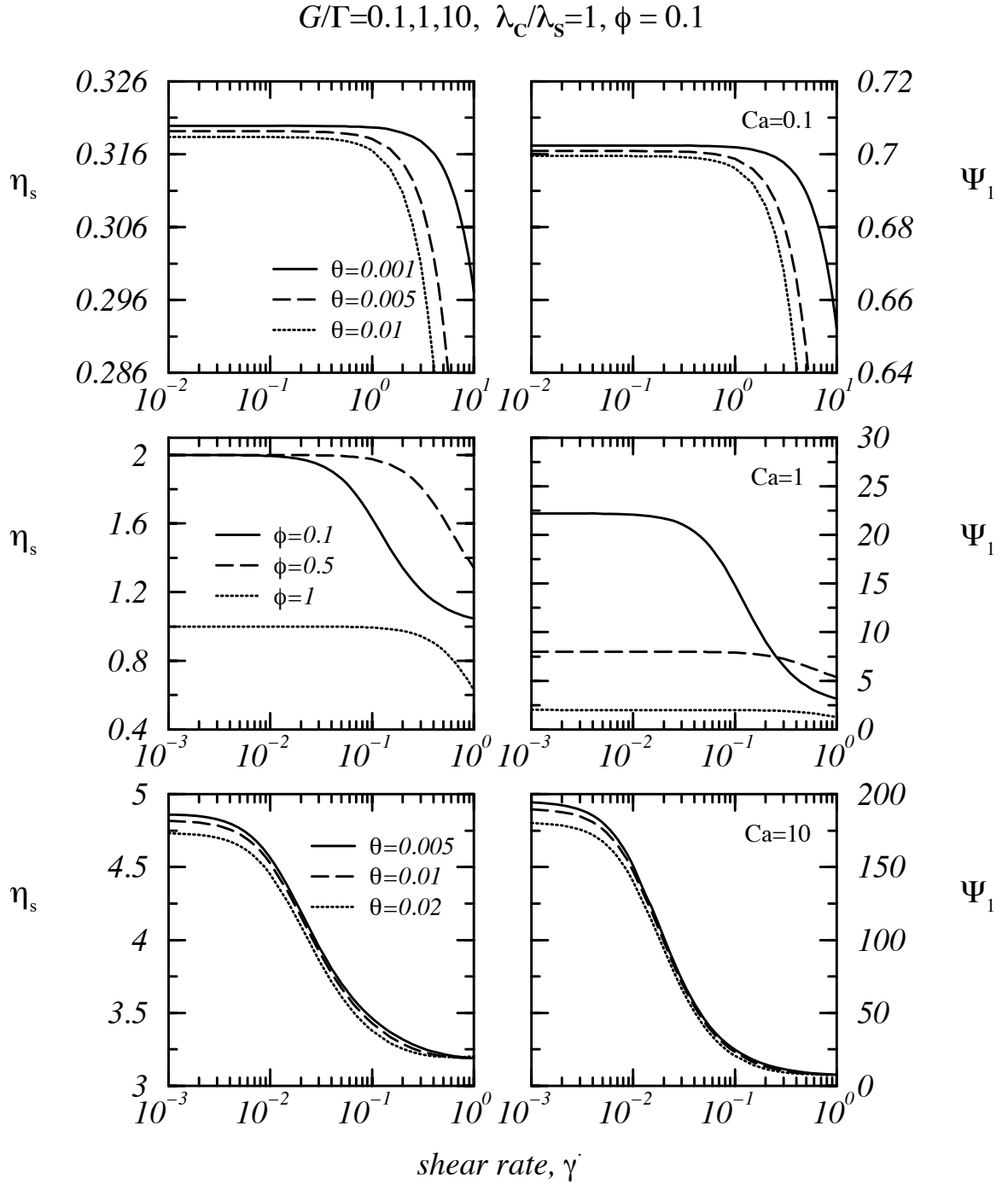


Figure 4.5.: The steady-state shear viscosity, η_s (left column), and the first normal stress coefficient, Ψ_2 (right column), for three emulsions $Ca = 0.1$ (first row), 1 (second row), 10 (third row) with dispersed phase concentration, $\phi = 0.1$, and three coupling parameter values, θ , denoted in the legend within each row. For the $Ca = 1$ emulsion, we show three droplet concentrations.

parameters and droplet concentrations in the three Capillary Number regimes. For the $Ca = 0.1$ emulsion, we note that an increase of the coupling parameter increases the power-law index of the steady-shear viscosity and the first normal stress coefficient curves. This is qualitatively different from the results reported in Figs. 4.4a, where an increase of θ resulted in a decrease of the power-law index of the steady-state shear viscosity. For the $Ca = 1$ emulsion, we report the steady-state viscometric properties for three different droplet concentrations in Fig. 4.5. The case $\phi = 1$ corresponds to the MM Model and it is identical to the stress tensor predictions in Yu et al. (2002). For $Ca = 10$, we observe that the power-law index of the steady-state shear viscosity and the first normal stress coefficient are almost insensitive to a variation of $0.005 \lesssim \theta \lesssim 0.02$.

For the second normal stress coefficient, Ψ_2 , and the ratio of normal stress coefficients, Ψ_2/Ψ_1 , we find that both emulsion characteristics depend strongly on the Capillary number regime (cf. Dressler and Edwards, 2004, Fig. 13). For the low Capillary number regime both quantities are small and constant for shear rates $\dot{\gamma} \lesssim 1$. In the intermediate and in the high Capillary number regime the second normal stress coefficient is large and it shows a pronounced shear thinning behavior. The same is also true for the ratio of normal stress coefficients which is approximately one half in the low shear rate domain.

A comparison of the zero-shear viscometric functions of Fig. 4.5 with experimental data for emulsions and emulsion components would be a worthwhile. Figure 4.5 illustrates that the emulsion has specific zero shear viscometric characteristics and it is not obvious how they are related to the zero shear material functions of the single components, because the zero shear characteristics of the emulsion depend on the phenomenological coupling parameter, θ . Thus, θ can also be determined from zero shear viscometric data of the emulsion and emulsion components.

4.1.2. Elongational Flow

Figure 4.6 summarizes the predictions of the continuum equations in uniaxial elongational flow,

$$\nabla \mathbf{v} = \begin{pmatrix} \dot{\epsilon} & 0 & 0 \\ 0 & -\frac{\dot{\epsilon}}{2} & 0 \\ 0 & 0 & -\frac{\dot{\epsilon}}{2} \end{pmatrix}, \quad (4.3)$$

for the $Ca = 4$ emulsion and dispersed phase concentration $\phi = 0.1$. For uniaxial elongational flow, the droplets maintain a symmetric shape, $B = W$. The left column of Fig. 4.6 displays the transient morphological and rheometrical properties of the emulsion for constant coupling parameter and various elongation rates, $\dot{\epsilon}$. In Fig. 4.6a, we show

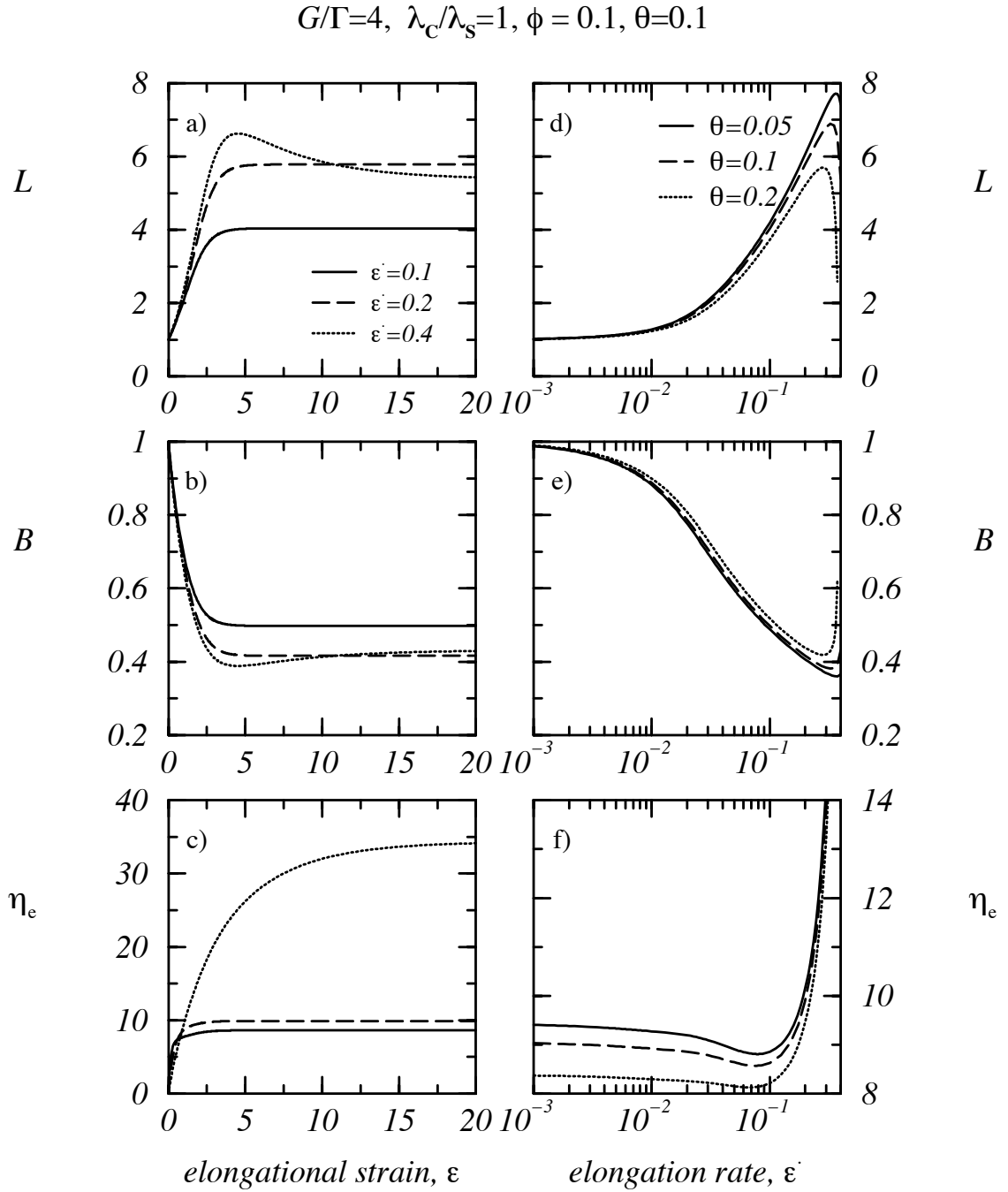


Figure 4.6.: The morphological and viscometric properties of the $Ca = 4$ emulsion with $\phi = 0.1$ dispersed phase concentration in uniaxial elongational flow: (a-c) The transient behavior of the droplet semiaxes and the elongational viscosity for three elongation rates, $\dot{\epsilon} = 0.1$ (solid lines), 0.2 (dashed lines), 0.4 (dotted lines), and $\theta = 0.1$. (d-f) The steady-state properties of the same quantities for three coupling parameter values, $\theta = 0.05$ (solid lines), 0.1 (dashed lines), 0.2 (dotted lines).

the transient behavior of the major semiaxis of the ellipsoidal droplet, L , as a function of elongational strain, $\epsilon = \dot{\epsilon}t$, for three elongation rates. For the two smallest elongation rates, we have a monotonic increase of the major semiaxis and an approach to a steady state. The steady-state value of L increases in this elongation rate region. For the highest elongation rate, we recover an overshoot and a slow relaxation of the major semiaxis to the steady state. Figure 4.6b shows the transient behavior of the minor semiaxis of a droplet, which decreases monotonically for small elongation rates and displays an undershoot for the highest elongation rate examined. In Fig. 4.6c, we report the transient elongational viscosity,

$$\eta_E = \frac{\sigma_{11} - \sigma_{22}}{\dot{\epsilon}}. \quad (4.4)$$

This quantity increases monotonically for start-up of flow and reaches a plateau value at rather low elongational strains. Note that for small elongation rates, the slope of the transient elongational viscosity is bigger than the slope of the transient droplet axis upon start-up of elongational flow. The steady-state morphological and viscometric properties of the model are reported in the right column of Fig. 4.6 for three coupling parameter values. The steady-state behavior of the major droplet axis is shown in Fig. 4.6d. We see that the major semiaxis increases monotonically up to elongation rates $\dot{\epsilon} \approx 0.3$, where it attains a maximum. The steady-state behavior of the minor droplet semiaxis, B , reported in Fig. 4.6e is a decreasing function of elongation rate due to the volume preservation constraint, $LB^2 = 1$. This quantity decreases monotonically for small and intermediate shear rates, and reaches a minimum for $\dot{\gamma} \approx 0.3$. Finally, we display the steady-state elongational viscosity for three coupling parameter values in Fig. 4.6f. For small elongation rates, we observe a slight strain softening of the emulsion which then turns into a pronounced strain hardening as the elongation rate approaches $\dot{\epsilon} \approx 0.1$. The range of coupling parameter values investigated in Fig. 4.6 has only a minor influence on the steady-state morphological and rheological properties in the high elongation-rate regime.

Figure 4.7 presents the predictions of the continuum equations for planar elongational flow,

$$\nabla \mathbf{v} = \begin{pmatrix} \dot{\epsilon} & 0 & 0 \\ 0 & -\dot{\epsilon} & 0 \\ 0 & 0 & 0 \end{pmatrix}. \quad (4.5)$$

In the left column of Figs. 4.7a-c, we plot the transient behavior of the three semi-axes and of the elongational viscosity for two elongation rates. For both elongation rates, we observe a monotonic increase of L and W and a monotonic decrease of B in Fig. 4.7a and 4.7b. This is contrary to the predictions of the MM Model, which predicts prolate droplet configurations in planar elongational flow (see Yu et al., 2002, Fig. 10). The transient elongational viscosity in Fig. 4.7c shows the same qualitative behavior as the

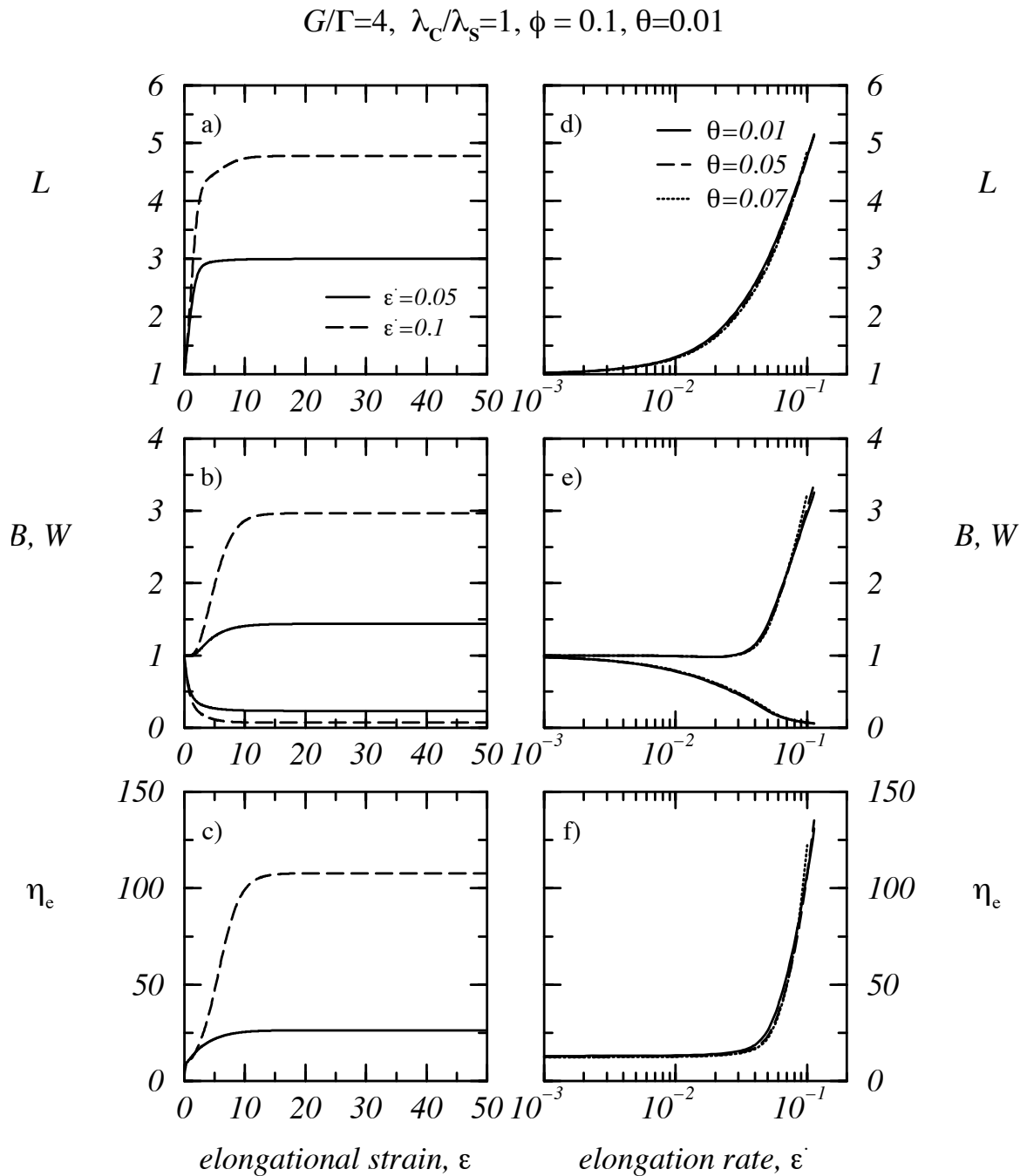


Figure 4.7.: The same as Fig. 4.6 for planar elongational flow: (a-c) The transient behavior of the droplet semiaxes and the elongational viscosity for two elongation rates $\dot{\varepsilon} = 0.05$ (solid lines), 0.1 (dashed lines), and $\theta = 0.01$. (d-f) The steady-state properties of the same quantities for three coupling parameter values, $\theta = 0.01$ (solid lines), 0.05 (dashed lines), 0.07 (dotted lines).

transient evolution of L and W , and it also increases monotonically. The steady-state morphological and viscometric properties of the emulsion are reported in Figs. 4.7d-f for several coupling parameter values. Whereas for uniaxial elongational flow (*cf.* Figs. 4.6d and e) we observe a stretching of the droplets into elongated, prolate ellipsoids, the situation is more complicated for planar elongational flow (Figs. 4.7d and e). In this flow field, the droplets are first stretched into prolates, and in this range of deformation rates the elongational viscosity remains almost constant. However, for higher values of the elongation rate, the droplets start to expand in the 3-direction deforming into an oblate state. The steady-state curves are insensitive with respect to a variation of θ between 0.01 and 0.07. The equations predict a strong strain hardening of the emulsion being subjected to planar hyperbolic flow. The beginning of the strain hardening regime (Fig. 4.7f) is observed in a rather narrow range of elongation rates, and it correlates with a sharp increase of the W -axis which is observed in the same elongation-rate interval (Fig. 4.7e). The major semiaxis, L , and the minor semiaxis, B , in Figs. 4.7d and 4.7e show a smooth increase and a smooth decay to zero, respectively. Therefore, in the present situation, the strain hardening in planar elongational flow is related to an expansion of the droplets into the 3-direction. Note that the strain hardening behavior recovered here is a feature which was not observed in the recent work of Yu et al. (2002), who evaluated the extra stress tensor for the MM model. Yu et al. (2002) report a constant elongational viscosity in uniaxial elongational flow and in planar elongational flow (see Yu et al., 2002, Eqs. (40), (44) and Figs. 8, 10). Viscometric properties of the ALS model in uniaxial elongational flow have not been reported thus far.

4.1.3. Four-Roll Mill Flow

We solve the time evolution equations for a deformation that is found at the stagnation point of the four roll mill

$$\nabla \mathbf{v} = \frac{1}{2}g \begin{pmatrix} 1 + \alpha & 1 - \alpha & 0 \\ -1 + \alpha & -1 - \alpha & 0 \\ 0 & 0 & 0 \end{pmatrix}, \quad (4.6)$$

where g is the strength of the deformation field, and $-1 < \alpha < 1$, is a measure of the relative strength of the straining motion and the vorticity in the flow. A purely rotational flow, a purely straining motion, and a simple shear flow are obtained with $\alpha = -1$, $+1$, and 0 , respectively.

In Fig. 4.8, we display the droplet semiaxes and the droplet orientation angle for two model emulsion with $Ca = 0.25$ (Fig. 4.8a) and $Ca = 4$ (Fig. 4.8b) for start-up of a four-roll mill flow. We chose $\alpha = 0.2$, *i.e.*, the magnitude of strain rate, $1 + \alpha$, over the magnitude of vorticity, $1 - \alpha$, is three halves. The $Ca = 0.25$ and the $Ca = 4$

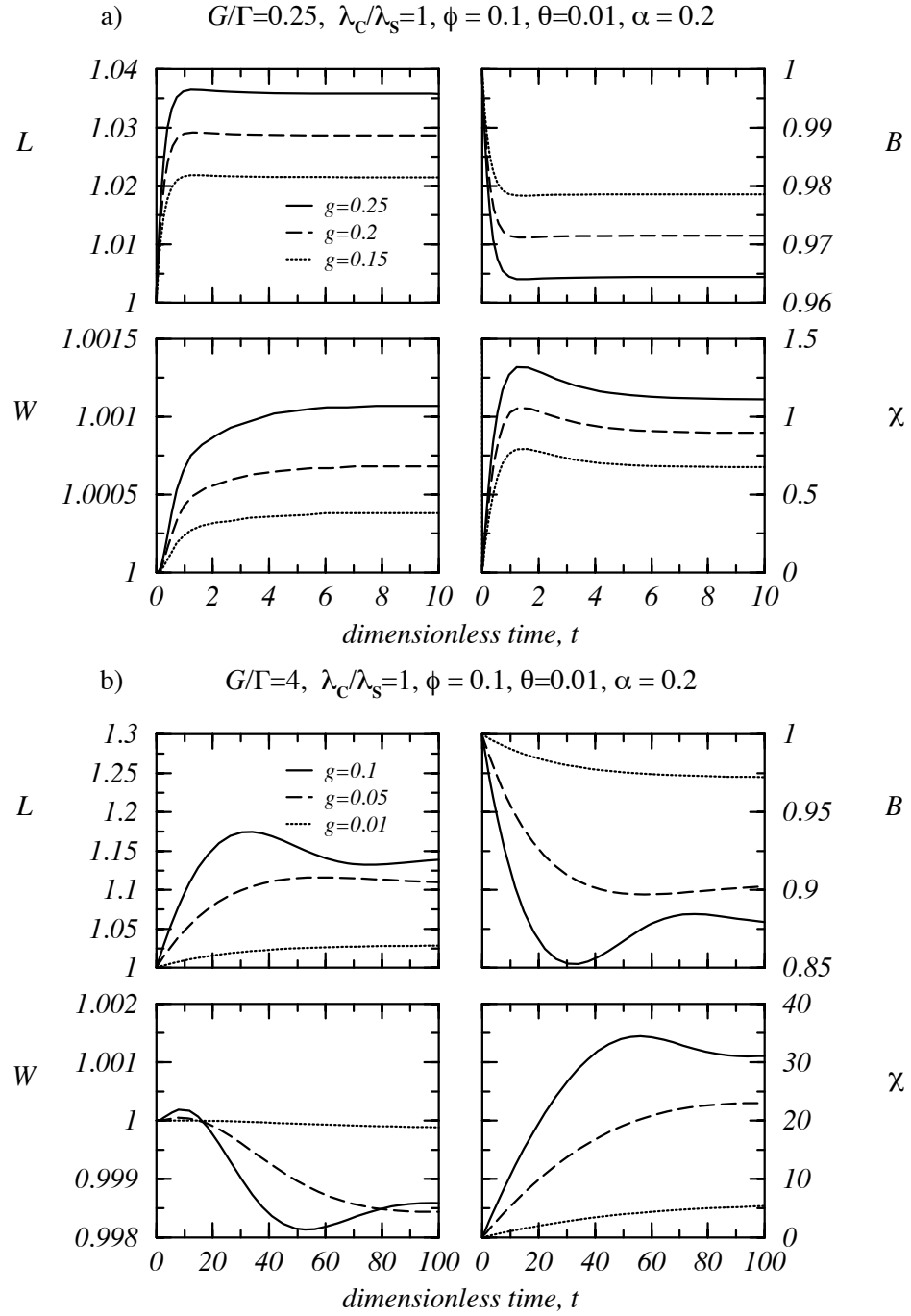


Figure 4.8.: The transient morphological properties for (a) a $Ca = 0.25$ and (b) a $Ca = 4$ model emulsion for start-up of a four-roll mill flow with $\alpha = 0.2$ and three values for the strength of the flow field, g . The droplet concentration and the coupling parameter are $\phi = 0.1$ and $\theta = 0.01$, respectively.

emulsion are investigated for high and low values of the the velocity gradient strength, g , respectively. We have chosen the same droplet concentration and coupling parameter value for both emulsions, and we have tracked the transient droplet morphology for three deformation velocities. For the $Ca = 0.25$ emulsion in Fig. 4.8a, we observe a monotonic behavior of the droplet semiaxes for small times and a steady state is obtained after a dimensionless time of approximately one decade. For this Capillary Number and the rather high values for g , oblate droplet configurations are generated in the four-roll mill. The orientation angle shows a non-linear increase with a pronounced overshoot. The qualitative behavior is different for the $Ca = 4$ model emulsion and the rather low values of g (Fig. 4.8b), where a non-monotonic approach with damped oscillations is observed for the transient behavior of the droplet morphology. A steady state is attained at long times. In general, such an oscillatory behavior of an internal variable is observed if a corotational derivative is employed for the time evolution equations of the structural variable. Here, the oscillations in the droplet shape tensor components are due to the non-linear coupling of the time evolution equations involving the structural variables. For $Ca = 4$, we observe a competition between oblate and prolate droplet shapes for small times immediately after start-up of flow. In the steady state, a prolate droplet configuration is recovered. The orientation angle shows an increase with dimensionless time.

We conclude this section by remarking that the emulsion model with matrix viscoelasticity predicts the typical rheological response of a viscoelastic fluid. The model is thus able to predict non-linear start-up effects in shear and elongational flows and a shear thinning behavior of the viscosity and the normal stress coefficients. The model can be solved also for mixed flows. A fit of the model to experimental data is thus possible and some preliminary fits are given in the Appendix. We proceed to study the model with break-up and coalescence next.

4.2. Model with Break-up and Coalescence

Now, the emulsion model with break-up and coalescence (3.18) is solved for homogeneous deformation velocities, $\nabla \mathbf{v}$. Again, a Runge-Kutta scheme with adaptive step size and a Newton-Raphson algorithm are used to solve for transient and steady state material properties, respectively. The model equations have been rendered dimensionless using $\tilde{t} = t/\sqrt[3]{\lambda_C \lambda_S \lambda_n}$, $\tilde{\mathbf{C}} = K/k_B T \mathbf{C}$, $\tilde{\mathbf{S}} = \mathbf{S}$, $\tilde{n} = n/n_0$, and $\tilde{\boldsymbol{\sigma}} = \boldsymbol{\sigma}/(\sqrt{G\Gamma})$. In all that follows, we omit the tilde over dimensionless quantities.

For the sample calculations in this section the phenomenological coefficient, p^* , is taken as the ratio of Newtonian viscosities of disperse and continuous phase according to

Eq. (3.7a). In particular we take $p^* = -0.25$ and $p^* = -1.25$ for our sample calculations. We compare model predictions with the predictions of the emulsion model of Sec. 3.1 in order to investigate the effect of a non-uniform DDF on the morphological properties and the rheological response of the emulsion.

4.2.1. Simple Shear Flow

Figure 4.9 shows the rheometric and the morphological properties as a function of shear rate, $\dot{\gamma}$, for two model emulsions with $p^* = -0.25$, $G/\Gamma = 4$ (solid lines) and $p^* = -1.25$, $G/\Gamma = 4$ (dashed lines), solving the full set of model equations (3.18) for steady shearing flow. The dispersed phase concentration is $\phi = 0.1$. The thin dotted lines in Fig. 4.9 are predictions for a constant droplet distribution and analogous material parameters. We have taken $\lambda_C \lambda_S / \lambda_n^2 = 1$ for the ratio of relaxation times of the emulsion, and a phenomenological coupling coefficient $\theta = 0.001$. Figures 4.9a-d show the non-linear rheometric properties as predicted from the system equations for steady shear flow. All viscometric functions possess a Newtonian plateau for low shear rates, a power-law regime for intermediate shear rates, and another Newtonian plateau in the high shear-rate regime (Figs. 4.9a-c). The ratio of the normal stress coefficients in Fig. 4.9d is non-trivial and decreases with increasing shear rate. The viscometric properties of the emulsions with variable and constant DDF are very similar for the present choice of model parameters.

Figures 4.9e-h show the deformation induced microstructural changes of the droplet morphology and the orientation of the micro-droplets with respect to the external flow field. The major droplet axis, L , increases and the minor droplet axis, B , decreases with increasing shear rate. For the low viscosity ratio emulsion, $p^* = -0.25$, we observe stronger variations in the major and in the minor droplet axes than for the $p^* = -1.25$ emulsion. The steady-state behavior of the vorticity axis of the droplet, W , is different for the two emulsions. Whereas a droplet widening effect, $W > 1$, is calculated for the low viscosity ratio, $p^* = -0.25$, a droplet compression effect, $W < 1$, is obtained for the high viscosity ratio, $p^* = -1.25$. The orientation angle, χ , decreases as a function of shear rate. From Figs. 4.9e-h we see that a variable DDF influences the steady-state morphological properties as obtained from the model equations, if we compare with the prediction for a constant DDF. This is especially true in the high shear-rate regime, $\dot{\gamma} \gtrsim 0.2$. Note that for very high shear rates, the viscometric and the morphological properties of the emulsion seem to approach constant plateau values. Finally, it should be mentioned that the continuum equations predict steady-state solutions for a wide shear-rate regime, extending from a low shear rate region with a lower Newtonian plateau to high shear rates with an upper Newtonian plateau.

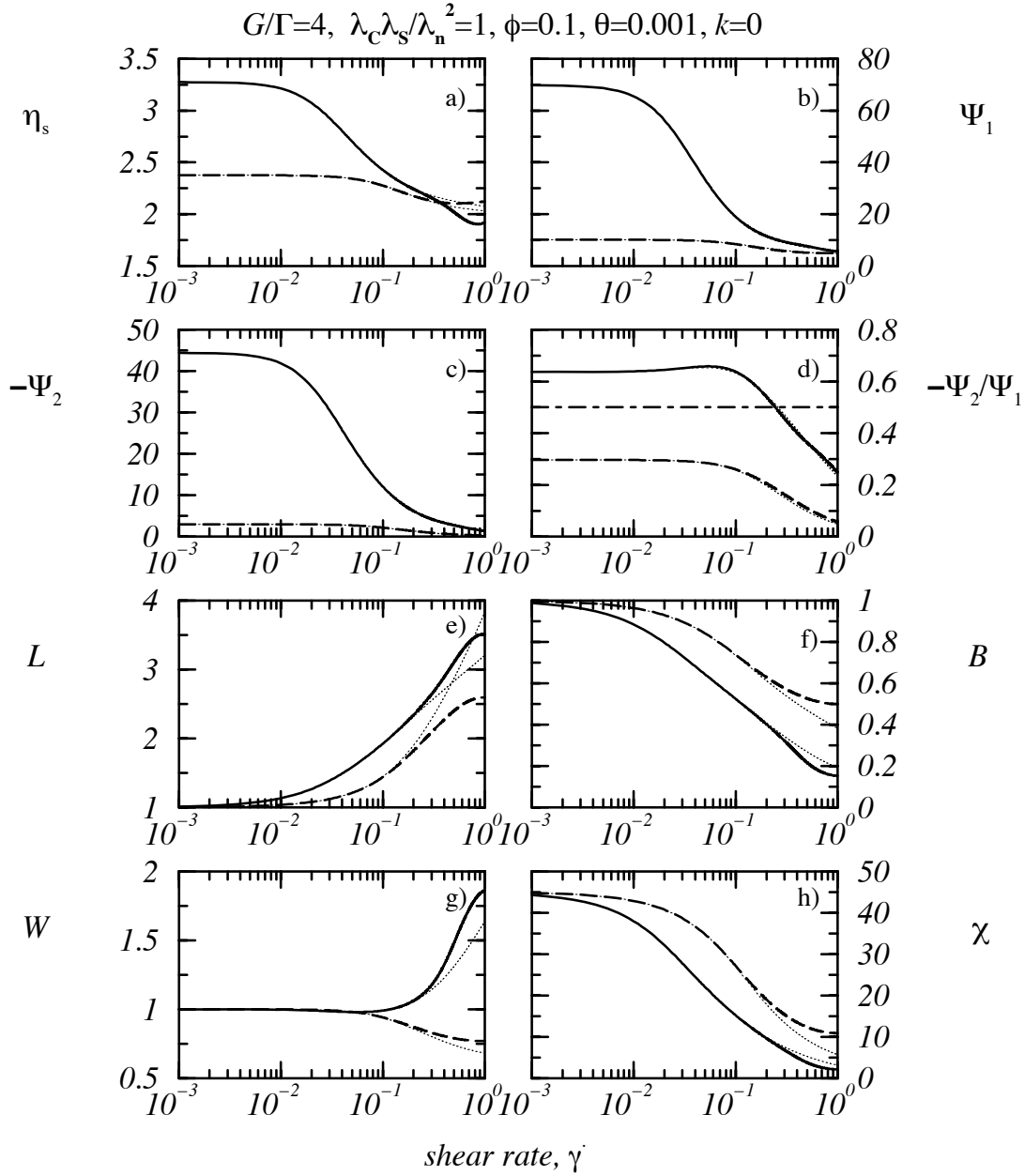


Figure 4.9.: Model predictions of the continuum equations for a variable DDF as functions of shear rate for two viscosity ratios, $p^* = -0.25$ (solid lines) and $p^* = -1.25$ (dashed lines). For the ratio of elastic moduli, the relaxation times, the coupling parameter, and the EWM power-law index, we chose $G/\Gamma = 4$, $\lambda_c \lambda_s / \lambda_n^2 = 1$, $\theta = 0.001$, and $k = 0$, respectively. Dispersed phase concentration is $\phi = 0.1$. The thin dotted lines are model predictions for a constant droplet distribution, i.e., $n = 1$. The graph on the front cover shows the non-linear flow curve and the major droplet axis for an extended regime of shear rates where a transition to the shear thickening regime is recovered. Here, we discuss only the regime of low and intermediate shear rates.

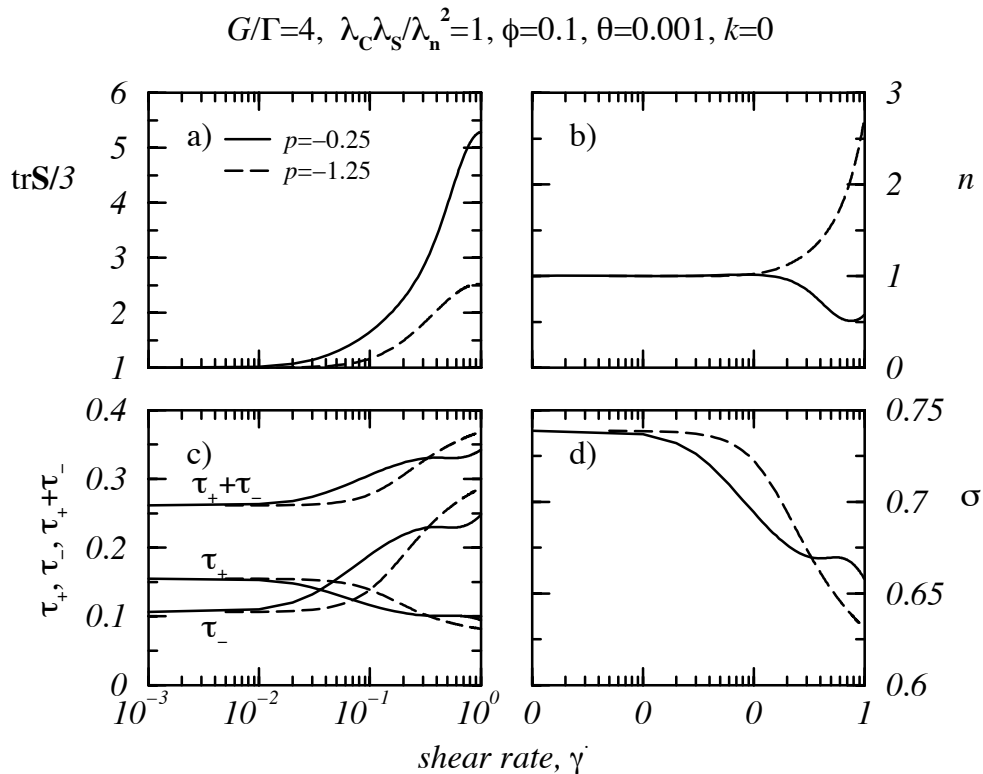


Figure 4.10.: The same as Fig. 4.9 for the properties of the steady DDF, $f(\text{tr}\mathbf{S}/3)$: a) position of the maximum, $\text{tr}\mathbf{S}/3$, b) maximum of the distribution function, n , c) volume fraction of residual droplets left and right from the inflection points R_{\pm} (τ_+ , τ_-) and total volume fraction of residual droplets ($\tau_+ + \tau_-$), d) volume fraction of the droplets around the maximum of the droplet distribution function, σ .

In Fig. 4.10, we examine the properties of the steady-state DDF for $p^* = -0.25$ (solid lines) and $p^* = -1.25$ (dashed lines) as functions of shear rate. We use the same model parameters as in Fig. 4.9. Figure 4.10a shows the average radius of the representative micro-droplets. This quantity increases for both viscosity ratios reported in Fig. 4.10 as the shear rate, $\dot{\gamma}$, is increased. For shear rates as high as $\dot{\gamma} \approx 0.8$, the increase in the average droplet radius becomes less pronounced and seems to reach a plateau value (*cf.* Fig. 4.9). The behavior of the average droplet radius shown in Fig. 4.10a corresponds to a shift of the location of the maximum of the DDF towards higher values of $\tilde{R} \equiv \text{tr}\mathbf{S}/3$ as the shear rate, $\dot{\gamma}$, is increased (*cf.* Fig. 4.11).

Figure 4.10b shows the solution of the droplet number density equation, Eq. (3.18d), for steady shear flow. We note that the representative number density of micro-droplets decreases for the $p^* = -0.25$ emulsion, whereas it increases for the $p^* = -1.25$ emulsion with increasing shear rate, $\dot{\gamma}$. This means that the steady-shear DDF is smeared out for

$p^* = -0.25$ (cf. Fig. 4.11a), and it is compressed for $p^* = -1.25$ (cf. Fig. 4.11b). Hence our model equations predict a shear-induced droplet coalescence in the low viscosity regime, and a shear-induced droplet break-up in the higher viscosity ratio regime.

In Fig. 4.10c, d, we show several characteristic droplet volume fractions, τ_- , τ_+ , σ , which are calculated from the DDF:

$$\tau_- = \frac{1}{V} \int_0^{R_-} f(R) dR, \quad \sigma = \frac{1}{V} \int_{R_-}^{R_+} f(R) dR, \quad \tau_+ = \frac{1}{V} \int_{R_+}^{\infty} f(R) dR, \quad (4.7)$$

where $f(R)$ is the DDF, Eq. (3.11), and

$$R_{\pm} = \tilde{R}^q \sqrt{\frac{3}{2} \pm \sqrt{\frac{5q-1}{q-1}}}, \quad (4.8)$$

are the inflection points of the DDF with $q > 1$. The first integral in the above Eq. (4.7), τ_- , represents the volume fraction of micro-droplets with droplet radii smaller than R_- , whereas the last integral, τ_+ corresponds to the volume fraction of droplets with radii larger than R_+ . The second integral, σ , is the number density of droplets with radii between R_- and R_+ , and it is a measure of the width of the center part of the DDF, i.e., the volume fraction of droplets that are found around its maximum at \tilde{R} . Consequently, $\tau_- + \tau_+$ might be considered as the total volume fraction of small, residual droplets (e.g., daughter or satellite droplets). Fig. 4.10c shows that τ_- increases as a function of shear rate, whereas τ_+ decreases with increasing shear rate. This means that the left edge of the DDF is smeared out as the shear rate is increased, whereas the right edge is compressed and becomes steeper as the shear rate increases (cf. Fig. 4.11a,b). The total volume fraction of residual droplets, $\tau_- + \tau_+$, is not a constant, but it increases with increasing shear rate. This is mainly due to a decrease of the third integral, σ , which is found to decrease for the low viscosity ratio emulsion, $p^* = -0.25$, as well as for the higher viscosity ratio emulsion, $p^* = -1.25$ (Fig. 4.10d).

In Fig. 4.11, we display a band of steady-state DDFs for $p^* = -0.25$ (Fig. 4.11a) and $p^* = -1.25$ (Fig. 4.11b), which have been discussed in Fig. 4.10. In Fig. 4.11, the shear rate is a parameter, $0 \leq \dot{\gamma} \leq 0.3$. The dotted lines in Fig. 4.11 are the trajectories of the maximum of the DDF with $\dot{\gamma}$ as a parameter, whereas the vertical dashed lines denote the maximum of the equilibrium DDF, $\dot{\gamma} = 0$. The set of model parameters is the same as in Figs. 4.9 and 4.10. We see clearly in Fig. 4.11 that the left edges of the DDF are smeared out for increasing shear rate, $\dot{\gamma}$, whereas the right edges become steeper as the shear rate is increased, although we have a qualitatively different behavior for the representative number density of droplets, n (cf. Fig. 4.10b, c). The insets in Fig. 4.11 show the DDF for $\dot{\gamma} = 0.3$ (solid lines) together with the equilibrium DDF (dashed lines), which have been shifted onto the DDF for $\dot{\gamma} = 0.3$. The vertical dotted lines in the two

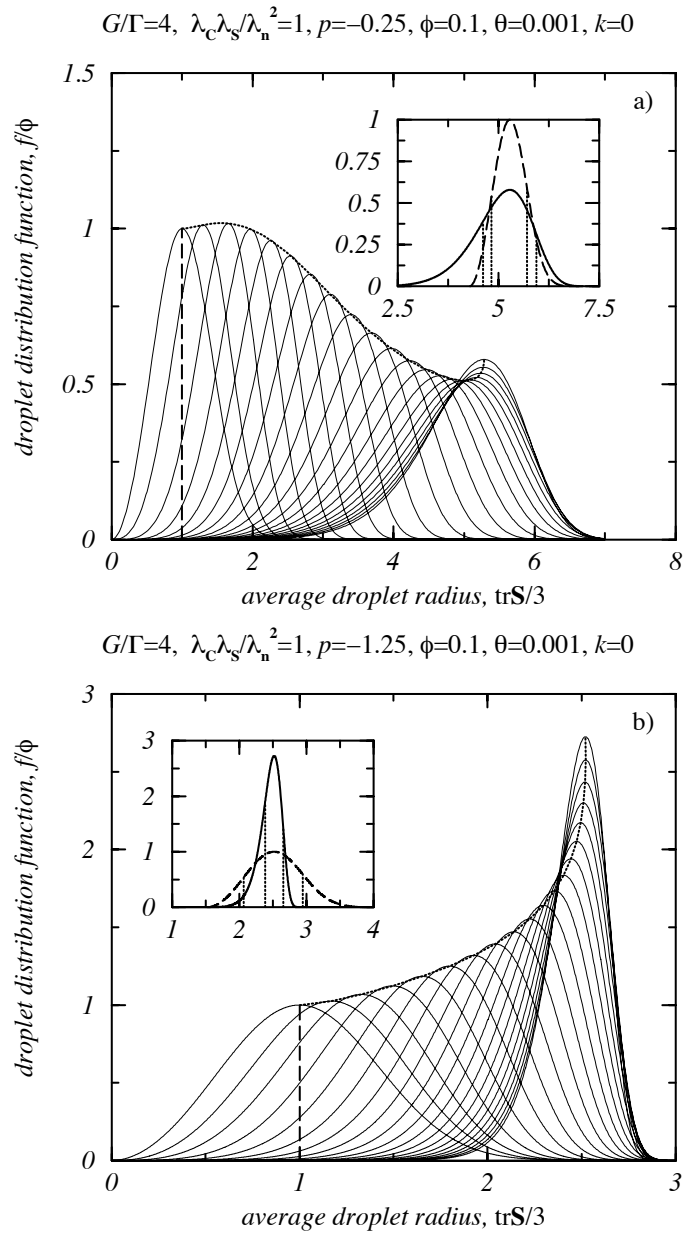


Figure 4.11.: The DDF for steady shearing flow and two viscosity ratios a) $p^* = -0.25$, b) $p^* = -1.25$, with the shear rate as a parameter ($0 \leq \dot{\gamma} \leq 0.3$). The dotted line is the trajectory of the maximum of the DDF in the $\text{tr}\mathbf{S}/3-f/\phi$ plane, with $\dot{\gamma}$ as a parameter, and the vertical dashed line marks the maximum of the equilibrium DDF for $\dot{\gamma} = 0$. The inset shows the equilibrium DDF (dashed line), which has been superimposed onto the DDF for the highest shear rate (solid line). Vertical dotted lines mark the position of the inflection points of the two DDFs, R_{\pm} .

insets denote the positions of the inflection points of the two DDFs, R_{\pm} . Note that the position of the inflection points separate from each other for the $p^* = -0.25$ emulsion (Fig. 4.11a), whereas they approach each other for the $p^* = -1.25$ emulsion (Fig. 4.11b). However, the volume fraction of droplets between the two inflection points, σ , decreases with respect to the equilibrium DDF for both viscosity ratios (*cf.* Fig. 4.10d). Although the DDF in Fig. 4.11b is compressed, the volume fraction of residual droplets, $\tau_+ + \tau_-$ increases. If dispersity of the system is defined as the distance between the inflection points of the DDF then we see that the degree of dispersity increases for the emulsion in Fig. 4.11a and it decreases for the emulsion in Fig. 4.11b.

In Figs. 4.12-4.14, we show sample calculations for start-up of steady shearing flow for a $p^* = -0.25$, $G/\Gamma = 4$ emulsion with $\phi = 0.1$ dispersed phase concentration, $\lambda_C \lambda_S / \lambda_n^2 = 1$, $\theta = 0.001$, and $k = 0$. Fig. 4.12 shows the transient behavior of the model as a function of shear strain, γ , for start-up of steady flow with three different shear rates, $\dot{\gamma} = 0.2$ (solid lines), 0.4 (dashed lines), and 0.8 (dotted lines).

Figures 4.12a,b display the transient shear stress, σ_{12} , and the transient shear viscosity, $\eta_s = \sigma_{12}/\dot{\gamma}$, respectively. The shear stress shows a rapid, monotonic increase for small shear strains and a subsequent overshoot before the steady state is attained. The steady shear stress increases with increasing shear rate. The transient shear viscosity in Fig. 4.12b shows the same qualitative behavior as the shear stress; *i.e.*, a rapid increase, an overshoot, and an approach towards its steady state as the shear strain increases during the start-up experiment. In Figs. 4.12c, d, the two normal stress differences are displayed. Note that the first normal stress difference, N_1 , is larger than the shear stress, whereas the second normal stress difference, N_2 , is nearly equal to the shear stress. The morphological characteristics of our model equations are shown in Figs. 4.12e-h. The transient behavior of the major droplet axis, L , correlates with the transient stresses; *i.e.*, a steep increase is observed for small strains, which is followed by an overshoot and an approach to the steady state. The minor droplet axis, B , shows an undershoot for the small shear rate, $\dot{\gamma} = 0.2$ (solid line), and a monotonic decrease for the high shear rate, $\dot{\gamma} = 0.8$ (dotted line). For $\dot{\gamma} = 0.2$, the vorticity axis of the droplets, W , shows a transition from an oblate configuration for small strains to a prolate configuration for higher shear strains (solid line in Fig. 4.12g). For the other two shear rates, the droplet configuration is oblate for all shear strains (broken lines in Fig. 4.12g). In Fig. 4.12h, the transient orientation angle of the droplet with respect to the external flow field is shown. For the smallest shear rate (solid line), an undershoot in the orientation angle is obtained. From Figs. 4.12e-h, we see that transient droplet deformation and orientation become more pronounced as the shear rate is increased (*cf.* Fig. 4.9e-h). The thin dotted lines in Fig. 4.12 are predictions for the emulsion with a constant DDF, *i.e.*, $n = 1$.

In Fig. 4.13, we examine properties of the transient DDF as functions of shear strain for the same model parameters as in Fig. 4.12. Figure 4.13a shows the transient behavior

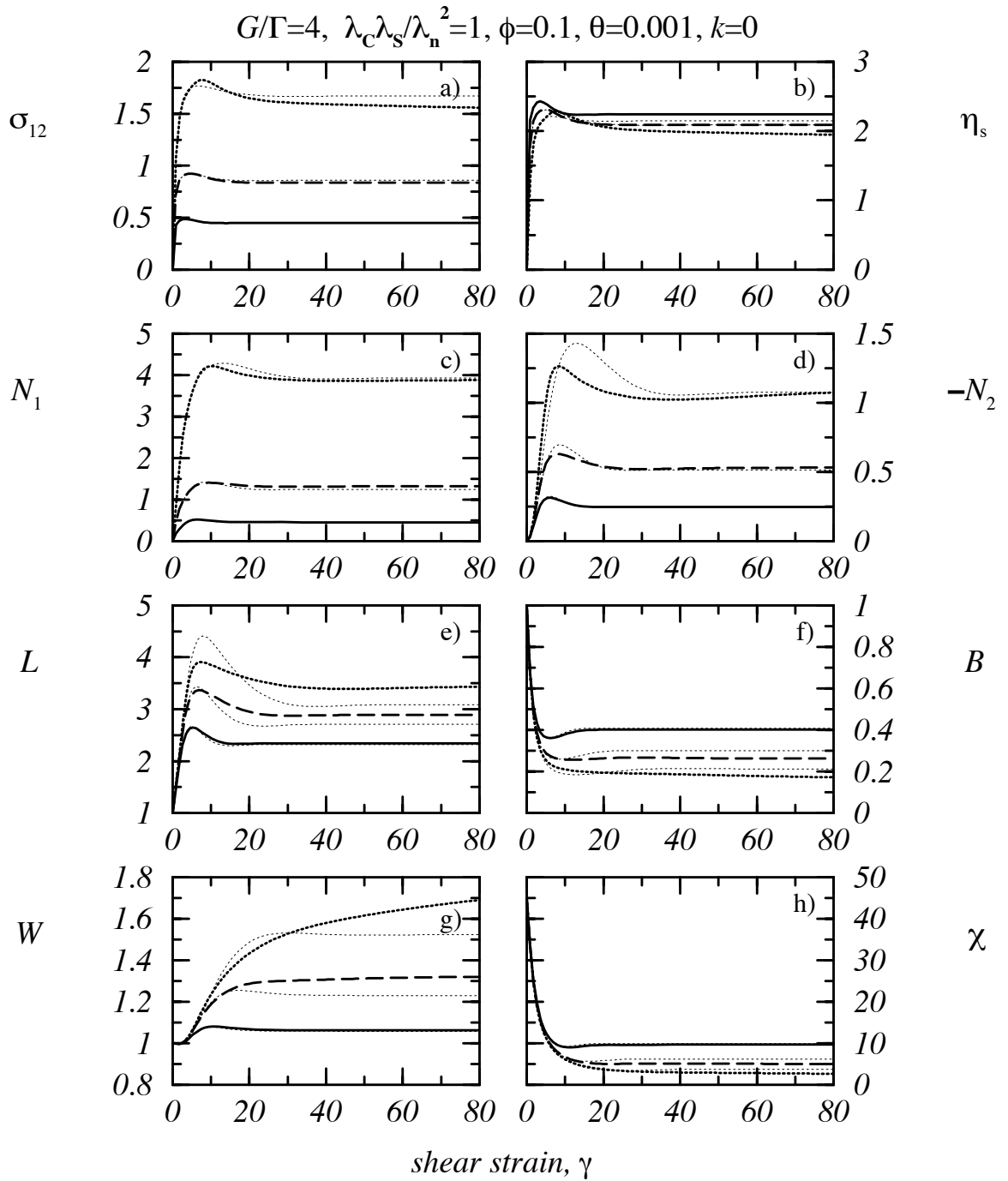


Figure 4.12.: The same as Fig. 4.9 for start-up of steady shearing flow for a $p^* = -0.25$ emulsion and three different shear rates, $\dot{\gamma} = 0.2$ (solid lines), 0.4 (dashed lines), 0.8 (dotted lines). The thin dotted lines are model predictions for a constant DDF.

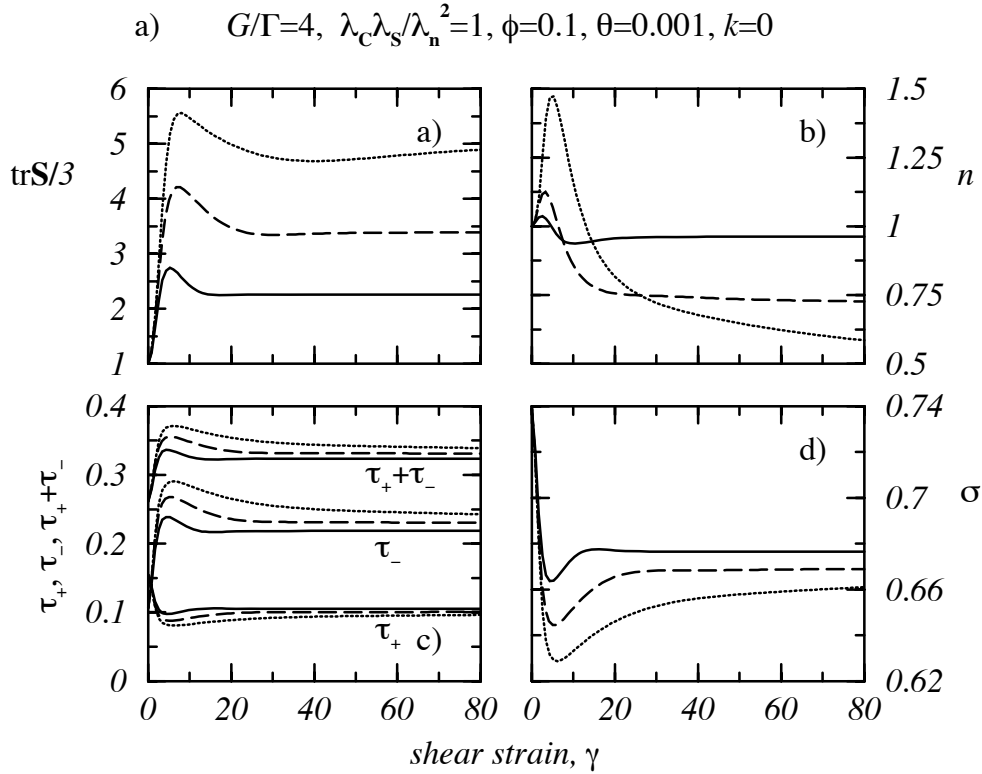


Figure 4.13.: The same as Fig. 4.10 for the function properties of the transient DDF for $p^* = -0.25$ and three different shear rates, $\dot{\gamma} = 0.2$ (solid lines), 0.4 (dashed lines), 0.8 (dotted lines). Other model parameters are as in Fig. 4.12.

of the representative average droplet radius of the micro-droplets. This quantity shows a pronounced overshoot and reaches a steady state for $\gamma \approx 40$ shear strain units. The solution of the droplet number density equation, Eq. (3.18d), is reported in Fig. 4.13b. We recover an increase of the representative number density of droplets immediately after start-up of flow of approximately 10-50%, which is followed by a rapid decrease of this quantity towards the steady-state value. This value is $n \approx 0.9$ for the lowest shear rate ($\dot{\gamma} = 0.2$, solid line), and of $n \gtrsim 0.5$ for the highest shear rate ($\dot{\gamma} = 0.8$, dotted line). This means that for start-up of steady shear flow, a transition from a break-up to a coalescence regime is obtained with the model. The volume fractions of residual droplets, τ_+ , τ_- , and $\tau_+ + \tau_-$ are shown in Fig. 4.13c. Note that these volume fractions also show a strongly non-linear behavior with an overshoot (for τ_- and $\tau_+ + \tau_-$) or an undershoot (for τ_+). Whereas the small droplet radius regime, τ_- , is smeared out for increasing shear strains, the large droplet radius regime, represented by τ_+ , is compressed as the shear strain increases. The total volume fraction of residual droplets, $\tau_+ + \tau_-$, is approximately 25% for $\gamma = 0$, and reaches a value of approximately 33% at the steady state. Figure 4.13d, displays the volume fraction of droplets with radii between the inflection points,

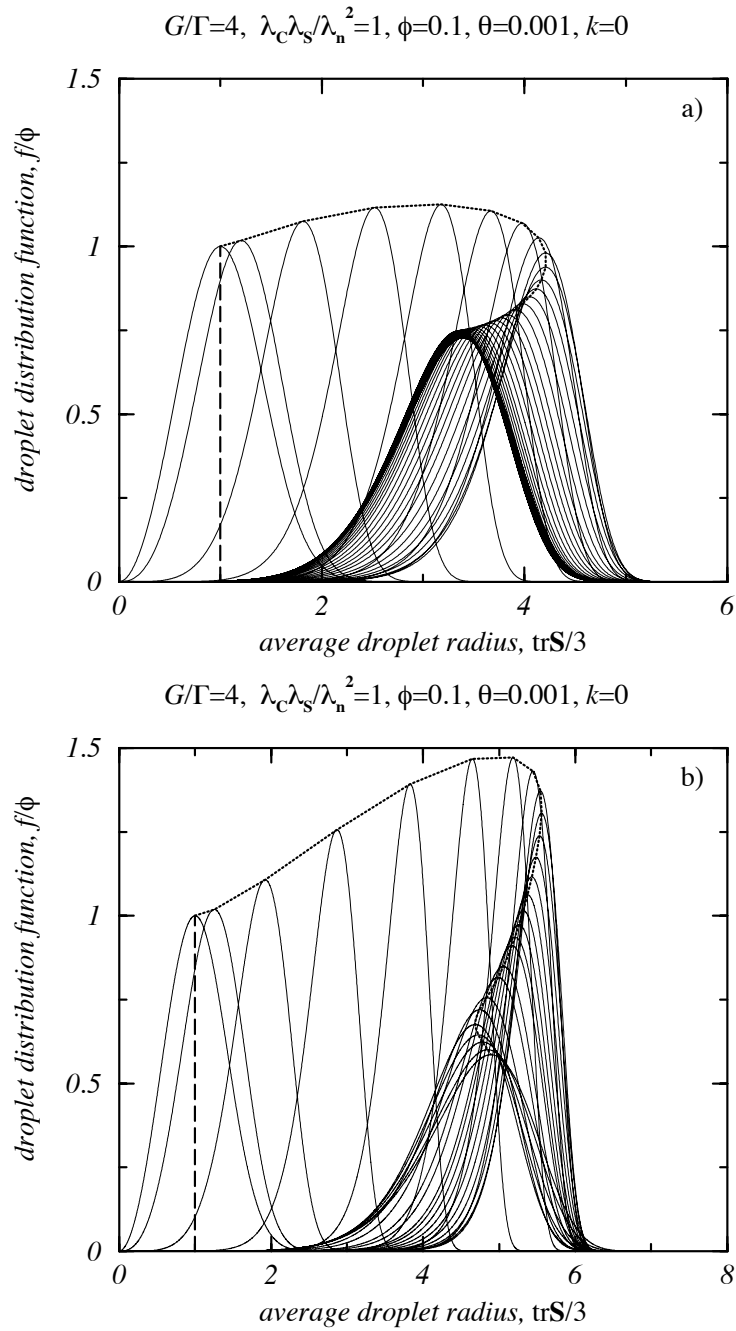


Figure 4.14.: The same as Fig. 4.11 for the transient DDF with shear strain as a parameter ($0 \leq \gamma \leq 80$) and two shear rates: a) $\dot{\gamma} = 0.4$, b) $\dot{\gamma} = 0.8$. The dotted line is the trajectory of the maximum of the DDF in the $\text{tr}\mathbf{S}/3-f/\phi$ plane, and the vertical dashed line denotes the equilibrium DDF for $\gamma = 0$.

σ . This volume fraction decreases rapidly for small shear strains, shows an undershoot at $\gamma \approx 7$, and reaches a steady-state value for $\gamma \gtrsim 40$. The volume fraction of droplets with radii between the two inflection points of the DDF is approximately 75% at equilibrium, and decreases to approximately 67% at the steady state. From Figs. 4.13c, d, we deduce that the volume fraction σ is reduced and the total volume fraction of residual droplets, $\tau_+ + \tau_-$, is increased for start-up of steady shearing flow.

Figure 4.14 shows two bands of transient DDFs for the same set of model parameters as in Figs. 4.12, 4.13. The shear rates are $\dot{\gamma} = 0.4$ (Fig. 4.14a), $\dot{\gamma} = 0.8$ (Fig. 4.14b) and the dimensionless strain, $0 \leq \gamma \leq 80$, has been taken as a parameter. Again, the vertical dashed lines mark the position and the height of the equilibrium DDF, whereas the dotted lines are the trajectories of the maximum of the DDF in the $\text{tr}\mathbf{S}/3 - f/\phi$ plane. It can be seen from Fig. 4.14 that both the location of the maximum (the representative average droplet radius) and the height of the DDF (the number density of droplets with the representative average droplet radius) increase for low shear strains and then decrease as the shear strain increases (*cf.* Fig. 4.13a, b). This effect is more pronounced in Fig. 4.14b for the shear rate, $\dot{\gamma} = 0.8$. Furthermore, we see clearly in Fig. 4.14 that the left edge of the DDF is smeared out, whereas the right edge becomes steeper as the shear strain increases.

4.2.2. Elongational Flow

Figures 4.15-4.17 summarize model predictions for uniaxial elongational flow. We have taken the same model parameters as before, *i.e.*, $G/\Gamma = 4$, $\phi = 0.1$, $\lambda_C \lambda_S / \lambda_n^2 = 1$, $\theta = 0.001$, and a vanishing EWM power-law index, $k = 0$. Again, we have studied two different viscosity ratios, $p^* = -0.25$ and $p^* = -1.25$.

Figure 4.15 shows morphological and viscometric data obtained from the continuum model. In the left column (Figs. 4.15a-c), we show the start-up behavior of the model for $p^* = -0.25$ and three different elongation rates, $\dot{\epsilon} = 0.05$ (solid lines), 0.1 (dashed lines), and 0.2 (dotted lines). For low elongation rates, the droplet semiaxes in Fig. 4.15a, b show a monotonic increase and reach a steady state for $\epsilon \approx 4$. For the highest elongation rate, $\dot{\epsilon} = 0.2$, a slight overshoot/undershoot is detected in the transient droplet semiaxes. The transient elongational viscosity, η_e , in Fig. 4.15c increases monotonically for $\dot{\epsilon} = 0.05$ (solid line) and shows a strongly non-linear behavior for $\dot{\epsilon} = 0.1$ and 0.2 (broken lines). In the right column (Figs. 4.15d-f), we display the steady-state morphological and viscometric data as calculated from the model for two viscosity ratios, $p^* = -0.25$ (solid lines) and $p^* = -1.25$ (dashed lines). For elongation rates $\dot{\epsilon} \gtrsim 0.2$, we observe an increase of the major droplet axis, L , and a decrease of the minor droplet axis, B , (Fig. 4.15d, e). For the low viscosity ratio emulsion, a strain-hardening behavior is

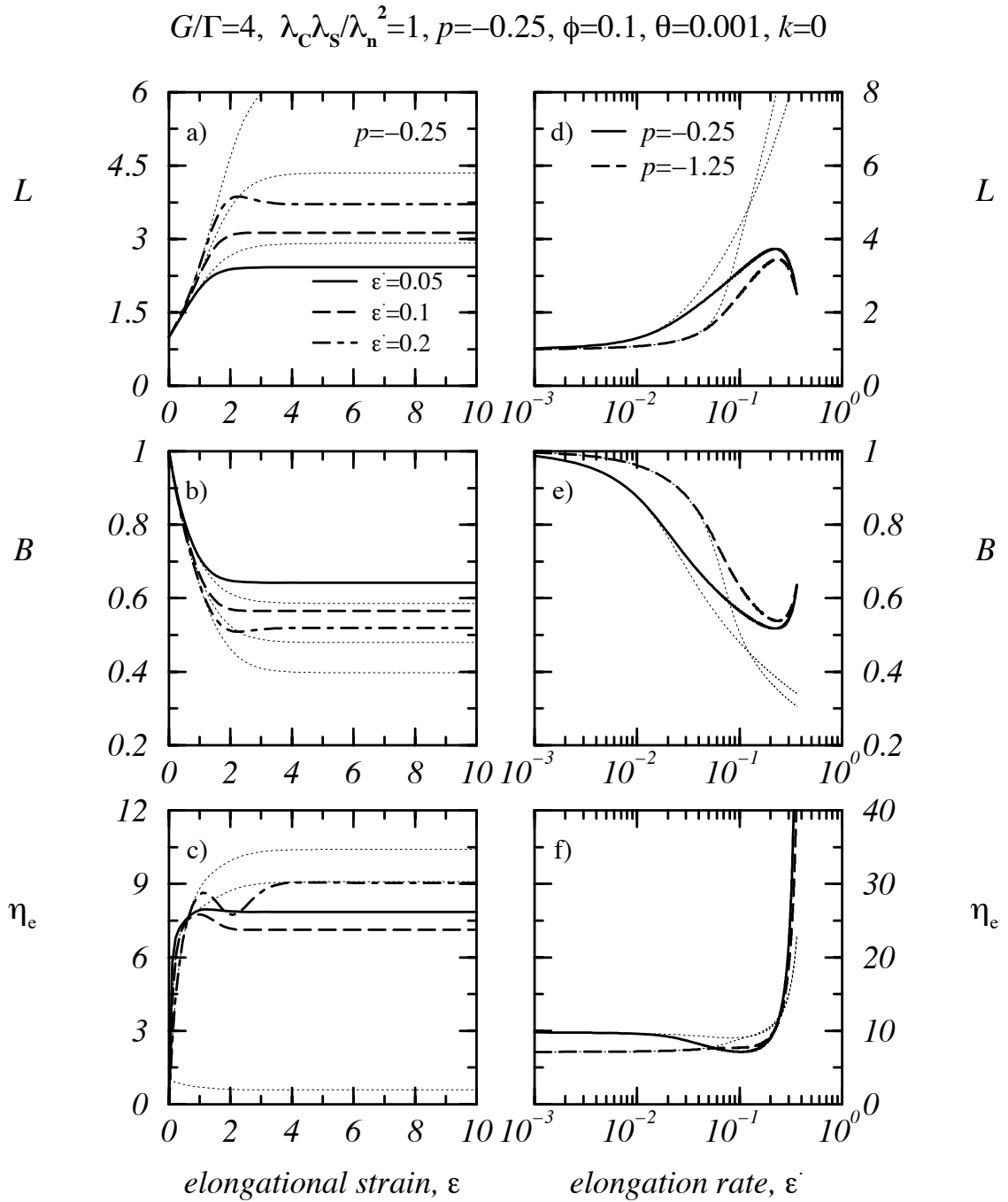


Figure 4.15.: Model solution for uniaxial elongational flow for various elongation rates and viscosity ratios: a)-c) transient calculations for $p^* = -0.25$ and three different elongation rates, d)-f) steady-state calculations for $p^* = 0.25$ (solid lines) and $p^* = -1.25$ (dashed lines). The other model parameters are the same as in Fig. 4.9. Thin lines are predictions for a constant DDF.

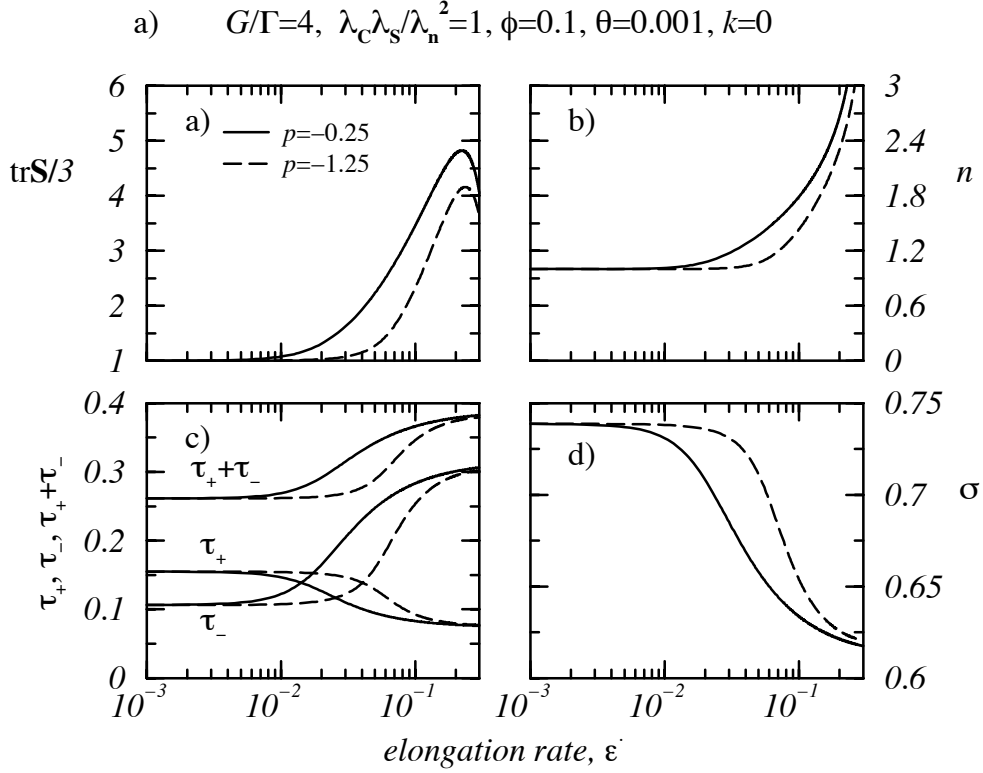


Figure 4.16.: The properties of the steady-state DDF for two different viscosity ratios, $p^* = -0.25$ (solid lines) and $p^* = -1.25$ (dashed lines), for steady uniaxial elongational flow. Other model parameters are the same as in Fig. 4.15.

recovered for $\dot{\epsilon} \lesssim 0.1$, whereas the high viscosity ratio emulsion shows only a slight strain hardening (Fig. 4.15f). For $\dot{\epsilon} \gtrsim 0.2$, the elongational viscosity becomes very large. The thin dotted lines in Fig. 4.15 are predictions of a constant DDF.

In Fig. 4.16, we display the properties of the steady DDF for uniaxial elongational flow as a function of elongation rate, $\dot{\epsilon}$, for two different viscosity ratios $p^* = -0.25$ (solid lines) and $p^* = -1.25$ (dashed lines). The other model parameters are as in Fig. 4.15. Figure 4.16a shows that the steady DDF for uniaxial elongational flow is shifted towards higher droplet radii, $\text{tr}\mathbf{S}/3$, for $\dot{\epsilon} \lesssim 0.1$. Furthermore, the height of $f(R)$ increases as the elongation rate is increased (Fig. 4.16b). This means that the DDF is shifted to the right and it is compressed as the elongation rate increases (*cf.* Fig. 4.17). Figure 4.16c shows that the volume fraction of droplets with radii smaller than R_- (τ_-) increases with increasing elongation rate, whereas the volume fraction of droplets with radii greater than R_+ (τ_+) decreases. The total volume fraction of residual droplets, $\tau_+ + \tau_-$, varies between 26% and 37%, approximately, for $\dot{\epsilon} \lesssim 0.2$. Fig. 4.16d shows the volume fraction of droplets with radii between R_+ and R_- (σ). This quantity decreases as the elongation

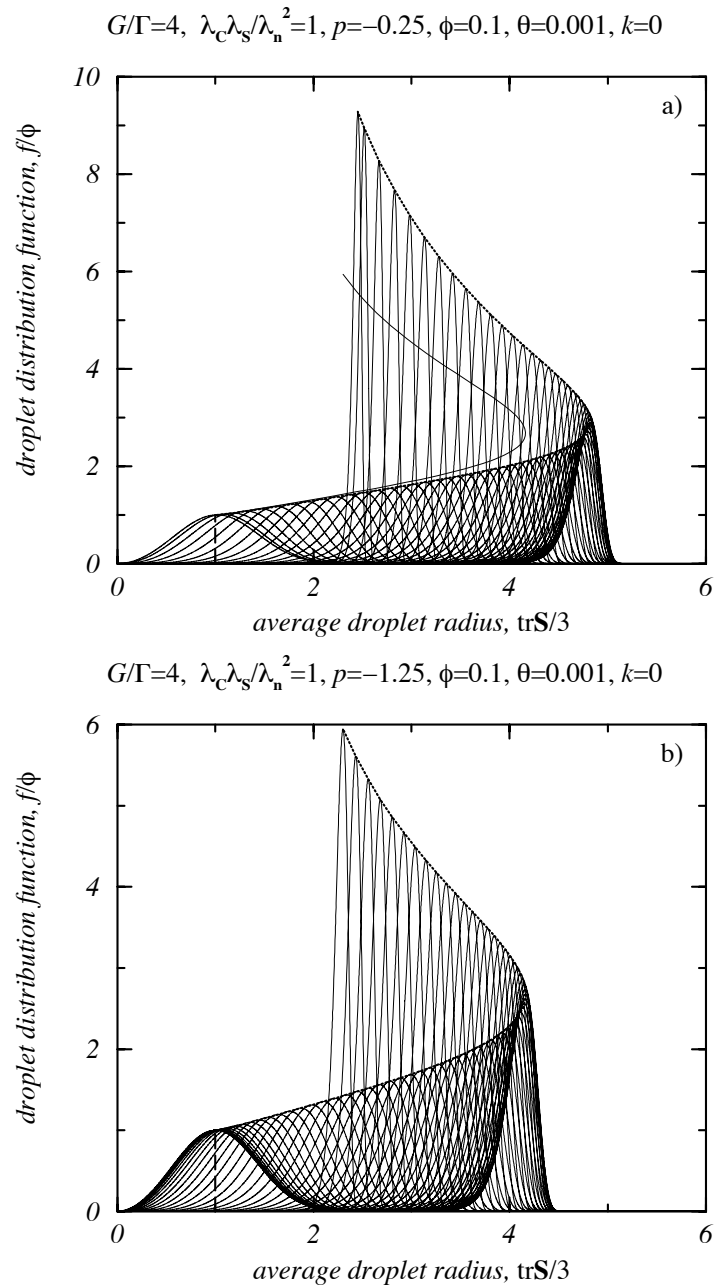


Figure 4.17.: The DDF for steady uniaxial elongational flow and two viscosity ratios, a) $p^* = -0.25$ and b) $p^* = -1.25$. The dotted lines are the trajectories of the maximum of the DDF in the $\text{tr}\mathbf{S}/3-f/\phi$ plane with $\dot{\epsilon}$ as a parameter ($0 \leq \dot{\epsilon} \leq 0.3$). The vertical dashed lines mark the maximum of the equilibrium DDF. In Fig. 4.17a we have included the trajectory for $p^* = -1.25$ (solid line).

rate is increased, and varies between 74% and 63%, approximately. Note that the results of Fig. 4.16c, d are qualitatively similar to the results obtained for steady shearing flow (*cf.* Fig. 4.10).

Figure 4.17 shows the steady-state DDF for uniaxial elongational flow for $p^* = -0.25$ and $p^* = -1.25$, using the elongation rate as a parameter, $0 \leq \dot{\epsilon} \leq 0.3$. Again, the vertical dashed lines mark the equilibrium DDF, whereas the dotted lines are the trajectories of the maximum of the DDF. Note that the DDF is compressed and becomes as high as $n \approx 10$ for $\dot{\epsilon} = 0.3$ and $p^* = -0.25$, *i.e.*, we observe an elongational flow-induced break-up. Recently, the phenomenon of flow induced coalescence in extensional flow has been investigated in Fortelný and Zivný (2003). The volume fraction of droplets between the inflection points of the DDF becomes smaller and the volume fraction of drops outside the center part of the DDF increases as the elongation rate increases (*cf.* Fig. 4.16c, d). We see that for both viscosity ratios the dispersity of the system decreases because the distance of the inflection points of the DDF becomes smaller. On an absolute basis, the dispersity decreases as the width of the distribution gets narrower.

Grizzuti and Bifulco (1997) studied the effect of coalescence and break-up on the steady-state morphology of immiscible polymer blends in shear flow. In their experimental studies, coalescence and break-up phenomena prevail over the effects of droplet deformation. It might be interesting to find out whether our model can be applied to fit those data.

5. Simple Laminar Flows

An important application of the emulsion models is the simulation of flow in geometries of practical importance. Simple emulsion flows are realized in channels, tubes, and in the annular gap. This chapter gives an introduction to CFD of highly viscous emulsions with main emphasis on the computation of flow profiles and microstructural emulsion characteristics. The dispersing characteristics of the flows are discussed in connection with the rheometer flows of the previous chapter and in connection with their dispersing characteristics.

5.1. Channel and Tube Flow

For pure Poiseuille flow between two horizontal planes located at $x_2 = \pm H/2$ the blend model of Sec. 3.2 is solved for steady laminar flow in the x_1 direction. For this type of flow the model equations (3.18) are rendered dimensionless with $\tilde{\mathbf{v}} = \sqrt[3]{\lambda_C \lambda_C \lambda_n} \mathbf{v}/H$, $\tilde{\mathbf{C}} = K\mathbf{C}/k_B T$, $\tilde{\mathbf{S}} = \mathbf{S}$, $\tilde{n} = n/n_0$, $\tilde{p} = p/\sqrt{G\Gamma}$, $\tilde{\boldsymbol{\sigma}} = \boldsymbol{\sigma}/\sqrt{G\Gamma}$, and $\tilde{\mathbf{r}} = \mathbf{r}/H$, $\tilde{\boldsymbol{\nabla}} = H \boldsymbol{\nabla}$. In what follows we skip the tilde over dimensionless quantities. The velocity vector is of the form $\mathbf{v} = v_1(x_2) \mathbf{e}_1$ and obeys the boundary conditions

$$v_1'(x_2 = 0) = 0, \quad (5.1a)$$

$$v_1(x_2 = 1/2) = 0, \quad (5.1b)$$

where “ ’ ” denotes differentiation with respect to the transversal direction, x_2 . The flow is symmetric with respect to the midplane, $x_2 = 0$ and the density, ρ , is constant since $\boldsymbol{\nabla} \cdot \mathbf{v} = 0$. The conformation tensor, the droplet shape tensor, the number density of droplets, and the extra stress tensor are functions of the transversal coordinate, x_2 .

For this type of flow the set of PDE's (3.18) reduces to a set of ODE's since flow is stationary and the fields depend only on one spatial coordinate. The set of ODE's can be rewritten in the form

$$\mathcal{A} \cdot \boldsymbol{\xi}' = \mathbf{b}, \quad (5.2)$$

which has to be solved for the boundary conditions (5.1). In Eq. (5.2) $\boldsymbol{\xi}$ is a 12-tuple of non-trivial physical fields, \mathcal{A} is a 12×12 coefficient matrix, \mathbf{b} is another 12-tuple called the “inhomogeneity,” and “ $'$ ” denotes differentiation with respect to the x_2 coordinate. The coefficient matrix, \mathcal{A} , and the inhomogeneity, \mathbf{b} , are obtained from the continuum equations (3.18). For laminar channel flow, we have

$$\boldsymbol{\xi} = (v_1, v_1', p, \text{vec}(\mathbf{C}), \text{vec}(\mathbf{S}), n)^T, \quad (5.3)$$

where $v_1' = \partial v_1 / \partial x_2$ is the velocity gradient, and $\text{vec}(\mathbf{X}) = (X_{11}, X_{12}, X_{22}, X_{33})$, $\mathbf{X} \in \{\mathbf{C}, \mathbf{S}\}$, denotes the non-trivial components of the microstructural variables, \mathbf{C} and \mathbf{S} . Equation (5.2) together with Eqs. (5.1) defines a Two Point Boundary Value (TPBV) problem which is solved numerically.

The coefficient matrix, \mathcal{A} , and the inhomogeneity, \mathbf{b} are obtained in the following way from Eqs. (3.18). The first two rows of $(\mathcal{A}, \mathbf{b})$ corresponding to v_1 and v_1' are the 1-component of Eq. (3.18a) and the 12-component of Eq. (3.18b), respectively. The third row of $(\mathcal{A}, \mathbf{b})$ corresponds to the v_2 -component of the momentum balance equation (3.18a). Note that the constitutive relation for the extra stress tensor (3.18e) is to be used in the Cauchy momentum balance (3.18a) for appropriate identification of the first and the third row of $(\mathcal{A}, \mathbf{b})$. The remaining nine rows of $(\mathcal{A}, \mathbf{b})$ corresponding to the non-trivial components of the conformation tensor, the droplet shape tensor, and the number density of droplets, are identified by taking the derivative with respect to x_2 of the appropriate components of Eqs. (3.18b-3.18c) and of the number density equation (3.18d).

The TPBV problem for the emulsion is solved computationally using a shooting algorithm (Press et al., 1992). The algorithm uses a fourth-order Runge-Kutta scheme with adaptive step size to integrate the set of ODEs and a globally convergent Newton algorithm to match the no-slip boundary conditions at the upper wall, $x_2 = 1/2$. First, in our computer algorithm the linear system (5.2) is solved using an LU decomposition of the coefficient matrix, \mathcal{A} . The set of ODEs $\boldsymbol{\xi}' = \mathcal{A}^{-1} \cdot \mathbf{b}$ is then integrated with a Runge-Kutta algorithm shooting from the mid-plane, $x_2 = 0$, to the upper plane, $x_2 = 1/2$. Every Runge-Kutta shoot starts with equilibrium values of the microstructural variables and a different mid-plane velocity, $V = v_1(x_2 = 0)$, being the independent variable in the Newton subroutine of the shooting algorithm

$$\boldsymbol{\xi} = (V, 0, p_0, \text{vec}(1, 0, 1, 1), \text{vec}(1, 0, 1, 1), n_0)^T. \quad (5.4)$$

The last nine entries of the above 12-tuple are specified through the boundary condition (5.1a). The requirement of vanishing shear rate implies that the microstructure of the emulsion is in equilibrium on the mid-plane. For the starting value of the pressure, p_0 , an arbitrary value can be taken since it is not specified up to an additive constant. The Runge-Kutta integrations with the starting tuple (5.4) are repeated until the Newton

algorithm has converged, *i. e.* the non-slip condition Eq. (5.1b), is satisfied. This gives the non-trivial mid-plane velocity of the emulsion, V , the solution of the TPBV problem. A final Runge-Kutta integration with the solution of the TPBV problem is performed to obtain the flow profiles together with the profiles of the microstructural characteristics.

If the velocity field is not symmetric (*e. g.* for mixed Couette-Poiseuille flow) one has to integrate from the lower to the upper wall. In this case one has to shoot with different wall shear rates on the lower wall to match the no-slip boundary condition at the upper wall. Since the micro-structural characteristics of the emulsion are a function of shear rate, one has to solve the steady state-shear flow problem prior to every Runge-Kutta shoot. This procedure will be adopted for the solution of the annular flow problems in Sec. 5.2.

To describe the axial flow of the emulsion through a circular tube of radius R , Eqs. (3.18) are solved in cylindrical coordinates (r, ϕ, z) , where r is the distance from the cylinder axis, ϕ is the azimuthal coordinate, and z is the axial coordinate along the cylinder axis. The boundary conditions for the velocity field are

$$v'_z(r = 0) = 0, \quad (5.5a)$$

$$v_z(r = R) = 0, \quad (5.5b)$$

and the tube axis is a symmetry line for the velocity and microstructural profiles. Now the tube radius, R , is the characteristic length of the flow problem, *i. e.* $\tilde{\mathbf{r}} = \mathbf{r}/R$, $\tilde{\nabla} = R\nabla$. The set-up of the ODE's (5.2) is analogous as explained above, for the channel flow problem. The emulsion equations (3.18) are reformulated in terms of a TPBV problem for the boundary conditions (5.5) and the 12-tuples of unknown profiles is

$$\boldsymbol{\xi} = (p, v_z, v'_z, \text{vec}(\mathbf{C}), \text{vec}(\mathbf{S}), n)^T. \quad (5.6)$$

The “ ’ ” denotes differentiation with respect to the radial coordinate and $\text{vec}(\mathbf{X}) = (X_{rr}, X_{rz}, X_{\phi\phi}, X_{zz})$, $\mathbf{X} \in \{\mathbf{C}, \mathbf{S}\}$ denotes the non-trivial components of the microstructural variables, \mathbf{C} and \mathbf{S} . The coefficient matrix, \mathcal{A} , and the inhomogeneity, \mathbf{b} , are obtained in an analogous way as for the laminar channel flow problem. The first row of $(\mathcal{A}, \mathbf{b})$ corresponding to p is the r -component of the Cauchy momentum balance (3.18a) in cylindrical coordinates. The second and third row of $(\mathcal{A}, \mathbf{b})$ corresponding to v_z and v'_z are the z -component of the momentum balance and the rz -component of the conformation tensor equation (3.18b), respectively. The remaining nine rows of $(\mathcal{A}, \mathbf{b})$ are obtained as before by taking the derivative of the appropriate microstructural equations with respect to the radial coordinate, r . The flow problem is symmetric with respect to the tube axis and the velocity on the tube axis is the independent variable of the Newton subroutine in the shooting algorithm. It is varied until the boundary condition (5.5b) is matched.

The computer codes for the emulsion models of Sec. 3.1 and 3.2 have been checked carefully. We have solved viscoelastic fluid models for Polymer melts (Dressler and Edwards, 2005) to assess the performance of the shooting algorithm and we have compared numerical data with analytical solutions of the UCM Model (Dressler and Edwards, 2006) to further check the accuracy of the code.

5.1.1. Model with Matrix Viscoelasticity

We compute laminar channel flow profiles for the PIB/PDMS emulsion discussed in App. A assuming a constant DDF, *i. e.* $n = n_0$. Then, the emulsion model accounting for break-up and coalescence reduces to the model that assumes a constant DDF (Sec. 3.1) This is used as a consistency check of our computer codes.

Figure 5.1 shows channel flow profiles for the $\phi = 0.1$ PIB/PDMS emulsion and five pressure drops. Model parameters for this system have been introduced in App. A; Figs. A.2, A.3. Figures 5.1a and 5.1b display the velocity field and the shear rate as functions of the distance from the mid-plane. Figures 5.1c and 5.1d show the shear stress profile and the profile of the first normal stress difference, respectively. The velocity profile matches the boundary conditions on the mid-plane and the upper plate of the channel. Note that the first normal stress difference is much larger than the shear stress. Furthermore, high wall shear rates are obtained for the highest pressure drop in Fig. 5.1b. The profiles of the major and the minor droplet axes as functions of the transversal direction are shown in Figs. 5.1e and 5.1f. The variation of the major droplet axis is monotonic for the lowest pressure drops in Fig. 5.1e, but it becomes non-monotonic for higher pressure drops. This finding is consistent with Figs. 4.4b where the droplet semiaxes are non-monotonic functions of shear rate. The minor droplet axis decreases monotonically for all pressure drops shown in Fig. 5.1. Consequently, the increase of the flow stresses does not correlate with the behavior of the major droplet axis, which varies non-monotonically for higher pressure drops.

The wall viscometric material functions and the droplet characteristics as a function of the wall shear rate, $\dot{\gamma}_w$, are identical to the steady shear viscometric functions and droplet characteristics in Fig. A.2. Thus the wall shear properties in laminar channel flow correspond to the viscometric properties in steady homogeneous shearing flow at the same value of shear rate. In a channel flow experiment, it is not clear whether the same properties will be detected since shear-induced migration from the wall or flow instabilities might occur at elevated pressure drops. These phenomena could lead to different shear rates at the walls.

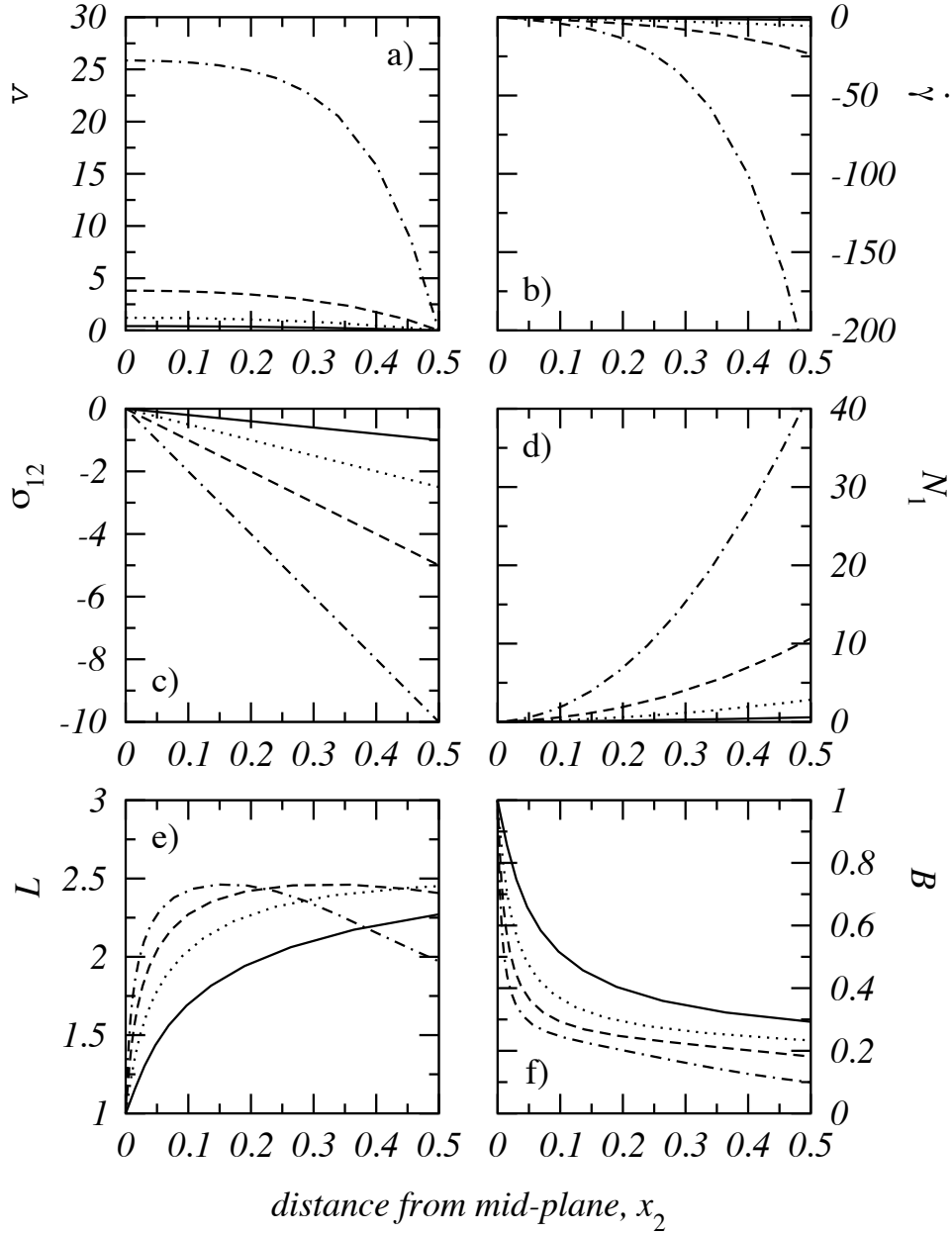


Figure 5.1.: Dimensionless channel flow profiles for a $\phi = 0.1$ PIB/PDMS blend for different pressure drops: $\nabla_1 p = -2$ (solid lines), -5 (dotted lines), -10 (dashed lines), -20 (dot-dashed lines). Model parameters are the same as in Fig. 4.9 and the number density of droplets is constant, $n = 1$. a) Velocity profile, b) shear rate profile, c) shear stress, d) first normal stress difference, e) major droplet axis, f) minor droplet axis.

5.1.2. Model with Break-up and Coalescence

After having solved and discussed the case $n = n_0$, we want to solve the system equations for a variable DDF ($n \neq n_0$) now. We do so to investigate whether non-monotonic trends of the droplet length occur also if break-up and coalescence are taken into account.

For solving the emulsion model accounting for break-up and coalescence, we adopt the model parameters of Sec. 4.2, *i. e.* $G/\Gamma = 4$, $\lambda_C \lambda_S / \lambda_n^2 = 1$, $\phi = 0.1$, $\theta = 0.001$, and $k = 0$. The viscosity ratio of the blend components is an independent parameter according to Eq. (3.7a), *i. e.* it is the ratio of Newtonian viscosities of the components, and we study the cases $p^* = -0.25$ and $p^* = -1.25$. First, we discuss the flow field of the polymer blend (Fig. 5.2), then we present the non-trivial components of the stress tensor and the droplet shape tensor (Fig. 5.3), and finally we discuss the droplet distribution function (Fig. 5.4).

Figure 5.2 shows the velocity and the shear rate profiles for the $p^* = -0.25$ emulsion and different pressure drops. We notice that the fluid has a maximum velocity on the mid-plane, and that the velocity vanishes on the channel walls to match the no-slip boundary condition (Fig. 5.2a). With the solution of the TPBV problem we know the velocity field, $v_1(x_2)$, which can be easily integrated, *e. g.* with a ten-point Gauss-Legendre integrator (Dressler and Edwards, 2005), to obtain the volumetric flow rate

$$Q = \int_{-W/2}^{+W/2} dx_3 \int_{-H/2}^{+H/2} v_1(x_2) dx_2, \quad (5.7)$$

where W is a unit-width of the channel. The volumetric flow rate, which corresponds to the area under the velocity profiles of Fig. 5.2a, increases with the pressure drop. Figure 5.2b shows that the shear rate increases monotonically from the mid-plane to the channel wall and it visualizes the strong deviation of the velocity profile from the parabolic Poiseuille profile of Newtonian liquids. This is evident mostly for the high pressure drop curves in Fig. 5.2.

Figure 5.3 shows the profiles of the flow stresses and the droplet shape as functions of the distance from the mid-plane for three pressure drops. Again, the shear stress varies linearly over the channel height, as required by the linearized momentum balance equation. The normal stress differences show a nonlinear increase as the walls are approached. Note that the absolute value of the shear stress in Fig. 5.3a is one order of magnitude smaller than the first normal stress difference in Fig. 5.3b. The second normal stress difference in Fig. 5.3c is again negative and of the same order of magnitude as the shear stress. The elastic stresses vary monotonically from the mid-plane to the

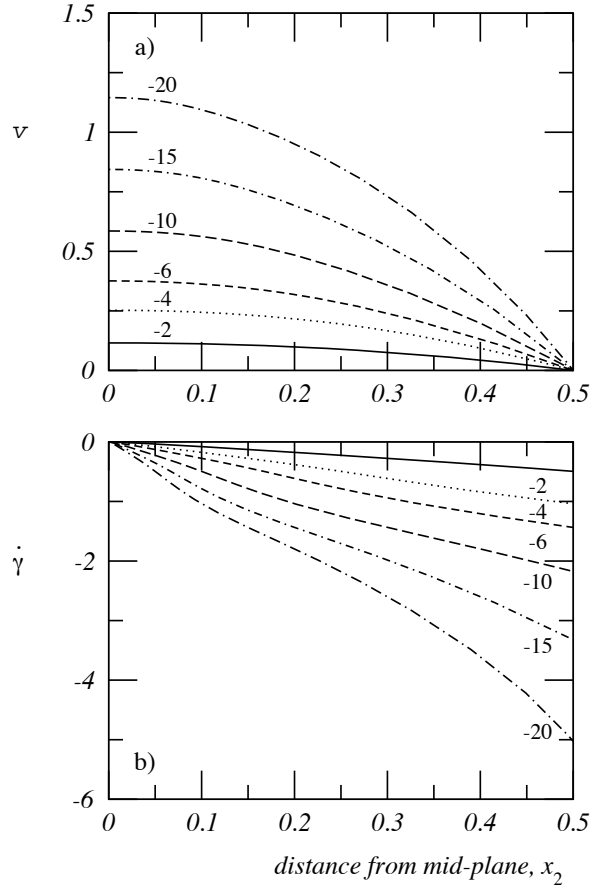


Figure 5.2.: Channel flow profiles for the model of Sec. 3.2, Eqs. (3.18) for different pressure drops: $\nabla_1 p = -2$ (solid lines), -4 (dotted lines), -6 (dashed lines), -10 (long dashed lines), -15 (dot-dashed lines), -20 (dot-long dashed lines). a) Velocity profile, b) shear rate profile. The viscosity ratio of the emulsion model is $p^* = -0.25$, other model parameters are the same as in Fig. 4.9: $G/\Gamma = 4$, $\lambda_C \lambda_S / \lambda_n^2 = 1$, $\phi = 0.1$, $\theta = 0.001$, $k = 0$.

walls. For a fixed position, the absolute value of the stress increases as the pressure drop is increased.

Figures 5.3d-f display the profiles of the droplet semiaxes. For small pressure drops, the major and the minor droplet axes vary monotonically as functions of the transversal direction. For the highest pressure drop, a non-monotonic variation of the three axes is recovered from the model equations. The vorticity axis in Fig. 5.3f shows a transition from the oblate ($W > 1$) to the prolate ($W < 1$) configuration regime near the centerline for the three pressure drops. An interesting conclusion from Fig. 5.3 is that the positions of the highest stresses in the channel (the walls) differ from the positions of the largest droplet deformation, which are located away from the walls at the maxima of the broken

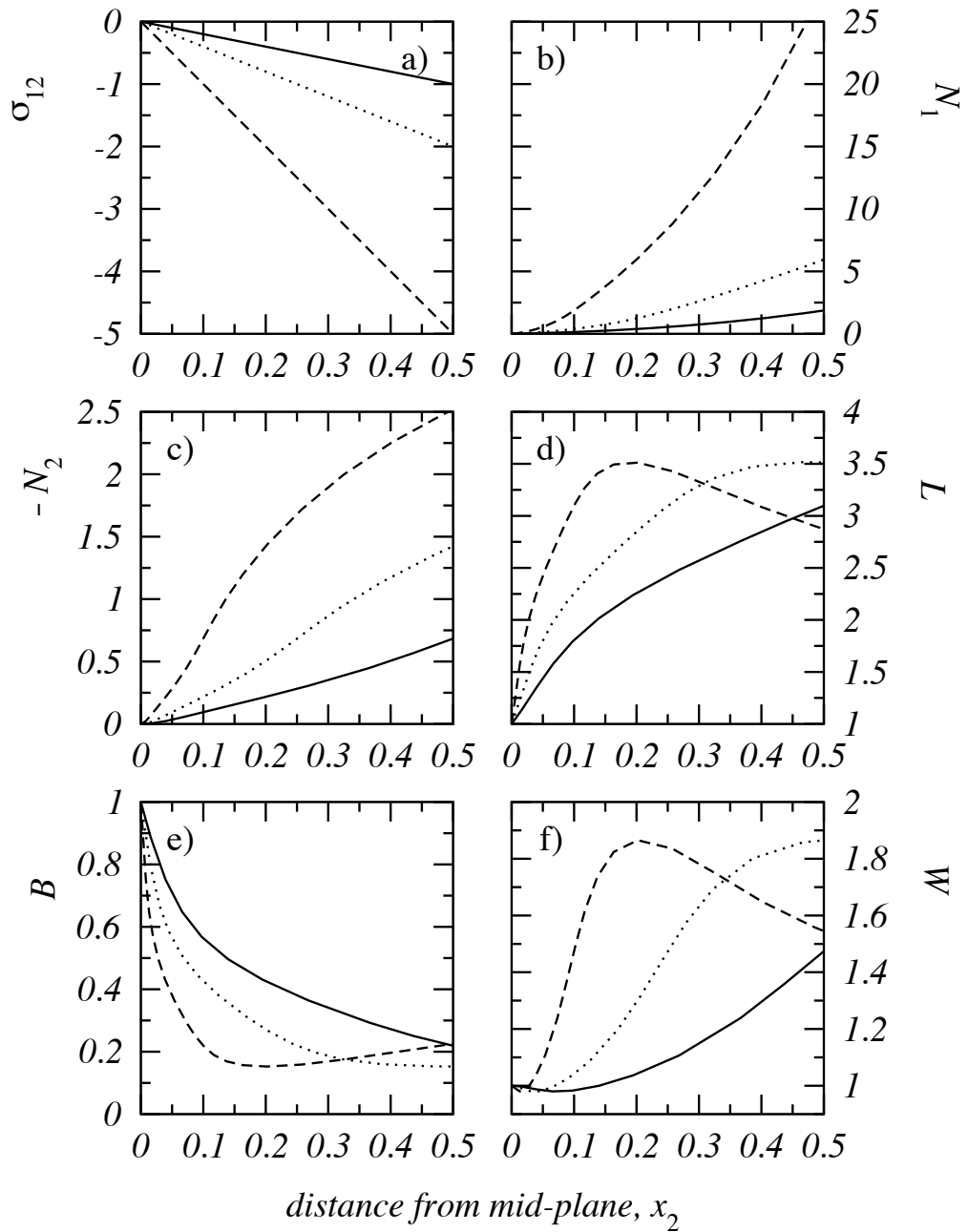


Figure 5.3.: The same as Fig. 5.2 for the extra stress tensor and the droplet shape tensor for three pressure drops: $\nabla_1 p = -2$ (solid lines), -4 (dotted lines), -10 (dashed lines). a) Shear stress, b) first normal stress difference, c) second normal stress difference, d) major droplet axis, e) minor droplet axis, f) vorticity axis.

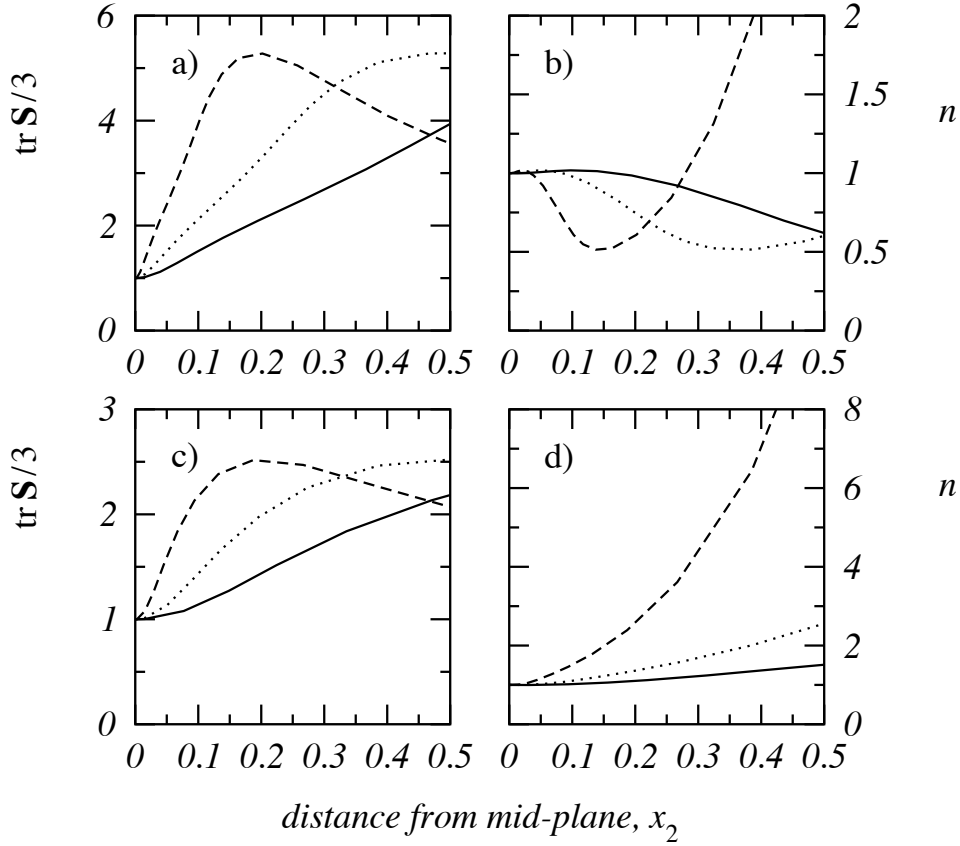


Figure 5.4.: The trace of the droplet shape tensor (right column) and the number density of droplets (left column) for $p^* = -0.25$ (first row) and -1.25 (second row) for three pressure drops: $\nabla_1 p = -2$ (solid lines), -4 (dotted lines), -10 (dashed lines). Other model parameters are the same as in Fig. 5.3.

lines in Figs. 5.3d-f. This is consistent with the steady shear trends of Fig. A.2e which also predict a non-monotonic droplet length in the high shear rate regime.

Figure 5.4 shows the position and the height of the droplet distribution for the $p^* = -0.25$ (Figs. 5.4a, b) and the $p^* = -1.25$ emulsions (Figs. 5.4c, d) as functions of the distance from the mid-plane. We report sample calculations for the three pressure drops discussed in Fig. 5.3. For the smallest pressure drop, the maximum of the DDF is shifted towards larger droplet sizes as we approach the channel wall. For the largest pressure drop, the maximum of the DDF is first shifted towards larger droplet sizes near the mid-plane. As the channel walls are approached, the maximum of the DDF shifts backwards to smaller sizes. This holds for the low viscosity ratio blend as well as for the high viscosity ratio blend (Figs. 5.4a, 5.4c). As already seen for the emulsion model of Sec. 3.1 the wall viscometric functions and droplet characteristics as a function of the wall shear rate are

identical to the steady state properties of Figs. 4.9-4.11.

The droplet number density for the low viscosity ratio blend is displayed in Fig. 5.4b. For the smallest pressure drop, we observe flow-induced break-up near the mid-plane and flow-induced coalescence near the walls (solid line in Fig. 5.4b). For the highest pressure drop, we see flow-induced break-up near the mid-plane and near the walls. Between the mid-plane and the wall, there is a region of flow-induced coalescence (Fig. 5.4b). For the high viscosity ratio blend in Fig. 5.4d, the droplet number density is a monotonically increasing function of the three pressure drops, and we have flow-induced break-up along the transversal direction.

Figures 5.2-5.4 show that the emulsion model of Sec. 3.2 predicts a non-monotonic droplet length at high shear rates. In this model the disperse phase dynamics is influenced by the deformation of the matrix fluid and the variable number density of micro-droplets. We believe that both mechanisms are reasonable from a physical point of view. On the one hand, matrix deformation influences droplet deformation even if break-up and coalescence do not occur. On the other hand, the break-up/coalescence events have an effect on matrix and droplet deformation. It should be checked whether the sole assumption of a variable number density (i.e., $\theta = 0$) is sufficient to produce a non-monotonic droplet length.

An obvious conclusion of Figs. 5.2-5.4 is that laminar tube flow is not an advantageous dispersion flow because there is no droplet deformation around the mid-plane of the channel. Next, we study dispersing characteristics of Couette flow and of mixed Poiseuille-Couette flow. Therefore, we solve the emulsion model in the annular gap between concentric cylinders since it is a typical dispersing geometry in process engineering.

5.2. Annular Flow

The emulsion model of Sec. 3.2 is solved for flows in the annular gap between two concentric cylinders with inner radius R_i and outer radius R_o . We explain how the coefficient matrix \mathcal{A} , and the inhomogeneity \mathbf{b} , in Eq. (5.2) change with respect to channel and tube flow. The ratio of cylinder radii is $\kappa = R_i/R_o$, the annular gap is $\delta = R_o - R_i$, and the relative distance from the inner cylinder is $\bar{r} = (r - R_i)/(R_o - R_i)$. Now the gap width, δ , is the characteristic length scale of the flow problem. Again, we adopt cylindrical coordinates (r, φ, z) to describe the flow. We study flows of the form

$$\mathbf{v} = v_\varphi(r)\mathbf{e}_\varphi + v_z(r)\mathbf{e}_z, \quad (5.8)$$

i. e. there is no radial fluid flow in the annulus. The density of the material is constant since the divergence of the velocity field (in cylindrical coordinates) is zero. The no-slip boundary conditions to be imposed on the velocity field are

$$v_\varphi(r = R_i) = U, \quad (5.9a)$$

$$v_z(r = R_o) = 0, \quad (5.9b)$$

$$v_z(r = R_i) = 0, \quad (5.9c)$$

$$v_\varphi(r = R_o) = 0. \quad (5.9d)$$

The inner cylinder rotates at a constant angular velocity, $\boldsymbol{\Omega} = U/R_i \mathbf{e}_z$, generating Couette flow in the annular gap and a constant pressure drop along the cylinder axis, $\nabla_z p$, leads to axial through-flow. Note that for large inner cylinder velocities or large axial pressure drops the fluid will also move in the radial direction. The treatment of outer cylinder rotation or of two rotating cylinders is analogous as will be seen from the following.

Due to the rotation of the inner cylinder we have now non-linear convective terms in the momentum balance equation, in the conformation tensor equation, and in the droplet shape tensor equation. These centrifugal terms are not present in laminar channel and tube flow but they arise in the annulus if one or both cylinders rotate around their common axis.

The Cauchy momentum balance in dimensionless form is

$$\text{Ta} \mathbf{v} \cdot \nabla \mathbf{v} = \nabla \cdot \boldsymbol{\sigma} - \nabla p, \quad (5.10)$$

where $\text{Ta} = \rho^2 U^2 \delta^3 / (R_i G \lambda_C \Gamma \lambda_S)$ is the Taylor number and the model equations (3.18) are rendered dimensionless as before for the channel and tube flow problems, except that now the characteristic length scale of the flow geometry is δ , *i. e.*, $\tilde{\mathbf{r}} = \mathbf{r}/\delta$, $\tilde{\nabla} = \delta \nabla$. The Taylor number increases with the inner cylinder velocity, *i. e.* an increase of U corresponds to an increase of Ta .

The reversible contribution to the conformation tensor equation (3.18b) and the droplet shape equation (3.18c) are of the form

$$\mathbf{v} \cdot \nabla \mathbf{X} - \mathbf{X} \cdot \nabla \mathbf{v} - (\nabla \mathbf{v})^T \cdot \mathbf{X} = \hat{Q} \mathbf{X} + \frac{v_\varphi}{r} \mathbf{M} - \mathbf{X} \cdot \nabla \mathbf{v} - (\nabla \mathbf{v})^T \cdot \mathbf{X}, \quad (5.11)$$

where $\mathbf{X} \in \{\mathbf{C}, \mathbf{S}\}$ (Tanner, 2000). In Eq. (5.11) we have $\hat{Q} = v_r \partial_r + v_\varphi / r \partial_\varphi + v_z \partial_z$,

$$\mathbf{M} = \begin{pmatrix} -2X_{r\varphi} & X_{rr} - X_{\varphi\varphi} & -X_{\varphi z} \\ * & 2X_{r\varphi} & X_{rz} \\ * & * & 0 \end{pmatrix}, \quad (5.12)$$

is a matrix with $*$ denoting a symmetric entry, and the velocity gradient tensor is given by Eq. (5.14), below. For laminar flow in the annulus geometry, we have $\widehat{Q} = 0$ since $v_r = 0$, and the flow is homogeneous in the \mathbf{e}_ϕ and \mathbf{e}_z direction.

The model equations (3.18) are reformulated in terms of a TPBV problem (5.2) for the radial coordinate and the boundary conditions (5.9). The 18-tuple of flow profiles to solve for is

$$\boldsymbol{\xi} = (p, v_\phi, v'_\phi, v_z, v'_z, \text{vec}(\mathbf{C}), \text{vec}(\mathbf{S}), n)^T, \quad (5.13)$$

where $\text{vec}(\mathbf{X}) = (X_{rr}, X_{r\phi}, X_{rz}, X_{\phi\phi}, X_{\phi z}, X_{zz})$ and $\mathbf{X} \in \{\mathbf{C}, \mathbf{S}\}$, denotes the microstructural tensors. The 18×18 -coefficient matrix, \mathcal{A} , and the inhomogeneity, \mathbf{b} , in Eq. (5.2) are obtained as for the laminar channel and tube flow problem in the previous sections. The first row of $(\mathcal{A}, \mathbf{b})$ is obtained from the r -component of the Cauchy momentum balance equation (5.10), and the third and fourth row are obtained from the $r\phi$ and rz equations of Eq. (3.18b), respectively.

The set of ODEs $\boldsymbol{\xi} = \mathcal{A}^{-1} \cdot \mathbf{b}$ is integrated with the Runge-Kutta algorithm shooting from the inner cylinder, $r = R_i$, to the outer cylinder, $r = R_o$. Every Runge-Kutta shoot starts with the same initial condition, Eq. (5.9), on the velocity field and a different velocity gradient on the inner cylinder being the independent variable in the Newton subroutine of the shooting algorithm. Here we have to match *two* boundary conditions on the outer cylinder, Eqs. (5.9) and the flow fields are not symmetric. This means that we have to integrate the model equations from the inner cylinder to the outer one and we do not know the structural variables on the inner cylinder since the shear rate is non-trivial on the inner cylinder. Therefore, a two-dimensional Newton method for the variables v'_ϕ and v'_z is embedded into the shooting algorithm to match the two relevant boundary conditions, (5.9). Consequently, prior to every Runge-Kutta integration in the shooting algorithm, the homogeneous shear flow problem for the velocity gradient

$$\nabla \mathbf{v} = \begin{pmatrix} 0 & -\frac{v_\phi}{r} & 0 \\ \frac{\partial v_\phi}{\partial r} & 0 & 0 \\ \frac{\partial v_z}{\partial r} & 0 & 0 \end{pmatrix}^T, \quad (5.14)$$

is solved on the inner cylinder to determine correct starting values for the structural variables \mathbf{C} and \mathbf{S} . The Runge-Kutta integrations are repeated until the Newton algorithm has converged, *i. e.* the boundary conditions on the outer cylinder, Eq. (5.9) are satisfied.

We show solutions of the emulsion model for Couette, Poiseuille, and helical flow in a gap with $\kappa = 0.5$. The model parameters are taken from Sec. 4.2; $G/\Gamma = 4$, $\lambda_C \lambda_S / \lambda_n^2 = 1$,

$\phi = 0.1$, $\theta = 0.001$, and $k = 0$, and we present sample calculations for an emulsion with viscosity ratio $p^* = -0.25$ and $p^* = -1.25$.

5.2.1. Couette Flow

We consider the case of Couette flow generated via rotation of the inner cylinder with a stationary outer cylinder. Figure 5.5 shows the angular velocity field and the non-trivial components of the extra-stress tensor for various inner cylinder velocities, *i. e.* different Taylor numbers. The viscosity ratio of the blend components is $p^* = -0.25$. Figure 5.5a displays the velocity field as a function of the relative distance from the inner cylinder for various inner cylinder velocities which can be identified from the abscissa of Fig. 5.5a. We see that the velocity field satisfies the no-slip boundary conditions on the two cylinders, in particular that the fluid velocity on the inner cylinder corresponds to the cylinder velocity, U . Figure 5.5b is the shear rate, as a function of the relative distance from the inner cylinder. The absolute value of the shear rate decreases monotonically as we approach the outer cylinder. The absolute mean value of the shear rate, $(v_\varphi(R_i) - v_\varphi(R_o))/\delta$, increases with increasing Taylor number. Note that in Fig. 5.5 the shear rate in the annular gap is a non-trivial function of the distance from the inner cylinder and in particular that the shear rate is not constant. Even for the smallest inner cylinder velocity the shear rate in the annulus is not constant. Only for the narrow gap ($\kappa \rightarrow 1$) the velocity field is linear, the shear rate and the shear stress are constant, and the shear rate and elastic stresses increase with inner cylinder velocity. For $\kappa = 0.9$ we find that the narrow gap approximation holds for cylinder velocities $U < 0.1$. The extra-stress tensor components are shown in Fig. 5.5c-f. The radial-axial shear stress and the angular-axial shear stress components are zero. The radial normal stresses in Fig. 5.5c behave qualitatively different for low and for high inner cylinder velocities. Whereas for small Taylor numbers the radial normal stress increases monotonically near the inner cylinder, for large Taylor numbers it decreases near the inner cylinder.

A linear stability analysis of our solutions allows to understand whether this behavior of the radial normal stresses is realistic. Note that the variation of radial normal stresses in the fluid are in equilibrium with centrifugal forces and with the radial pressure drop in the gap, *i. e.*

$$-\text{Ta} \frac{v_\varphi^2}{r} = \frac{1}{r} \frac{\partial}{\partial r} (r \sigma_{rr}) - \frac{\sigma_{\varphi\varphi}}{r} - \frac{\partial p}{\partial r} \quad (5.15)$$

according to the r -component of Cauchy's momentum balance (5.10). For large Taylor numbers the variation of the normal stresses and the radial pressure drop increase in the gap. This can lead to radial motion of the emulsion, *i. e.* the laminar solution of Fig. 5.5 is unstable. It would be interesting to find out whether there exists a critical pressure

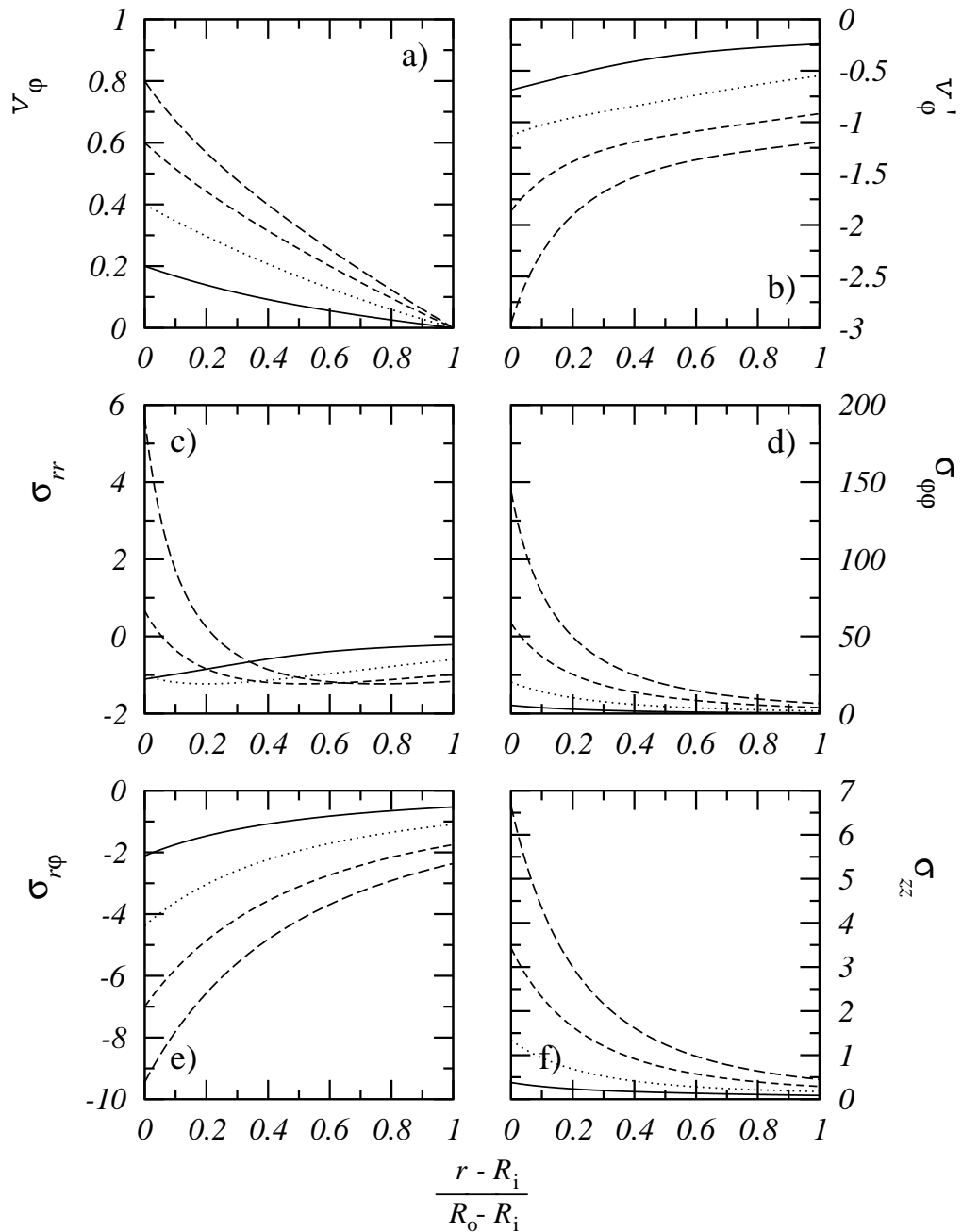


Figure 5.5.: Couette flow profiles of an emulsion ($\phi = 0.1$) in the annular gap ($\kappa = 0.5$) for four inner cylinder velocities: $U = 0.2$ (solid lines), 0.4 (dotted lines), 0.6 (dashed lines), 0.8 (long-dashed lines), and $\nabla_z p = 0$. Model parameters are $G/\Gamma = 4$, $\lambda_C \lambda_S / \lambda_n^2 = 1$, $\theta = 0.001$, $k = 0$, $p^* = -0.25$.

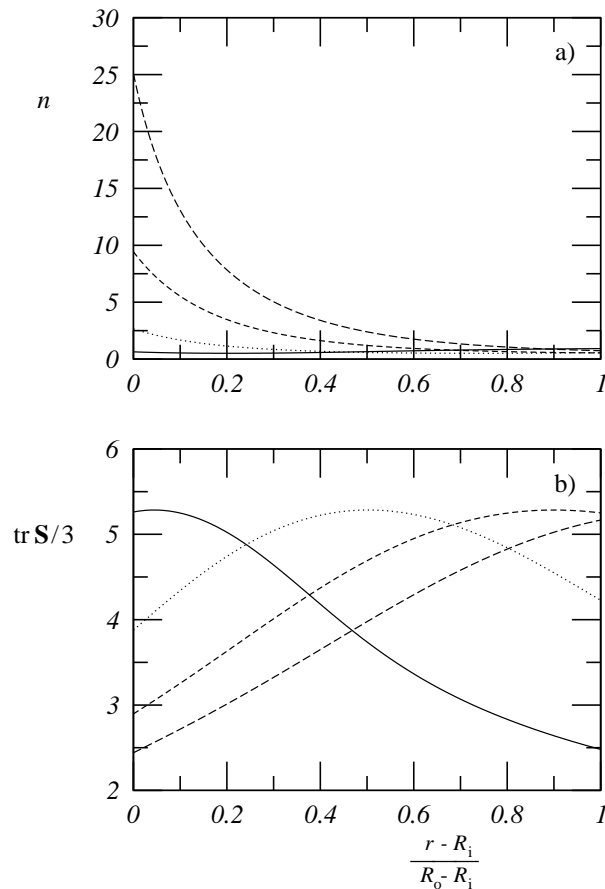


Figure 5.6.: The same as Fig. 5.5 for (a) the relative number density of droplets and (b) the representative droplet size.

drop where Couette flow becomes unstable and where we expect Taylor vortices. If this quantity becomes very large the laminar flow field of Fig. 5.5 are probably unstable.

For the angular normal stress (Fig. 5.5d) and the axial normal stress (Fig. 5.5f) we find a monotonic decrease as we approach the outer cylinder. These stresses increase with the Taylor number. The radial angular shear stress in Fig. 5.5e is a monotonic function in the annular gap and its absolute magnitude increases with increasing inner cylinder velocity. Note that the angular shear rate and the angular radial shear stress are non-linear functions of the relative distance from the inner cylinder and the assumption of a constant shear rate and shear stress in the gap is critical. Also the approximation of shear rate and stresses with the values on the inner or the outer cylinder is critical.

The characteristics of the DDF in the gap are reported in Fig. 5.6. Figure 5.6a shows the relative number density of micro-droplets in the annular gap and Fig. 5.6b the average

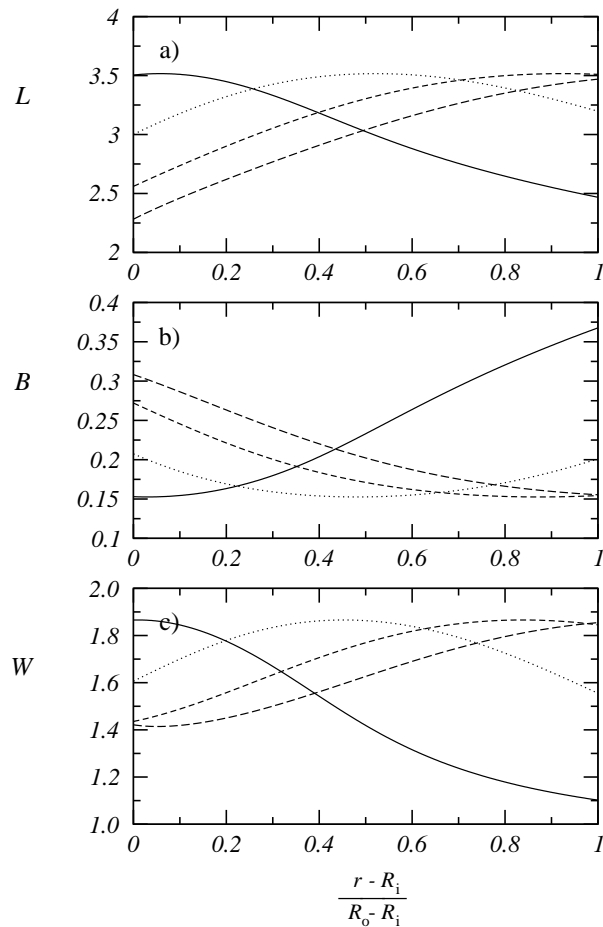


Figure 5.7.: The same as Fig. 5.7 for the droplet semiaxes. (a) Major droplet semiaxis, (b) minor droplet semiaxis, and (c) vorticity axis.

size of micro-droplets as a function of the relative distance from the inner cylinder. For small values of the inner cylinder velocity the average number density of micro-droplets decreases below the equilibrium value in the annular gap, *i. e.* we have flow induced coalescence in the gap. For $U = 0.4$ we have break-up near the inner cylinder (position of highest shear rates) and coalescence near the outer cylinder (position of smallest shear rate). The same holds also for $U = 0.6$ and $U = 0.8$, except that now high values of droplet number density are found near the outer cylinder. For the largest Taylor number in Fig. 5.6a the number density of droplets near the inner cylinder is 25 times higher than in the undeformed state. The large break-up rates near the inner cylinder are due to centrifugal forces being proportional to v_φ^2 . It might be interesting to compare calculations for $Ta = 0$ and $\mathbf{M} = \mathbf{0}$ with the calculations shown in Fig. 5.6 to understand the effect of centrifugal forces on droplet break-up. The average size of micro-droplets in the annular gap is reported in Fig. 5.6b. We notice that the average droplet size is a non-monotonic function of the relative distance from the inner cylinder. For the

smallest Taylor number the largest droplets are found near the inner cylinder. This is consistent with Fig. 5.6a where for $U = 2$ coalescence occurs in the whole gap and we have larger coalescence rates on the inner cylinder than on the outer one. For large values of inner cylinder velocity the largest droplets are found on the outer cylinder (where coalescence occurs) and the smallest droplets are found on the inner cylinder (where break-up occurs).

In Fig. 5.7 we plot the three semiaxes of the ellipsoidal droplets as a function of the relative distance from the inner cylinder. Figure 5.7 shows the major droplet axis which correlates with the average droplet size of Fig. 5.6b. For the four inner cylinder velocities the droplet length is more than twice the equilibrium droplet size in the annular gap, *i. e.* we have large droplet deformation in Couette flow. For the smallest Taylor number the largest droplets are found on the inner cylinder and for larger Taylor numbers they are found on the outer cylinder. The minor droplet axis is shown in Fig. 5.7b. As already found for the droplet size in Fig. 5.6b and the major droplet size in Fig. 5.7a the minor droplet axis increases towards the outer cylinder for small values of inner cylinder speed and it decreases for the largest value of U . Figure 5.7c shows the droplet width as a function of the relative distance from the inner cylinder. Note that this quantity is greater than one for all cylinder velocities in Fig. 5.7.

An important conclusion of Fig. 5.6a is that large Taylor numbers lead to high break-up rates on the inner cylinder and coalescence near the outer cylinder. Consequently, dispersing with stationary outer cylinder is not effective if one defines effectiveness as break-up in the whole geometry. Probably the rotation of both cylinders results in more effective dispersing in the gap. Lets now treat Poiseuille flow in the gap and study its dispersing characteristics.

5.2.2. Poiseuille Flow

Figure 5.8 displays the velocity and stress tensor components for Poiseuille flow in the annular gap. Here, the flow is due to an axial pressure drop. We show sample calculations for an emulsion $p^* = -1.25$ and five pressure drops. Figure 5.8a is the emulsion velocity as a function of the relative distance from the inner cylinder. The velocity vanishes on the two cylinders due to the no-slip boundary conditions and the position of maximum velocity is a non-trivial function of shear rate. The axial through flow, *i. e.* the area under the velocity profile, increases with the pressure drop. Figure 5.8b shows the shear rate as function of the relative distance from the inner cylinder. The position of maximum axial velocity, *i. e.* zero shear rate, is near the inner cylinder at $r < \kappa/2$. Furthermore, shear rates are larger on the inner cylinder than on the outer one. Figure 5.8c-f show the components of the stress tensor as a function of the distance from the

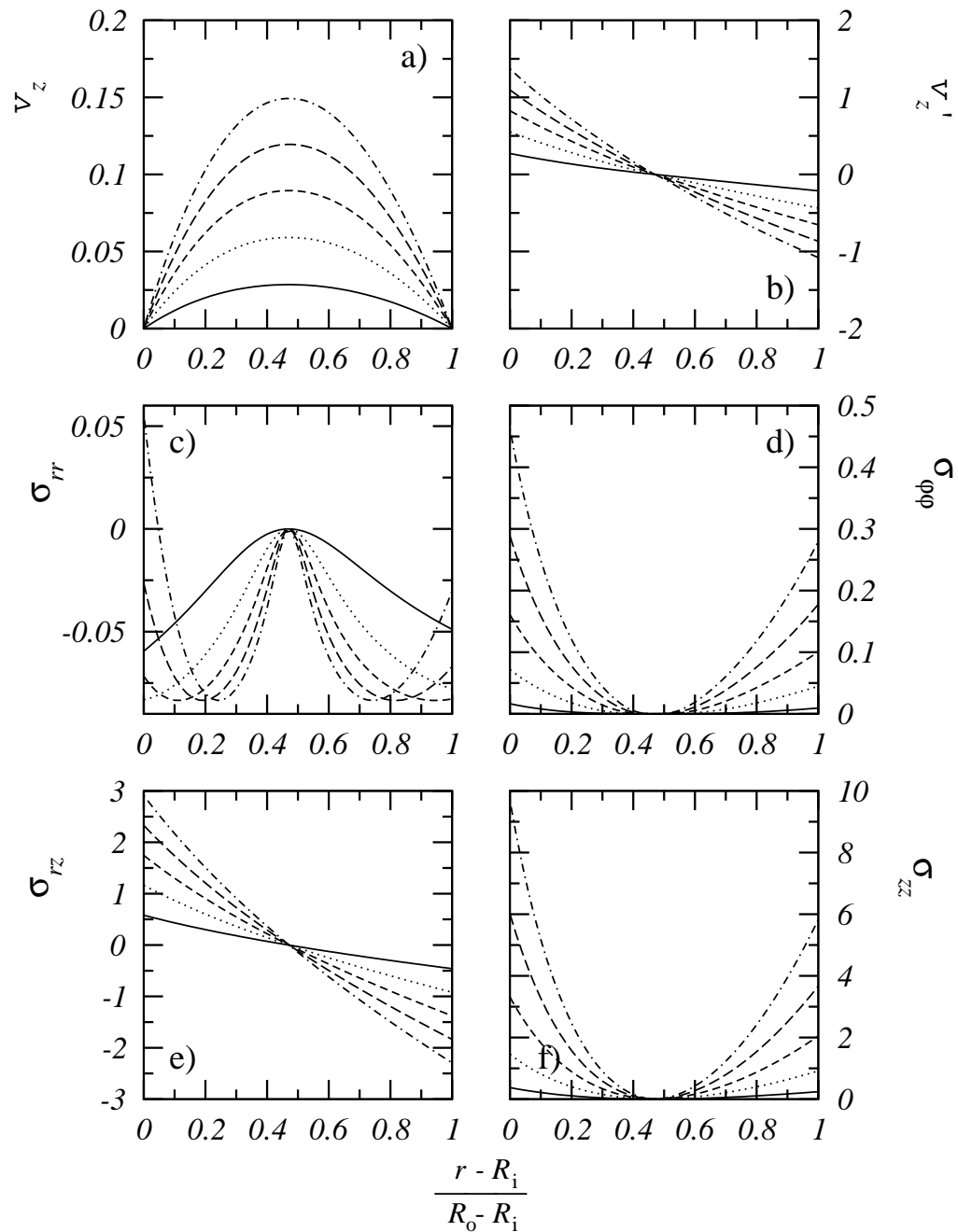


Figure 5.8.: Poiseuille flow profiles of an emulsion ($\phi = 0.1$) in the annular gap ($\kappa = 0.5$) for five pressure drops: $\nabla_z p = -0.2$ (solid lines), -0.4 (dotted lines), -0.6 (dashed lines), -0.8 (long-dashed lines), -1 (dot-dashed lines), and $U = 0$. The viscosity ratio is $p^* = -1.25$. Other model parameters are the same as in Fig. 5.5.

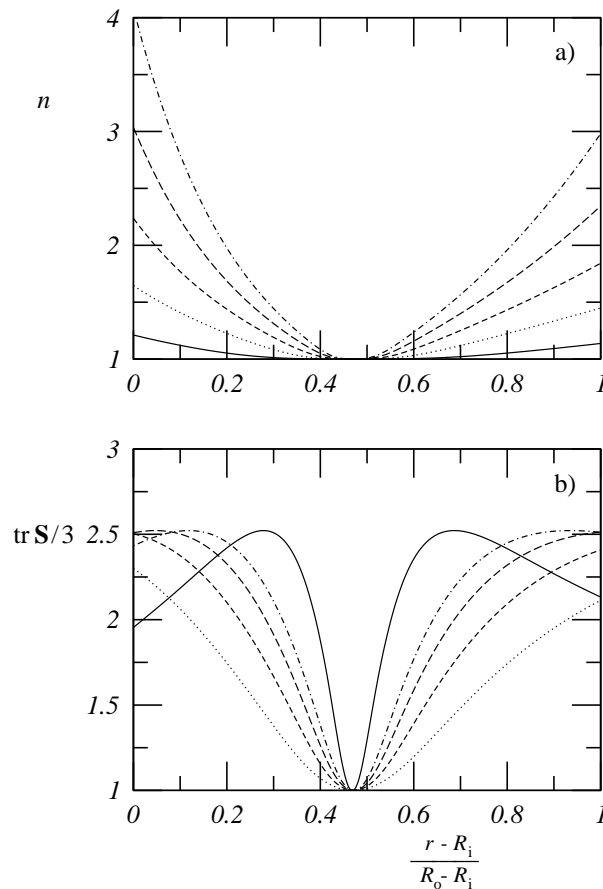


Figure 5.9.: The same as Fig. 5.8 for (a) the relative number density of droplets and (b) the representative droplet size.

inner cylinder. Now the radial-angular and the angular-axial shear stresses are zero. Figure 5.8c shows the radial normal stress as a function of the radial position. It is interesting that the variation of the radial normal stress correlates with the velocity field for the two small pressure drops in Fig. 5.8. For the larger pressure drops the radial normal stress is non-monotonic with local minima near the inner and the outer cylinder. Via the Cauchy momentum balance equation the radial normal stress is related to the radial pressure distribution in the gap. It would be interesting to investigate the linear stability of the laminar flow solutions and to understand whether the profiles of the radial normal stresses are physically reasonable. Furthermore, calculations should be done for a narrow gap to see whether a monotonic trend for the radial normal stress is recovered. In Fig. 5.8d,f we show the angular normal stress profile and the axial normal stress profile, respectively. Note that both normal stresses are larger on the inner cylinder than on the outer. Furthermore, both quantities correlate with the variation of the axial velocity field of Fig. 5.8a. The radial axial shear stress of the emulsion is displayed in

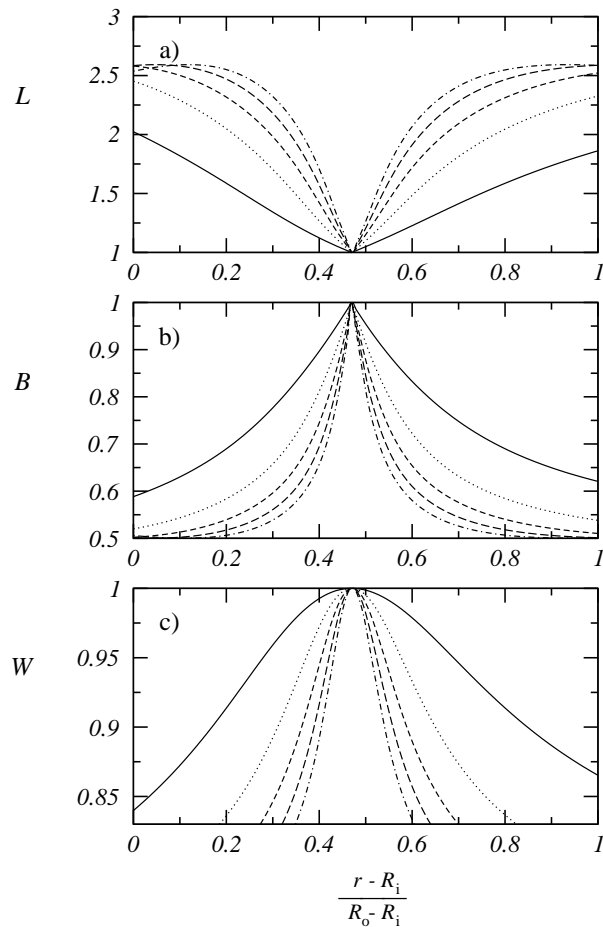


Figure 5.10.: The same as Fig. 5.8 for the droplet semiaxes. (a) Major droplet semiaxis, (b) minor droplet semiaxis, (c) vorticity axis.

Fig. 5.8e. This quantity correlates with the shear rate distribution of Fig. 5.8b.

Note that we find a similar stress tensor behavior for laminar Couette flow (Fig. 5.5) and laminar Poiseuille flow (Fig. 5.8). The angular normal stresses, the axial normal stresses, and the shear stress profiles correlate with the velocity field. They show the same qualitative behavior for the regime of inner cylinder velocities and axial pressure drops in Figs. 5.5 and 5.8. The radial normal stress profiles change qualitatively as the Taylor number or the axial pressure drop are increased. Also note that all flow stresses are larger on the inner cylinder than on the outer cylinder, a result that was also found for laminar Couette flow in Fig. 5.5.

Figure 5.9 shows the number density of droplets (Fig. 5.9a) and the average size of representative droplets (Fig. 5.9b) in the annulus. As already seen for the flow stresses in Fig. 5.8c-f also the number density of droplets is non-symmetric with a maximum

number density on the inner cylinder. The minimum of the number density is found near the inner cylinder, where the axial velocity is maximum and where the shear rate and the radial axial shear stress vanish. Note that in Fig. 5.9a the number density of droplets on the inner cylinder is more than five times smaller than in Couette flow (Fig. 5.6b) though the shear rates in Fig. 5.5b and Fig. 5.8b are almost the same. The strong break-up rates encountered in Couette flow (Fig. 5.6b) are due to centrifugal forces. The profile of the average droplet sizes in pressure driven annular flow are shown in Fig. 5.9b. Here we observe that the profiles of average droplet size are non-monotonic for the smallest pressure drop and monotonic for the largest pressure drop. Again, the position of equilibrium droplet size is identical to the position of equilibrium droplet number density, maximum fluid velocity, and vanishing shear rate and shear stress in the gap.

In Fig. 5.10 we show the profiles of the ellipsoidal droplets for five pressure drops. Figure 5.10a are the profiles of the major droplet axis being greater than one, Fig. 5.10b are the profiles of the minor droplet axis being smaller than one, and Fig. 5.10c are the profiles of the vorticity axis. Again, the position of undeformed droplets correlates with the position of maximum fluid velocity, *i. e.* of zero shear rate and shear stress. The viscosity ratio of $p^* = -1.25$ leads to $W < 1$, *i. e.* the droplets in the gap are prolate.

A major difference between Couette flow (Figs. 5.5-5.7) and Poiseuille flow (Figs. 5.8-5.10) is that in Poiseuille flow we have droplet break-up around a position of undeformed droplets for all pressure drops. In Couette flow, we have positions with droplet break-up and positions with droplet coalescence. We have seen from Fig. 5.9a that dispersing in pressure driven flow is not as effective as in Couette flow because break-up rates are much smaller though shear rates are more or less the same. Furthermore, there is a position of zero shear rate in the annular gap where droplets do not deform.

5.2.3. Helical Flow

We have seen that Couette flow due to inner cylinder rotation is not very effective for dispersing since we get droplet break-up near the inner cylinder and droplet coalescence near the outer one. For pure Poiseuille flow we have mainly droplet break-up in the annulus. However, at the point of zero shear rate in the annular gap droplets stay undeformed. Lets now look at helical flow in the annulus and investigate its effect on droplet dispersing behavior.

In Figs. 5.11-5.14 we show sample calculations for helical flow of a $p^* = -1.25$ blend in the annular gap $\kappa = 0.5$. In Fig. 5.11 the velocity is shown together with the corresponding shear rates. Figure 5.11a and 5.11b show the angular velocity and the corresponding

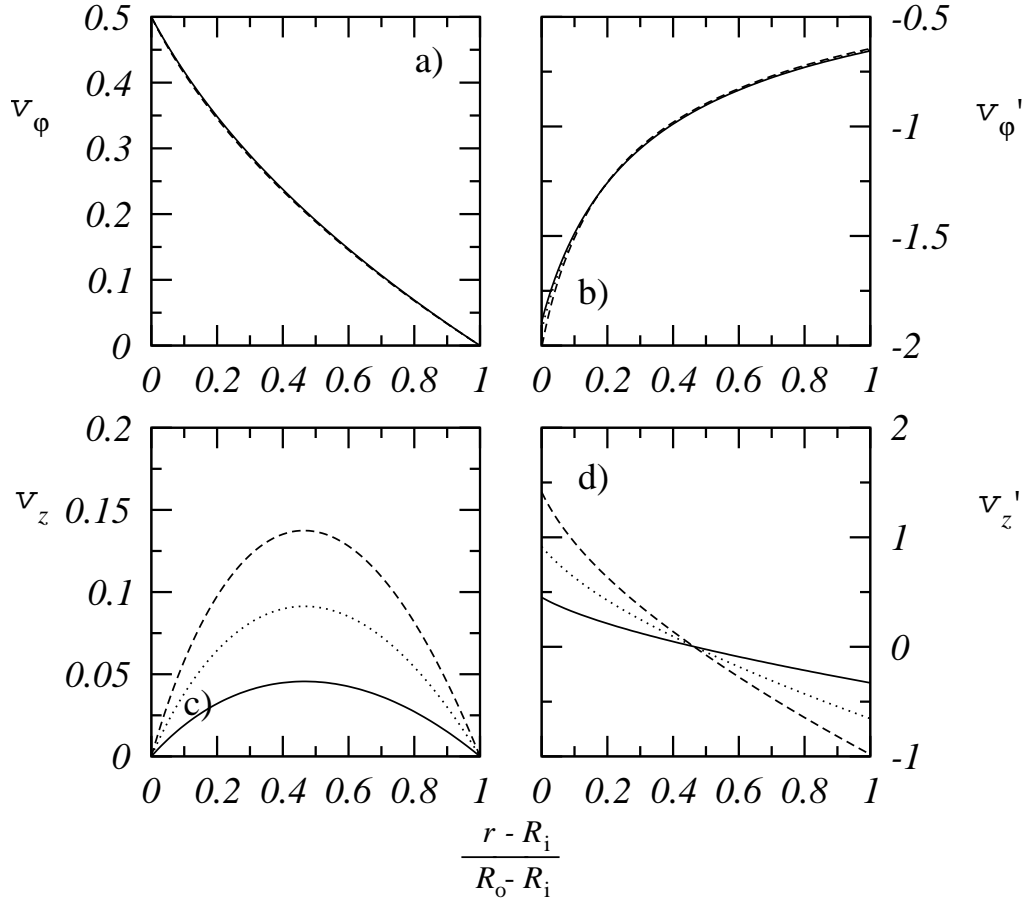


Figure 5.11.: Helical flow profiles of an emulsion ($\phi = 0.1$) in the annular gap ($\kappa = 0.5$) for inner cylinder velocity ($U = 0.5$) and three axial pressure drops: $\nabla_z p = -3$ (solid lines), -6 (dotted lines), -9 (dashed lines). The viscosity ratio of the blend is $p^* = -1.25$. Other model parameters are the same as in Fig. 5.8.

shear rate.

We report sample calculations for inner cylinder velocity $U = 0.5$ and three axial pressure drops. The angular velocity in Fig. 5.11a matches the no-slip boundary conditions and the axial pressure drop has a small effect on the angular velocity. The same is also true for the angular shear rate. The angular and the axial motion of the blend cannot be studied independently of each other but that they are coupled via the non-linear elastic stresses. The absolute value of the angular shear rate is larger on the inner cylinder than on the outer one. The axial pressure drop results in steeper angular shear rate profile since the absolute value of the angular shear rate is increased on the two cylinders. Figure 5.11c,d show the axial velocity field and the corresponding shear rate. Again, the axial velocity matches the no-slip boundary conditions, the position of maximum fluid

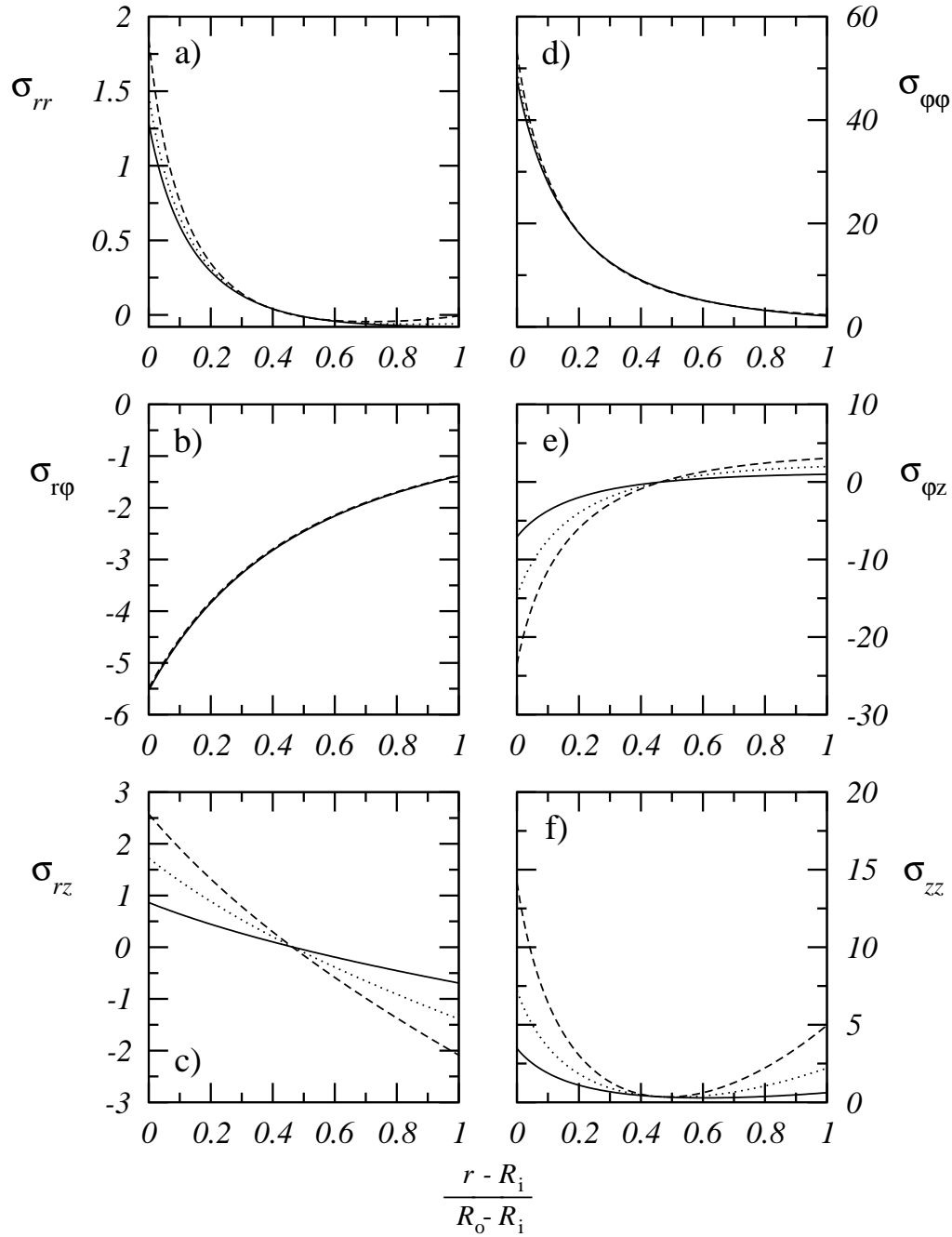


Figure 5.12.: The same as Fig. 5.11 for the profiles of the extra stress tensor.

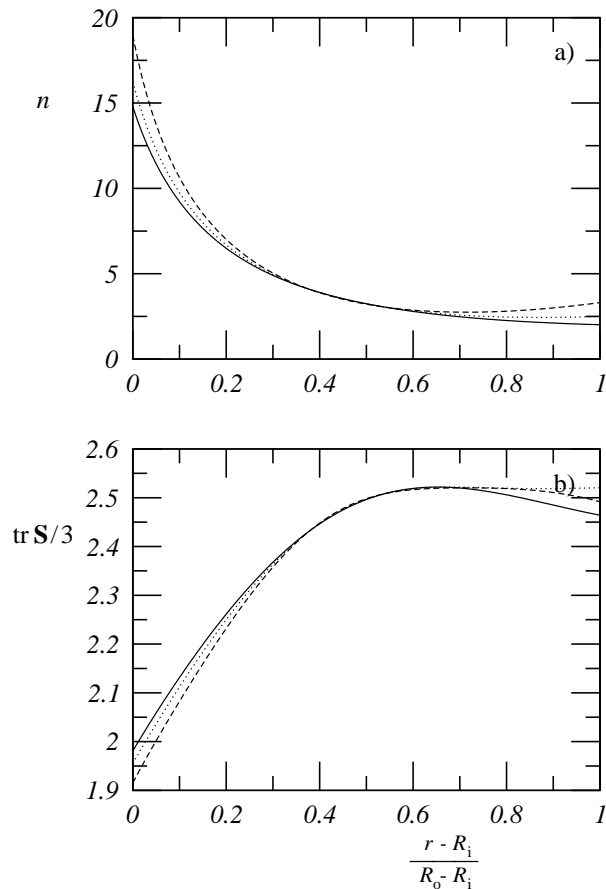


Figure 5.13.: The same as Fig. 5.11 for (a) the relative number density of droplets and (b) the representative droplet size.

velocity coincides with the position of vanishing axial shear rate in Fig. 5.11d, and it is near the inner cylinder. We expect the Taylor number to have minor influence on the axial motion.

The shear stress profiles corresponding to the velocity field of Fig. 5.11 are shown in Fig. 5.12. The appearance of a non-trivial angular-axial shear stress component means that the angular and the axial flow of the emulsion cannot be considered separately from each other due to the non-linear elastic stresses. The flow and the non-linear stresses are coupled non-linearly. Figure 5.12a shows the radial normal stress profile. This component is dominated by the angular velocity of the emulsion (Fig. 5.5c) and the axial flow leads to an increase of the radial normal stresses near the inner cylinder. Figure 5.12b displays the radial angular shear stress profile. The effect of the axial motion of the blend has only a minor influence on this shear stress component since the three curves in Fig. 5.12b superimpose. Figure 5.12c shows the radial axial shear

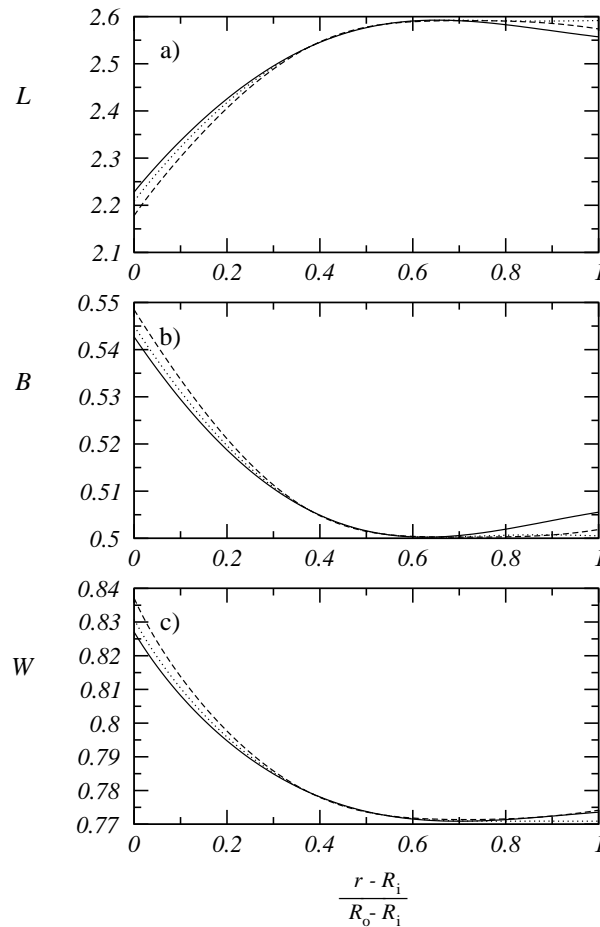


Figure 5.14.: The same as Fig. 5.11 for the three droplet semiaxes. (a) Major droplet semiaxis, (b) minor droplet semiaxis, and (c) vorticity axis.

stress profile. This component is mainly due to the axial shear flow of the blend and consequently it is a strong function of the axial pressure drop. The angular velocity is expected to have only minor influence on this stress tensor component. Figure 5.12d shows the angular normal stress profile. This stress tensor component is dominated by the angular motion of the emulsion as reveals a comparison of Fig. 5.12d with the corresponding stress tensor profile for pure Couette flow (Fig. 5.5d) and pure Poiseuille flow (Fig. 5.8d). Again, the axial fluid motion has only minor influence on this shear stress component. Figure 5.12e is the angular-axial shear stress profile. This component arises only in helical flow. For the flow parameters (*i. e.* inner cylinder velocity and axial pressure gradient) this component correlates with the angular velocity field of the material. Figure 5.12f is the axial normal stress. For the axial normal stress profile we find that it is dominated by the Couette flow contribution for small pressure drops and by the pressure flow contribution for large pressure drops. Again, this can be understood by comparing Fig. 5.12f with Fig. 5.5 for Couette flow and Fig. 5.8 for Poiseuille flow.

The droplet number variation in the gap and the average droplet size are shown in Fig. 5.13. Note that on the inner cylinder the average number density of droplets is between fifteen and twenty. The centrifugal forces lead to strong droplet break-up near the inner cylinder. The superimposed pressure flow leads to a further increase of the number density of droplets, *i. e.* to even higher break-up rates. On the outer cylinder we have still break-up but break-up rate are much smaller compared to the inner cylinder. Note that the imposition of an axial pressure drop on the Couette flow allows to obtain droplet break-up in the whole gap. For pure Couette flow we found a region of coalescence near the outer cylinder. Thus the advection of the material in the axial direction results in a better dispersion of the blend. The average size of droplets is small on the inner cylinder and large on the outer cylinder. The superimposed pressure flow leads to a decrease of average droplet size on the inner cylinder and an increase of average droplet size on the outer cylinder.

The three droplet semiaxes of the disperse phase micro-structure are shown in Fig. 5.14. Here we see that the superimposed pressure flow leads to stronger droplet deformation on the inner cylinder and to a smaller droplet deformation near the outer cylinder. Again droplets in the annular gap deform into prolates. We are in the high viscosity ratio regime.

6. Conclusions

In Chap. 1 we give a literature survey and we motivate the need to develop thermodynamically consistent models for highly viscous emulsions. These models should capture the viscoelastic flow behavior together with microstructural characteristics of the matrix and the droplet inclusions. Furthermore, we introduce and we discuss a Toy Model to give an illustrative example for the type of thermodynamic descriptions pursued in this treatise. The Toy Model is for an emulsion of equi-viscosity Newtonian liquids with low volume fraction of disperse phase. Since the model describes only prolate droplet configurations and it cannot be generalized to account for matrix viscoelasticity, break-up and coalescence phenomena, or the appearance of oblate droplets, a systematic modeling framework is necessary.

In Chap. 2 we introduce a Hamiltonian framework of non-equilibrium Thermodynamics to develop continuum equations for complex fluids. We consider fluids with an unconstrained microstructure (*e. g.* macromolecular fluids) which are described in terms of the classical hydrodynamic fields and a second rank tensorial variable. We explain how to obtain a general set of time evolution equations which hold for a compressible and non-isothermal medium. Then, we repeat the analysis for a fluid with a volume preserving microstructure (*e. g.* a fluid of Newtonian droplets in an Eulerian medium), which is described in terms of a second-rank tensorial variable with fixed determinant. To satisfy the volume preservation constraint a projection is introduced to map the dynamics of the unconstrained microstructure to a volume preserving one.

In Chap. 3 we develop various models for highly viscous emulsions. To accomplish this we combine the flow descriptions developed in Chap. 2 to describe the matrix phase and the droplet shape with the two different microstructural variables. For simplicity, we restrict to incompressible and isothermal media. Making constitutive assumptions for phenomenological coefficients of matrix phase relaxation, droplet interface relaxation, and matrix-droplet interaction we derive a model for highly viscous emulsions in Sec. 3.1. In Sec. 3.2 the model is generalized to describe droplet break-up and coalescence. Furthermore, we explain how emulsions with surface active molecules at the interface should be modeled and we discuss emulsions with a high volume fraction of disperse phase. In the appropriate limits the models of Chap. 3 reduce to the Toy Model of Chap. 1.

In Chaps. 4 and 5 we solve different flow problems to understand basic model features and to demonstrate that the models are suitable for CFD calculations for emulsions. Since the models of Chap. 3 are coupled non-linear partial differential equations computer codes have to be developed. We restrict our computational work to the more complex emulsion models of Secs. 3.1 and 3.2. In Chaps. 4 we solve the emulsion model for transient and steady flows as encountered in rheometric characterization. For transient shear flow we find a non-linear start-up behavior of the viscometric and morphological emulsion properties with over- and under-shoots. For steady shear flow the models predict shear thinning, shear thickening, and non-trivial normal stress coefficients. The ratio of normal stress differences is large in the low shear rate regime. Moreover, model characteristics are discussed for elongational flows and for the four-roll-mill flow. The model predictions are in qualitative agreement with experimental data. With these models we are able to study systematically the influence of matrix viscoelasticity on droplet shape, the effect of break-up and coalescence on the rheology, and we recover oblate droplet configurations in the small viscosity ratio regime. We overcome the problems of the Toy Model.

In Chap. 5 the emulsion models are formulated in terms of Two Point Boundary Value Problems in order to solve for simple flows of practical importance. This is done to demonstrate that the models can be used for CFD simulations of emulsions. The models are solved for pressure driven channel and tube flow in the steady state. The velocity, shear rate, stress tensor, and droplet shape profiles are computed. The wall viscometric material properties are determined as a function of the wall shear rate and the relationship with the homogeneous flow calculations of Chap. 4 is worked out. Furthermore, the emulsion models have been solved for steady flow in the annular gap. We solve for Poiseuille, Couette, and helical flow in the gap and we discuss the viscometric and morphological emulsion characteristics together with the flow field. We find that centrifugal forces affect the break-up of droplets and we discuss the consequences for dispersing processes. We conclude that helical flow gives satisfactory emulsion dispersing if weak Poiseuille flow is superimposed on Couette flow.

Bibliography

- Aït-Kadi, A., Ramazani, A., Grmela, M., and Zhou, C. (1999). “Volume preserving” rheological models for polymer melts and solutions using the GENERIC formalism. *J. Rheol.*, 43:51–72.
- Almusallam, A. S., Larson, R. G., and Solomon, M. J. (2000). A constitutive model for the prediction of ellipsoidal droplet shapes and stresses in immiscible blends. *J. Rheol.*, 44:1055–1083.
- Beris, A. N. and Edwards, B. J. (1990a). Poisson bracket formulation of incompressible flow equations in continuum mechanics. *J. Rheol.*, 34:55–78.
- Beris, A. N. and Edwards, B. J. (1990b). Poisson bracket formulation of viscoelastic flow equations of differential type - a unified approach. *J. Rheol.*, 34:503–538.
- Beris, A. N. and Edwards, B. J. (1994). *Thermodynamics of Flowing Systems*. Oxford University Press, New York.
- Bird, R. B., Armstrong, R. C., and Hassager, O. (1987). *Dynamics of polymeric liquids: Fluid Mechanics*, volume 1. John Wiley & Sons, Inc., New York, NY, U.S.A. Nebis Signatur: 434 119: 1.
- Bronshtein, I. N. and Semendyayev, K. A. (1985). *A Guidebook to Mathematics*. Verlag Harri Deutsch, Zürich.
- Caserta, S., Sabetta, L., Simeone, M., and Guido, S. (2005). Shear-induced coalescence in aqueous biopolymer mixtures. *Chem. Eng. Sci.*, 60:1019–1027.
- Caserta, S., Simeone, M., and Guido, S. (2004). Evolution of drop size distribution of polymer blends under shear flow by optical sectioning. *Rheol. Acta*, 43:491–501.

- Chin, H. B. and Han, C. D. (1979). Studies on droplet deformation and breakup: I. Droplet deformation in extensional flow. *J. Rheol.*, 23(5):557–590.
- Choi, S. J. and Schowalter, W. R. (1975). Rheological properties of nondilute suspensions of deformable particles. *Phys. Fluids*, 18(4):420–427.
- Delaby, I., Ernst, B., Germain, Y., and Muller, R. (1994). Droplet deformation in polymer blends during uniaxial elongational flow: Influence of viscosity ratio for large capillary numbers. *J. Rheol.*, 38(6):1705–1720.
- Doi, M. and Ohta, T. (1991). Dynamics and rheology of complex interfaces. *J. Chem. Phys.*, 95:1242–1248.
- Dressler, M. and Edwards, B. J. (2004). The influence of matrix viscoelasticity on the rheology of polymer blends. *Rheol. Acta.*, 43:257–282.
- Dressler, M. and Edwards, B. J. (2005). A method for calculating rheological and morphological properties of constant-volume polymer blend models in inhomogeneous shear fields. *J. Non-Newtonian Fluid Mech.*, 130:77–95.
- Dressler, M. and Edwards, B. J. (2006). Channel, Tube, and Taylor-Couette flow of complex viscoelastic fluid models. *Rheol. Acta.*, 46:59–82.
- Dressler, M., Edwards, B. J., and Öttinger, H. C. (1999). Macroscopic thermodynamics of flowing polymeric liquids. *Rheol. Acta.*, 38:117–136.
- Edwards, B. J. (1998). An analysis of single and double generator thermodynamic formalisms for the macroscopic description of complex fluids. *J. Non-Equilib. Thermodyn.*, 23:301–333.
- Edwards, B. J. and Beris, A. N. (1991a). Noncanonical Poisson bracket for nonlinear elasticity with extensions to viscoelasticity. *J. Phys. A-Math. Gen.*, 24:2461–2480.
- Edwards, B. J. and Beris, A. N. (1991b). Unified view of transport phenomena based on the generalized bracket formulation. *Ind. Eng. Chem. Res.*, 30:873–881.
- Edwards, B. J. and Beris, A. N. (1992). The dynamics of a thermotropic liquid-crystal. *Eur. J. Mech. B-Fluids*, 11:121–142.
- Edwards, B. J., Beris, A. N., and Grmela, M. (1991). The dynamic behavior of liquid-crystals - a continuum description through generalized brackets. *Mol. Cryst. Liquid Cryst.*, 201:51–86.

- Edwards, B. J., Beris, A. N., and Mavrantzas, V. G. (1996). A model with two coupled Maxwell modes. *J. Rheol.*, 40:917–942.
- Edwards, B. J., Beris, A. N., and Öttinger, H. C. (1998). An analysis of single and double generator thermodynamic formalisms for complex fluids. II. The microscopic description. *J. Non-Equilib. Thermodyn.*, 23:334–350.
- Edwards, B. J. and Dressler, M. (2003). A rheological model with constant approximate volume for immiscible blends of ellipsoidal droplets. *Rheol. Acta*, 42:326–337.
- Edwards, B. J., Dressler, M., Grmela, M., and Ait-Kadi, A. (2003). Rheological models with microstructural constraints. *Rheol. Acta*, 42:64–72.
- Feigl, K., Kaufmann, S. F. M., Fischer, P., and Windhab, E. J. (2003). A numerical procedure for calculating droplet deformation in dispersing flows and experimental verification. *Chem. Eng. Sci.*, 58:2351–2363.
- Fortelný, I. (2001). Analysis of the effect of breakup frequency on the steady droplet size in flowing polymer blends. *Rheol. Acta*, 40:485–489.
- Fortelný, I. and Zivný, A. (2003). Extensional flow induced coalescence in polymer blends. *Rheol. Acta*, 42:454–461.
- Greco, F. (2002). Drop deformation for non-Newtonian fluids in slow flows. *J. Non-Newtonian Fluid Mech.*, 107:111–131.
- Grizzuti, N. and Bifulco, O. (1997). Effects of coalescence and breakup on the steady state morphology of an immiscible polymer blend in shear flow. *Rheol. Acta*, 36:406–415.
- Grmela, M., Bousmina, M., and Palierne, J. F. (2001). On the rheology of immiscible blends. *Rheol. Acta*, 40:560–569.
- Grmela, M. and Öttinger, H. C. (1997). Dynamics and thermodynamics of complex fluids. I. Development of a general formalism. *Phys. Rev. E*, 56:6620–6632.
- Guido, S., Simeone, M., and Greco, F. (2003a). Deformation of a Newtonian drop in a viscoelastic matrix under steady shear flow: Experimental validation of slow flow theory. *J. Non-Newtonian Fluid Mech.*, 114:65–82.
- Guido, S., Simeone, M., and Greco, F. (2003b). Effects of matrix viscoelasticity on drop deformation in dilute polymer blends under slow shear flow. *Polymer*, 44:467–471.

- Guido, S. and Villone, M. (1998). Three-dimensional shape of a drop under simple shear flow. *J. Rheol.*, 42:395–415.
- Hu, Y. T. and Lips, A. (2003). Transient and steady state three-dimensional drop shapes and dimensions under planar extensional flow. *J. Rheol.*, 47:349–369.
- Iza, M., Bousmina, M., and Jerome, R. (2001). Rheology of compatibilized immiscible viscoelastic polymer blends. *Rheol. Acta*, 40:10–22.
- Jansseune, T., Mewis, J., Moldenaers, P., Minale, M., and Maffettone, P. L. (2000). Rheology and rheological morphology determination in immiscible two-phase polymer model blends. *J. Non-Newtonian Fluid Mech.*, 93:153–165.
- Jansseune, T., Vinckier, I., Moldenaers, P., and Mewis, J. (2001). Transient stresses in immiscible model polymer blends during start-up flows. *J. Non-Newtonian Fluid Mech.*, 99:167–181.
- Kaufmann, S. F. M. (2002). *Experimentelle und numerische Untersuchungen von Tropfendispergiervorgängen in komplexen laminaren Strömungsfeldern*. Dissertation, Eidgenössische Technische Hochschule Zürich, CH.
- Kernick, W. A. and Wagner, N. J. (1999). The role of liquid-crystalline polymer rheology on the evolving morphology of immiscible blends containing liquid-crystalline polymers. *J. Rheol.*, 43:521–549.
- Lacroix, C., Grmela, M., and Carreau, P. J. (1999). Morphological evolution of immiscible polymer blends in simple shear and elongational flows. *J. Non-Newtonian Fluid Mech.*, 86:37–59.
- Levitt, L., Macosko, C. W., and Pearson, S. D. (1996). Influence of normal stress difference on polymer drop deformation. *Polym. Eng. Sci.*, 36:1647–1665.
- Loewenberg, M. and Hinch, E. J. (1996). Numerical simulation of a concentrated emulsion in shear flow. *J. Fluid Mech.*, 321:395–419.
- Maffettone, P. L. and Greco, F. (2004). An ellipsoidal drop model for single drop dynamics with non-Newtonian fluids. *J. Rheol.*, 48:83–100.
- Maffettone, P. L. and Minale, M. (1998). Equation of change for ellipsoidal drops in viscous flow. Erratum (1999) 84:105-106. *J. Non-Newtonian Fluid Mech.*, 78:227–241.
- Megias-Alguacil, D., Fischer, P., Dressler, M., Feigl, K., and Windhab, E. J. (2005).

- Droplet deformation under simple shear investigated by experiment, numerical simulation, and modeling. *J. Non-Newtonian Fluid Mech.*, 126:153–161.
- Megias-Alguacil, D., Fischer, P., and Windhab, E. J. (2004). Experimental determination of interfacial tension by different dynamical methods under simple shear flow conditions with a novel computer-controlled parallel band apparatus. *J. Colloid Interface Sci.*, 274:631–636.
- Minale, M. (2004). Deformation of a non-Newtonian ellipsoidal drop in a non-Newtonian matrix: Extension of Maffettone-Minale model. *J. Non-Newtonian Fluid Mech.*, 123:151–160.
- Minale, M. and Maffettone, P. L. (2003). Morphology estimation from normal stress measurements for dilute immiscible polymer blends. *Rheol. Acta.*, 42:158–165.
- Oldroyd, J. G. (1953). The elastic and viscous properties of emulsions and suspensions. *Proc. R. Soc. London Ser. A-Math.*, 218:122–132.
- Oldroyd, J. G. (1955). The effect of interfacial stabilizing films on the elastic and viscous properties of emulsions. *Proc. R. Soc. London Ser. A-Math.*, 232:567–577.
- Öttinger, H. C. and Grmela, M. (1997). Dynamics and thermodynamics of complex fluids. II. Illustrations of a general formalism. *Phys. Rev. E*, 56:6633–6655.
- Palierne, J. F. (1990). Linear rheology of viscoelastic emulsions with interfacial tension. *Rheol. Acta*, 29(3):204–214.
- Press, W. H., Teukolsky, S. A., Vetterling, W. T., and Flannery, B. P. (1992). *Numerical Recipes*. Cambridge University Press, second edition.
- Souvaliotis, A. and Beris, A. N. (1992). An extended White-Metzner viscoelastic fluid model based on an internal structural parameter. *J. Rheol.*, 36:241–271.
- Tanner, R. I. (2000). *Engineering Rheology*. Oxford University Press, New York, second edition.
- Taylor, G. I. (1932). The viscosity of a fluid containing small drops of another fluid. *Proc. Roy. Soc. London Ser. A*, 138:41–48.
- Taylor, G. I. (1934). The formation of emulsions in definable fields of flow. *Proc. Roy. Soc. London Ser. A*, 146:501–523.

- Vinckier, I., Mewis, J., and Moldenaers, P. (1997). Stress relaxation as a microstructural probe for immiscible polymer blends. *Rheol. Acta*, 36:513–523.
- Vinckier, I., Moldenaers, P., and Mewis, J. (1996). Relationship between rheology and morphology of model blends in steady shear flow. *J. Rheol.*, 40:613–631.
- Wagner, N. J., Öttinger, H. C., and Edwards, B. J. (1999). Generalized Doi-Ohta model for multiphase flow developed via GENERIC. *AICHE J.*, 45:1169–1181.
- Windhab, E. J., Dressler, M., Feigl, K., Megias-Alguacil, D., and Fischer, P. (2005). Emulsion processing - from single drop deformation to design of complex processes and products. *Chem. Eng. Sci.*, 60:2101–2113.
- Wolf, B. (1995). *Untersuchungen zum Formverhalten mikroskopisch kleiner Fluidtropfen in stationären und instationären Scherströmungen*. Dissertation, Eidgenössische Technische Hochschule Zürich, CH.
- Yu, W., Bousmina, M., Grmela, M., Palierne, J. F., and Zhou, C. X. (2002). Quantitative relationship between rheology and morphology in emulsions. *J. Rheol.*, 46:1381–1399.
- Yu, W., Zhou, C. X., and Bousmina, M. (2005). Theory of morphology evolution in mixtures of viscoelastic immiscible components. *J. Rheol.*, 49:215–236.

Appendix

A. Comparison with Experimental Trends

The appendix deals with preliminary fitting of the emulsion models with experimental data for polymer blends. We fit morphological characteristics related to droplet deformation as well as non-linear flow curves related to blend viscoelasticity. Experimental data are taken from the literature. Fits with experiments performed at ETH Laboratory of Food Process Engineering and comparison with boundary integral calculations (Loewenberg and Hinch, 1996) have been published in Megias-Alguacil et al. (2005).

A.1. Single Droplet Deformation in Viscoelastic Matrix Fluid

Single droplet deformation measurements in a viscoelastic matrix fluid are reported, e. g. in Guido et al. (2003a,b) and, earlier, in Levitt et al. (1996). Whereas Guido et al. (2003a,b) study droplets of a Newtonian liquid Levitt et al. (1996) report measurements on droplets of a viscoelastic fluid. In what follows we fit our blend model to the experimental data of Guido et al. (2003b).

In Guido et al. (2003b) the dynamics of a single silicon drop ($R = 50\mu\text{m}$, $\eta^* = 13\text{Pas}$) in a viscoelastic matrix fluid made of corn syrup with 0.13wt% polyacrylamide ($\eta_c = 10\text{Pas}$, $\Psi_{1,c} = 2.5\text{Pas}^2$) has been investigated. The interfacial tension between the two liquids is $\Gamma' = 30\text{mN/m}$. Invoking the UCMM and the relationship for the interfacial elastic modulus, we obtain $G = 80\text{Pa}$ and $\Gamma = 600\text{Pa}$, respectively. Fig. A.1 shows steady-state morphological predictions of our model (solid lines) together with experimental data (symbols) reported in Guido et al. (2003b). Fig. A.1a shows a monotonic increase and decrease of the major and the minor droplet axes in the shearing plane, respectively. Fig. A.1b displays a strong decrease of the steady-state orientation angle. Solid lines in Fig. A.1 have been calculated for the following values of the ratio of matrix and interfacial elasticity, the viscosity ratio, and the droplet concentration: $G/\Gamma = 0.13$, $p^* = -1.3$,

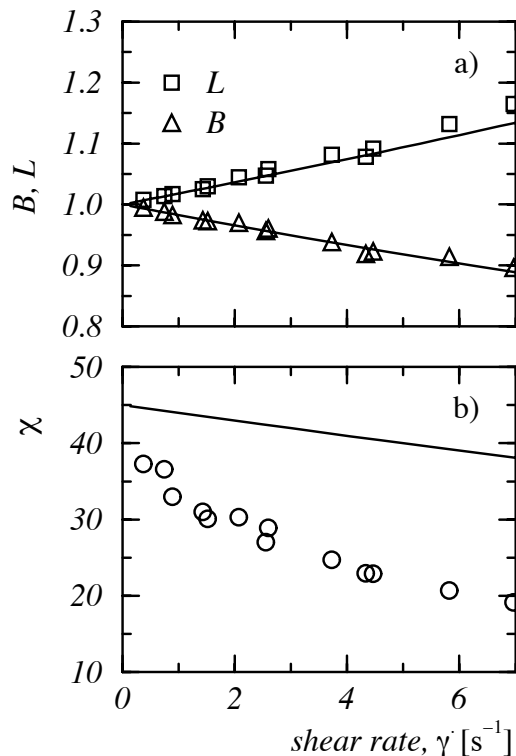


Figure A.1.: The major and the minor semiaxes, L , B (a) and the orientation angle, χ (b) of a single silicon droplet in a viscoelastic corn syrup matrix (symbols) together with model predictions (solid lines). Experimental data are from Guido et al. (2003b).

$\phi = 0.01$. The EWM power law index, k , has been taken as vanishing. Note that for the calculations in Fig. A.1 the phenomenological coefficient p^* has been taken as the viscosity ratio of the blend components, *i.e.*, $p^* = -\eta^*/\eta_c = -1.3$ is an independent quantity. For the purpose of the present comparison with experimental data we chose $\phi = 0.01$ which is reasonable to represent the low concentration regime of a single droplet experiment. To fit experimental data the following values for the relaxation times and the phenomenological coupling parameter have been adopted: $\lambda_c = 10^{-3}s$, $\lambda_s = 5 \cdot 10^{-4}s$, $\theta = 0.01$. (Note that model predictions are insensitive for $0.01 < \theta < 0.05$.) We notice that the fit of the droplet semiaxes is satisfactory in Fig. A.1, whereas the strong decrease of the orientation angle is not predicted by our model. The strong decrease of the orientation angle with increasing shear rate is presumably due to a non-affine motion of the silicon droplet with respect to the externally-imposed flow field and it may be recovered using the Gordon-Schowalter derivative in the droplet shape tensor, Eq. (3.3c). The perturbative approach proposed by Greco (2002) gives a more satisfactory fit to experimental data compared to the present model (*cf.* Guido et al., 2003b, Fig. 4).

A.2. PIB/PDMS blend with low viscoelastic contrast

Vinckier et al. (1996) studied morphological and rheological properties of different blends of polyisobutene (PIB, $\eta_d = 86\text{Pas}$) and polydimethylsiloxane (PDMS, $\eta_c = 195\text{Pas}$, $\Psi_{1,c} = 10.4\text{Pas}^2$) in steady shear flow. Whereas pure PDMS shows a pronounced shear thinning behavior, pure PIB is Newtonian for shear rates $\dot{\gamma} \lesssim 10\text{s}^{-1}$ (Vinckier et al., 1996). Therefore, we compare experiments on PIB/PDMS blends with our model. Interfacial tension between the blend components is $\Gamma' = 2.3\text{mN/m}$. With the UCMM and the relationship for the interfacial elastic modulus we obtain $G \approx 7300\text{Pa}$ and $\Gamma = 230\text{Pa}$ for an average droplet radius of $10\mu\text{m}$. In what follows, we fit rheological measurements of 10wt% and 30wt% PIB in PDMS with our model.

Figure A.2 shows calculations for the pure matrix fluid with $G = 7300\text{Pa}$ and $\phi = 0$ (solid lines) and two PIB/PDMS blends with $G/\Gamma = 30$, $\phi = 0.1$ (dashed lines) and $G/\Gamma = 30$, $\phi = 0.3$ (dotted lines). The EWM power-law index has been taken as $k = -2$ to recover the shear-thinning behavior for the matrix fluid and the phenomenological coupling coefficient has been chosen as $\theta = 0.01$. The phenomenological parameter, p^* , is not taken as the viscosity ratio of the blend components, but it is related to the interfacial elasticity in Figs. A.2 and A.3, $p^* = -\eta^*/\eta_c$. The ratio of relaxation times λ_c/λ_s is adjusted to fit experimental data.

In Fig. A.2a and b, we show the steady-state shear viscosity and the first normal stress coefficient for the viscoelastic PDMS matrix fluid and for two different PIB/PDMS blends (symbols) together with model predictions (lines). Experimental data have been taken from Vinckier et al. (1996) and they have been normalized with their zero shear rate values. Circles in Fig. A.2a,b are for the viscometric properties of the pure PDMS matrix fluid, squares and diamonds represent the $\phi = 0.1$ and the $\phi = 0.3$ PIB/PDMS blend, respectively. Solid lines in Fig. A.2a,b have been calculated from the model equations with $G = 7300\text{Pa}$, $\phi = 0$, and $k = -2$ for the EWM power law index to fit the shear thinning of the matrix phase. The dashed lines and the dotted lines in Fig. A.2 have been calculated for $G/\Gamma = 30$, $k = -2$ and $\phi = 0.1, 0.3$ for the 10wt% and the 30wt% blends, respectively. The relaxation times and the phenomenological coupling parameter have been chosen to recover the shear-thinning behavior. This is reasonable since there is no standard technique available to determine the relaxation time of the interface, λ_s – cf. Vinckier et al. (1996, Figs. 6 and 7). We took $\lambda_c = 0.03\text{s}$, $\theta = 0$ for pure PDMS, $\lambda_c/\lambda_s = 0.012$, $\theta = 0.01$ for the $\phi = 0.1$ blend, and $\lambda_c/\lambda_s = 0.04$, $\theta = 0.01$ for the $\phi = 0.3$ blend. Note that in Fig. A.2 the phenomenological coefficient p^* is related to the elasticity of the matrix phase and the interface, *i. e.*, $p^* = -(\Gamma\lambda_s)/(G\lambda_c)$. We note that

A. Comparison with Experimental Trends

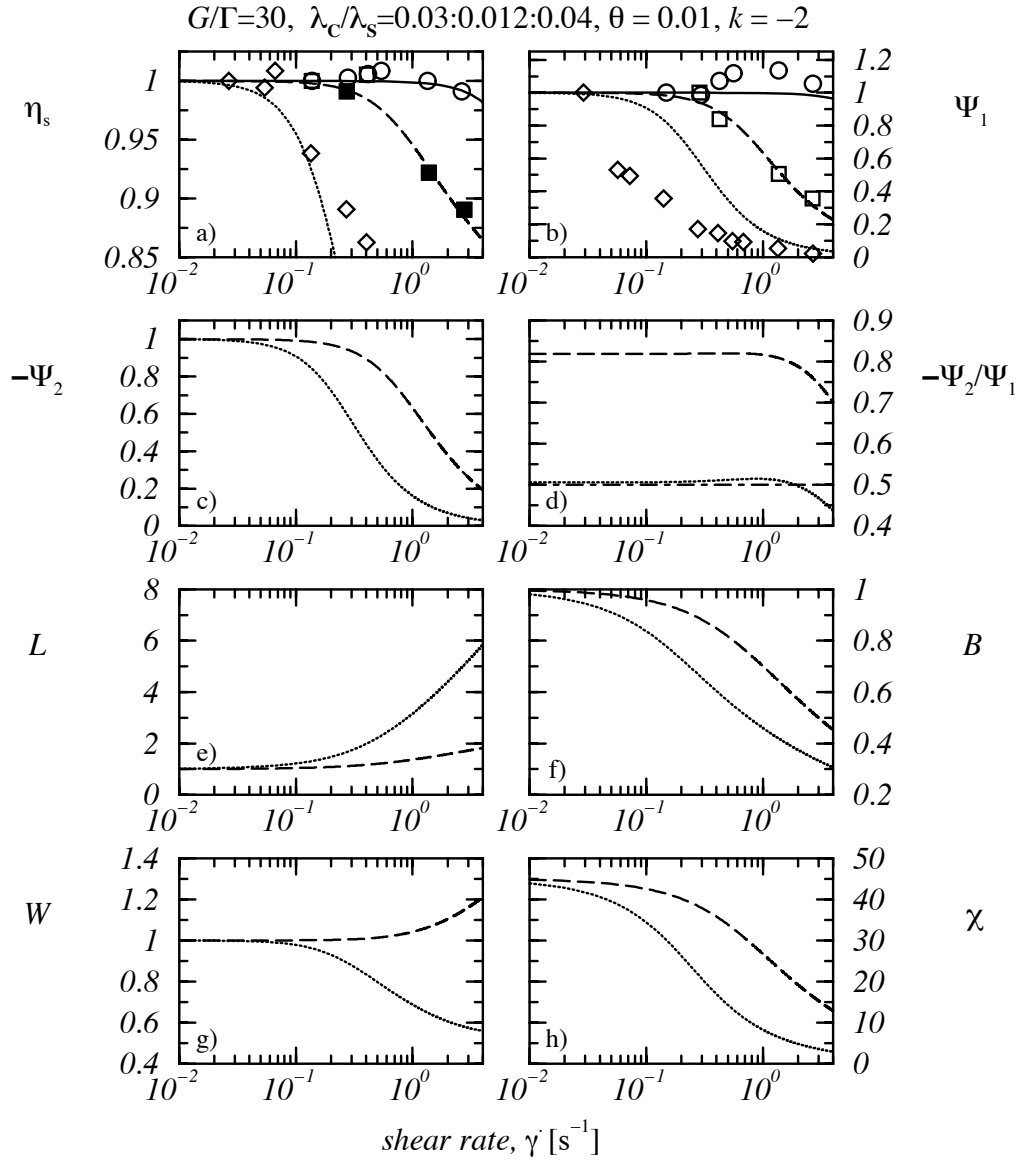


Figure A.2.: Model predictions of the continuum equations for constant droplet distribution $n = 1$, as a function of shear rate for three different dispersed phase concentrations, $\phi = 0$ (solid lines), 0.1 (dashed lines), and 0.3 (dotted lines). Other model parameters are $G = 7300$, $k = -2$ (for $\phi = 0$); $G/\Gamma = 30$, $\theta = 0.01$, $k = -2$ (for $\phi \neq 0$); $p^* = -\Gamma\lambda_s/G\lambda_c$. The ratio of relaxation times has been taken as a fitting parameter: $\lambda_c/\lambda_s = 0.03$ ($\phi = 0$), 0.012 ($\phi = 0.1$), 0.04 ($\phi = 0.3$). The viscometric functions have been normalized with respect to their zero shear-rate values. Symbols are experimental data from Vinckier et al. (1996).

model predictions for the steady-shear viscosity and the first normal stress coefficient are satisfactory for $\phi = 0.1$. For $\phi = 0.3$ only the onset of the shear-thinning behavior is recovered from the model and the model fails to predict the quantitative behavior of the first normal stress coefficient. The fit to both rheological characteristic functions is satisfactory only in the dilute regime, $\phi \lesssim 0.2$.

Figs. A.2c-h show further solutions of the system equations for which no experimental data are available. Note that for the pure matrix fluid, the EWM model predicts $\Psi_2 = 0$ and no droplet morphology is present. Therefore, only the predictions of the two blends are reported in the remaining graphs of Fig. A.2. Fig. A.2c displays the shear-thinning behavior of the second normal stress coefficient, Ψ_2 , for the $\phi = 0.1$ and the 0.3 blend. Fig. A.2d shows the ratio of the two normal stress coefficients. For $\phi = 0.1$, we recover $\Psi_2/\Psi_1 \approx -0.8$ being considerably larger than for polymer melts, whereas for $\phi = 0.3$ a smaller value of $\Psi_2/\Psi_1 \approx -0.5$ is recovered from the system equations. This value is close to the stress tensor predictions of the Maffettone-Minale (MM) Model, $\Psi_2/\Psi_1 = -0.5$, cf. Yu et al. (2002), which has also been included in Fig. A.2d.

In Figs. A.2e-h we display the morphological characteristics of the polymer blend, which are represented by the average magnitude of the three semiaxes of the ellipsoidal droplets and the average orientation of the droplets with respect to the flow direction. The semiaxes of the droplets are the square roots of the eigenvalues of the droplet configuration tensor, \mathbf{S} Maffettone and Minale (1998). The droplet semiaxes in the flow direction, in the direction of the shear gradient, and in the direction of the vorticity axis are denoted with L , B , W , respectively. For steady shear flow, the major droplet axis, L , increases and the minor droplet axis, B , decreases with respect to the equilibrium droplet radius (Figs. A.2e, f). However, the vorticity axis, W , can be greater than, smaller than, or equal to unity upon start-up of flow and the droplets are thus either oblate or prolate. In Fig. A.2g, we have oblate droplets ($W > 1$) for the $\phi = 0.1$ blend and prolate droplets ($W < 1$) for the $\phi = 0.3$ blend. The orientation angle, χ , is the angle between the eigenvector corresponding to the largest eigenvalue of the \mathbf{S} -tensor and the flow direction; it is defined as $\chi = 1/2 \arctan[2S_{12}/(S_{11} - S_{22})]$. This quantity decreases for increasing shear rate, Fig. A.2h.

In Guido et al. (2003a) the steady-state deformation of single Newtonian droplets in a viscoelastic matrix is studied where the continuous and the dispersed phase are a non-Newtonian polyisobutylene (PIB) and a Newtonian Polydimethylsiloxane (PDMS), respectively. For viscosity ratios $p^* = -1$ and $p^* = -0.1$, steady-state prolate droplets have been observed. Note, that this is identical to the blend system investigated rheologically by Vinckier et al. (1996) except that Guido et al. (2003a) perform measurements on a single droplet whereas Vinckier et al. (1996) study the rheological response of the blend, hence there is no full control of the droplet morphology.

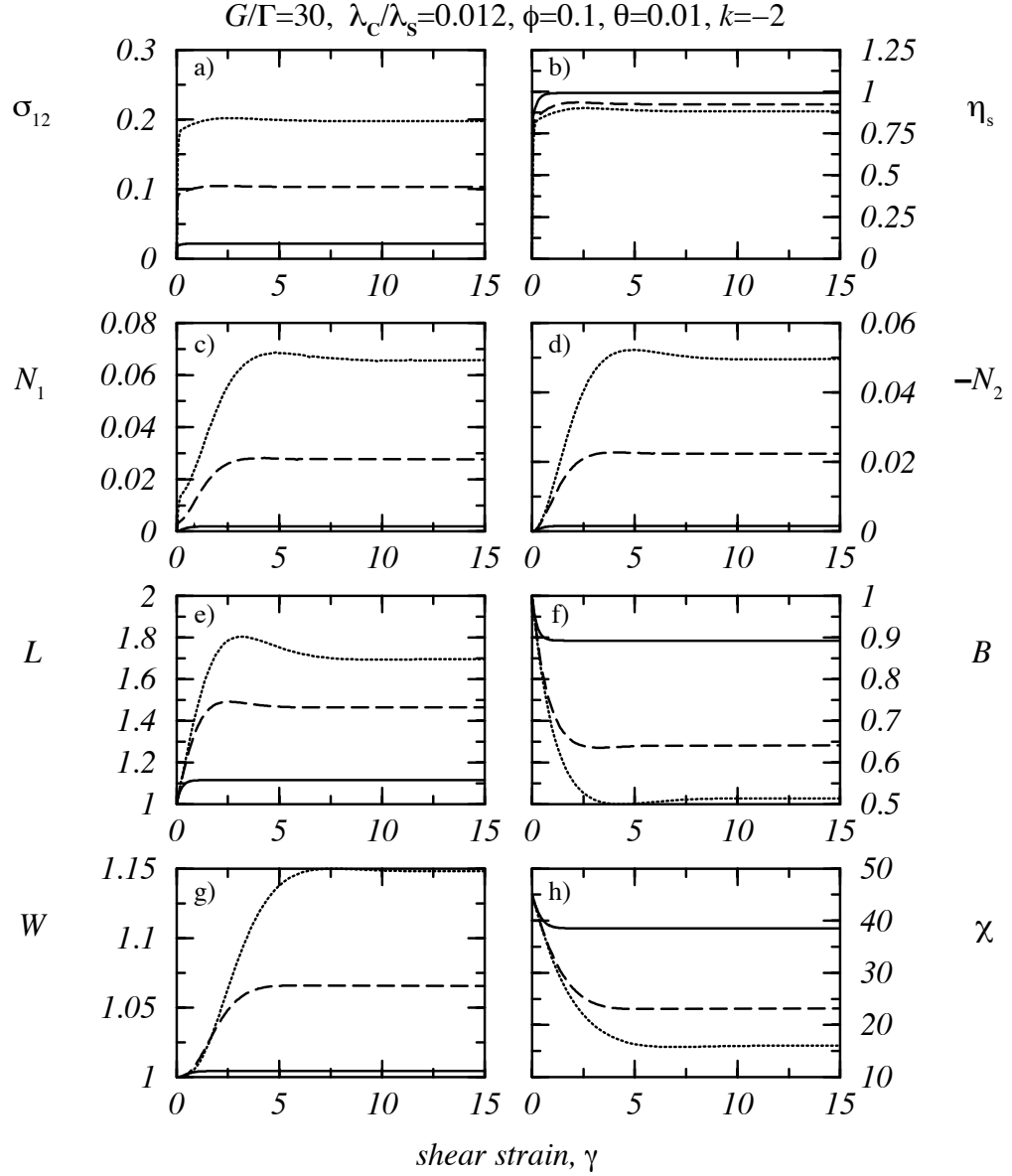


Figure A.3.: The same as Fig. A.2 for start-up of steady shearing flow as a function of shear strain for the $\phi = 0.1$ blend and three different shear rates, $\dot{\gamma} = 0.27\text{s}^{-1}$ (solid lines), 1.38s^{-1} (dashed lines), and 2.77s^{-1} (dotted lines) corresponding to the filled symbols in Fig. A.2. The shear viscosities in b) are normalized with respect to the zero shear-rate viscosity.

Figure A.3 displays transient solutions of the continuum equations for start-up of steady shearing flow for the $\phi = 0.1$ blend. Sample calculations were carried out for three different shear rates, $\dot{\gamma} = 0.27\text{s}^{-1}$ (solid lines), 1.38s^{-1} (dashed lines), and 2.77s^{-1} (dotted lines), which correspond to the abscissas of the filled squares in Fig. A.2a. Material parameters are the same as in Fig. A.2 for the 10wt% PIB/PDMS blend, *i.e.*, $G/\Gamma = 30$, $\theta = 0.01$, $k = -2$, and $\lambda_C/\lambda_S = 0.012$. Figs. A.3a-d display the transient viscometric behavior of the system equations showing a typical non-linear viscoelastic response as encountered often in synthetic polymer rheology. The transient shear stress, σ_{12} , and the shear viscosity, $\eta_s = \sigma_{12}/\dot{\gamma}$, (Figs. A.3a, b) show a rapid approach to their steady-state values, which are attained at $\gamma \approx 5$ shear strain units. The shear viscosity in Fig. A.3b has been normalized with respect to the zero shear-rate value. The first normal stress difference in Fig. A.3c is positive and shows a monotonic increase for the lowest shear rate ($\dot{\gamma} = 0.27\text{s}^{-1}$, solid line), whereas a slight overshoot is seen for the higher shear rates ($\dot{\gamma} = 1.38\text{s}^{-1}$, 2.77s^{-1} , broken lines). The steady-state value of N_1 is attained at strains of $\gamma \approx 10$, being twice as high as the strains that are necessary to attain a steady-state shear stress. The first normal stress difference is approximately one order of magnitude smaller than the shear stress. The second normal stress difference in Fig. A.3d is negative, and of the same order of magnitude as the first normal stress difference. Both normal stress differences, N_1 and N_2 , show a similar qualitative behavior as a function of strain rate in the regime of shear rates shown in Fig. A.3.

Figs. A.3e-h display the transient morphological properties of the $\phi = 0.1$ blend for start-up of steady shearing flow. For the low shear rate, $\dot{\gamma} = 0.27\text{s}^{-1}$ (solid line), we recover a monotonic approach of the droplet axes and the orientation angle towards their steady-state values. For the highest shear rate, $\dot{\gamma} = 2.77\text{s}^{-1}$ (dotted line), a pronounced overshoot is observed in L , which goes along with slight undershoots in the two minor droplet axes, B and W . For all shear rates shown in Fig. A.3, the droplet shape evolves towards a oblate, sheet-like configuration.

Levitt et al. (1996) report transient morphological measurements of a single polypropylene droplet in a viscoelastic matrix with $G/G_d \approx 0.3$, where G_d is the elastic modulus of the dispersed phase. Immediately after start-up of steady shear flow, an increase of the vorticity axis to 40% of its equilibrium value is observed. For higher shear strains, the vorticity axis decreases and a prolate droplet is recovered.

In the above sample calculations, we see that the transient first normal stress difference is approximately one order of magnitude smaller than the shear stress ($\sigma_{12} \gg N_1$) for the shear-rate regime investigated in Fig. A.3. The changes that the externally imposed flow field induces in the droplet morphology are as large as 70% for the major droplet axis, L . For the minor droplet axis, B , and for the vorticity axis, W , we recover variations of 50% and 15%, respectively, for a shear rate as high as $\dot{\gamma} = 2.77\text{s}^{-1}$, and a steady state is recovered from the model. This may be due to the viscoelastic similarity between the

matrix and the interface, which is quantified in terms of $G/\Gamma = 30$ and $\lambda_C/\lambda_S = 0.012$. With these values, we calculate $\Psi_{1c}/\Psi_{1d} \approx 4 \cdot 10^{-3}$ for the ratio of zero shear-rate first normal stress coefficients.

A.3. HPC/PDMS600 blend with high viscoelastic contrast

Now, we wish to solve the continuum equations for a polymer blend with a high viscoelastic contrast between the matrix phase and the interface and to investigate whether a large viscoelastic contrast of the blend components allows for highly deformed microstructural constituents such as fibers or sheets. This is of technological importance since in processing one is interested in the creation of a strongly deformed droplet morphology with a high amount of interface.

In Fig. A.4 we present sample calculations for a polymer blend with a strong viscoelastic contrast between the two phases. Also for the present calculations, we assume a constant DDF, *i.e.*, $n = 1$. However, we take the phenomenological coefficient, p^* , as an independent quantity, *i. e.*, $p^* = -\eta_d/\eta_c$ corresponds to the viscosity ratio of the blend components. Polymer blends with a strong viscoelastic contrast are of technological importance because it is possible to produce highly deformed inclusions (*e.g.*, fibers or sheets), by means of modest mechanical deformation of the blend. Kernick and Wagner (1999), *e.g.*, examined a polymer blend of 5wt% hydroxypropyl cellulose (HPC, $\eta_d \approx 300\text{Pas}$) in a PDMS ($\eta_d = 600\text{Pas}$) matrix by means of rheology and small angle neutron scattering. In this system, the large viscoelastic contrast between the matrix and the dispersed liquid-crystalline polymer phase is due to the phenomenon that HPC displays a phase transition from the tumbling to the flow aligning regime that correlates with a sign change of the first normal stress difference causing a $\Psi_{1c}/\Psi_{1d} \gg 1$.

Figure A.4 shows calculations for a polymer blend with dispersed phase concentration $\phi = 0.05$, and viscosity ratio $p^* = -0.5$. In the present model, the droplet phase is assumed to be Newtonian and hence anelastic. Only the first normal stress difference of the matrix and the interface can be varied in the model to tune the viscoelastic difference between the two phases. In order to mimic the strong viscoelastic contrast between the two phases, we have taken $G/\Gamma = 10^6$, and $\lambda_C/\lambda_S = 10^3$; *i.e.*, the ratio of the zero shear-rate first normal stress coefficient of the matrix and the interface in the steady state is $\Psi_{1c}/\Psi_{1d} = 10^{12}$. The EWM power-law index for the continuous phase has been chosen as $k = -0.13$, reproducing the shear-thinning behavior of the PDMS matrix (*cf.* Fig. 7 in Kernick and Wagner (1999)).

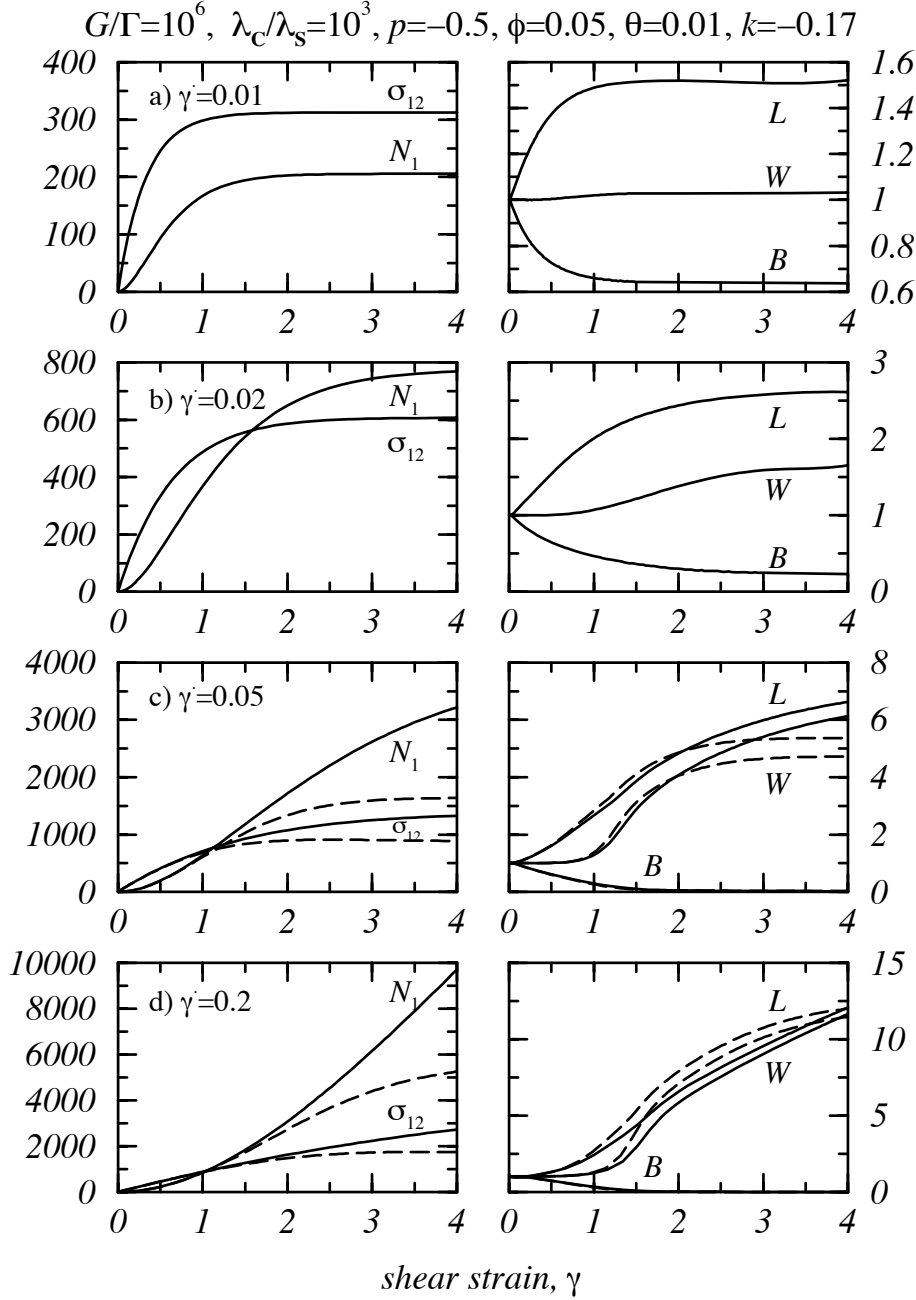


Figure A.4.: The transient shear stress, σ_{12} , and first normal stress difference, N_1 (left column) and the transient droplet axes, L , B , W (right column) for four different shear rates $\dot{\gamma} = 0.01$ (first row), 0.02 (second row), 0.05 (third row), and 0.2 (fourth row). The blend components have a strong viscoelastic contrast with $G/\Gamma = 10^6$ and $\lambda_c/\lambda_s = 10^3$. The phenomenological coefficient $p^* = -0.5$ is taken as the viscosity ratio of the blend components, *i.e.*, an independent model parameter. Other model parameters are $\phi = 0.05$, $\theta = 0.01$, and $k = -0.17$. The dashed lines in c) and d) are for $k = -1.3$.

Figure A.4 shows transient rheological and morphological properties of the model blend for start-up of steady shearing flow for four different shear rates: $\dot{\gamma} = 0.01$ (a), $\dot{\gamma} = 0.02$ (b), $\dot{\gamma} = 0.05$ (c), and $\dot{\gamma} = 0.2$ (d). For the lowest shear rate portrayed in Fig. A.4a, we observe a monotonic increase of the shear stress, σ_{12} , and the first normal stress difference, N_1 , to their respective steady-state values. Note that in the low shear-rate regime, the shear stress is always bigger than the first normal stress difference, which corresponds to a system with a small viscoelastic contrast as studied, e.g., in Figs. A.2, A.3. In this shear-rate regime, only relatively small droplet deformations are observed. In particular, the vorticity axis of the droplet increases slightly and reaches a steady-state value that is approximately 4% above its equilibrium value in the undeformed state. In Fig. A.4b ($\dot{\gamma} = 0.02$), the shear stress is bigger than the first normal stress difference only in the small shear-strain regime, $\gamma^* \approx 1.5$ (γ^* denotes the shear strain where $\sigma_{12} = N_1$ which we can identify from Figs. A.4b-d). For $\gamma > \gamma^*$, the first normal stress difference becomes greater than the shear stress which may be due to the high values of G/Γ and λ_C/λ_S . The crossover of the two stresses correlates with a strong increase of the vorticity axis of the droplet, W , for shear strains $\gamma \approx \gamma^*$. At the steady state, the vorticity axis, W , is approximately 18% above its equilibrium value, whereas for $\dot{\gamma} = 0.01$ an increase of approximately 4% is observed at the steady state (Fig. A.4a). For even higher shear rates, $\dot{\gamma} = 0.05$ and 0.2 , the crossover of the first normal stress difference, N_1 , and the shear stress, σ_{12} , shifts towards smaller shear strains ($\gamma^* \approx 1$), and the first normal stress difference becomes considerably larger than the shear stress (Figs. A.4c, d). For these shear rates, two different droplet deformation regimes can be identified. For $\gamma \lesssim \gamma^*$, we observe only a slight droplet widening in the vorticity direction, whereas the droplet widening becomes very strong for $\gamma \gtrsim \gamma^*$. In the latter strain-rate regime, the strong droplet widening correlates with the droplet extension in the flow direction and the droplets deform into thin disks with $L \approx W \approx 10$ and $B \approx 0$. For smaller EWM power-law indices, the steady state is recovered at smaller shear strains. This is illustrated in Figs. A.4c, d, where predictions for $k = -1.3$ (dashed lines) are included.